X-Ray Tensor Tomography

From Two-Dimensional Directional X-Ray Dark-Field Imaging to Three Dimensions

PhD Thesis
Andreas Dominik Malecki

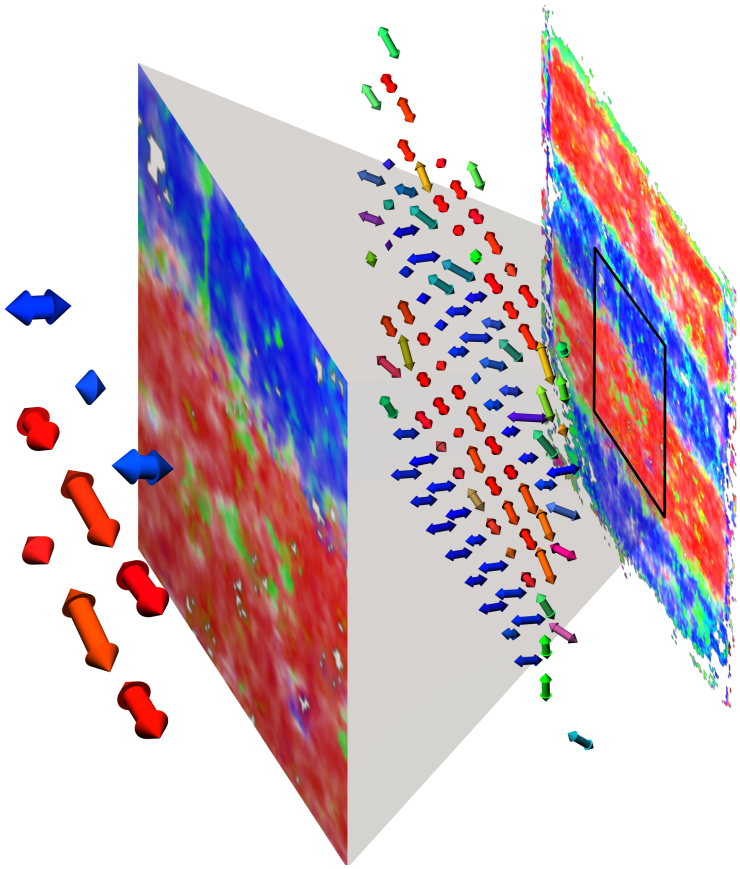

Technische Universität München
Fakultät für Physik
Univ.-Prof. Dr. Franz Pfeiffer
August 2013

Fakultät für Physik

Lehrstuhl für Biomedizinische Physik

X-Ray Tensor Tomography

Andreas Dominik Malecki

Vollständiger Abdruck der von der Fakultät für Physik der Technischen Universität München zur Erlangung des akademischen Grades eines

Doktors der Naturwissenschaften

genehmigten Dissertation.

Vorsitzender:	Univ.-Prof. Dr. J. Leo van Hemmen
Prüfer der Dissertation:	1. Univ.-Prof. Dr. Franz Pfeiffer 2. Univ.-Prof. Dr. Nassir Navab

Die Dissertation wurde am 12. Juni 2013 bei der Technischen Universität München eingereicht und durch die Fakultät für Physik am 8. August 2013 angenommen.

Abstract

Grating-based x-ray phase-contrast imaging provides three different contrast modalities, which are also known from visible light microscopy: transmission contrast, differential phase contrast, and dark-field contrast. Dark-field contrast has its origin in small-angle scattering and arises mainly at sample structure sizes below the detector pixel pitch. Thus, it is a promising candidate for visualization of a sample's microstructure without the requirement of resolving it directly. On the one hand, it has been shown that dark-field contrast allows to perform computed tomography under the assumption of isotropic scattering. Here, the reconstructed quantity represents the local x-ray scattering power. On the other hand, it was proven that the dark-field signal obtained from grating interferometry is strongly dependent on the sample orientation. This is exploited in Directional Dark-Field Imaging. As a consequence, a simple tomographic approach like in absorption-based tomography is not accurate, as it neglects this direction dependence.

In this thesis, I present a novel tomographic reconstruction technique called X-Ray Tensor Tomography, which takes this direction dependence into account and allows to reconstruct the scattering power and its direction at the same time. Several steps had to be taken in advance, to reach this goal: To improve the understanding of the signal formation in x-ray dark-field imaging, I developed a numerical framework, which allows to simulate grating interferometry experiments efficiently (see chapter 2). With this simulation framework, the influence of a sample's microstructure was examined and validated by experiments for simple dark-field imaging (see chapter 2) as well as Directional Dark-Field Imaging (see chapter 3). The new tensor tomography method is based on these results. Its theoretical, experimental, and algorithmic details are treated in chapter 4. Several scientific publications emerged from this PhD project. They are listed together with conference talks and poster presentations starting on page 107.

The novel X-Ray Tensor Tomography technique can be applied to answer ques-

tions in materials science as well as in the medical field. Especially in the clinical environment, the dose applicable to a patient limits the the resolution of the recorded images. Consequently, the resolution of tomographic reconstructions is restricted to several 100 µm as well. However, with the aid of X-Ray Tensor Tomography, it is still possible to extract information about structures that are smaller than the corresponding resolution would allow. The reconstruction results display the local average orientation and anisotropy. This additional information could improve diagnostic results for bone pathologies like osteoporosis without the requirement of a higher detector resolution, which would mean a higher dose to the patient. Further applications and improvements or extensions to the method are the topic of chapter 5.

Zusammenfassung

Gitter-basierte Phasenkontrastbildgebung mit Röntgenstrahlen bietet drei unterschiedliche Kontrastmodalitäten, die bereits von Mikroskopieanwendungen aus dem sichtbaren Bereich des elektromagnetischen Spektrums bekannt sind: Transmissionskontrast, differentiellen Phasenkontrast und Dunkelfeldkontrast. Der Dunkelfeldkontrast hat seinen Ursprung in der Kleinwinkelstreuung und tritt daher an Probenstrukturen auf, die kleiner sind als die Detektorpixelgröße. Daher ist diese Kontrastart ein vielversprechender Kandidat für die Visualisierung der Probenmikrostruktur, ohne dass es erforderlich wäre, diese direkt aufzulösen. Einerseits wurde bereits gezeigt, dass es der Dunkelfeldkontrast unter der Annahme isotroper Streuung erlaubt, Computertomographie zu betreiben. Die rekonstruierte Größe repräsentiert in diesem Fall die lokale Streustärke. Andererseits legen weitere Ergebnisse aus der gitterbasierten Dunkelfeldbildgebung nahe, dass das Dunkelfeldsignal stark von der Probenorientierung abhängt. Dies wird z.B. bei richtungsabhängiger Dunkelfeldbildgebung (im Englischen: Directional Dark-Field Imaging) ausgenutzt. Einfache Tomographieverfahren wie bei herkömmlicher Absorptionsbildgebung sind dafür ungeeignet, da sie diese Richtungsabhängigkeit vernachlässigen.

In dieser Doktorarbeit präsentiere ich eine neue tomographische Rekonstruktionsmethode, die Röntgen-Tensor-Tomographie, die diese Richtungsabhängigkeit berücksichtigt und es ermöglicht, die Streustärke und ihre Richtung gleichzeitig zu rekonstruieren. Um dorthin zu gelangen, waren einige Vorarbeiten nötig: Mit Hilfe eines numerischen Simulations-Frameworks, das ich im Rahmen dieser Arbeit entwickelt habe, können Gitterinterferometrie-Experimente effizient simuliert werden (siehe Kapitel 2). Als wichtige Voraussetzungen für das Verständnis der physikalischen Prozesse, die zum Dunkelfeldsignal führen, habe ich den Einfluss der Mikrostruktur der Probe auf einfache Dunkelfeldbildgebung (siehe Kapitel 2) und richtungsabhängige Dunkelfeldbildgebung (siehe Kapitel 3) untersucht und experimentell bestätigt. Die neue Röntgen-Tensor-Tomographie-Methode basiert auf diesen Ergebnissen. Ihre theoretischen, experimentellen und algorithmischen Details werden in Kapitel 4 behandelt. Im Rah-

men dieses Doktorarbeitsprojekts sind mehrere wissenschaftliche Publikationen entstanden. Diese sind zusammen mit Konferenzvorträgen und Posterpräsentationen ab Seite 107 aufgeführt.

Röntgen-Tensor-Tomographie könnte zukünftig z.B. in den Materialwissenschaften zum Einsatz kommen oder im medizinischen Bereich. Gerade im klinischen Umfeld limitiert die Strahlungsdosis, der ein Patient ausgesetzt werden darf, die Auflösung der Röntgenaufnahmen. Damit ist auch die Auflösung der tomographischen Rekonstruktion beschränkt auf mehrere 100 µm. Mit Hilfe der Röntgen-Tensor-Tomographie ist es jedoch möglich, trotzdem Informationen zu Strukturen aus den gewonnenen Aufnahmen zu extrahieren, die deutlich kleiner sind als es der verfügbaren Auflösung entsprechen würde. Das Rekonstruktionsergebnis zeigt die lokale durchschnittliche Orientierung und Anisotropie an. Mit dieser Zusatzinformation könnten beispielsweise die Diagnoseergebnisse von Knochenkrankheiten wie Osteoporose verbessert werden, ohne eine höhere Detektorauflösung zu benötigen, welche auch eine höhere Dosis für den Patienten bedeuten würde. Weitere Anwendungsmöglichkeiten und zukünftige methodische Verbesserungen oder Erweiterungen werden in Kapitel 5 thematisiert.

To Christiane, my lover, mate, and wife.

To infinity and beyond!

Contents

1 Introduction

How quick are we to learn, that is, to imitate what others have done or thought before. And how slow to understand, that is, to see the deeper connections. Slowest of all, however, are we in inventing new connections or even in applying old ideas in a new field.

Frits Zernike [1]

In 1953, Frits Zernike was awarded the Nobel Prize in Physics for his invention of phase-contrast microscopy [2, 3]. By placing an annular phase plate at the rear focal plane of a microscope's objective, which shifted the phase of the direct light (background illumination) by 90°, he was able to produce a focused image of phase-shifting but otherwise transparent objects. Former approaches were only able to improve the contrast generated by this type of sample by defocusing the object and thus suffered from a trade-off between smearing out the object's features and improving its visibility. As weakly absorbing specimens are rather common in biology and medicine, one can imagine the large impact his invention generated in these fields.

Before Zernike's invention, only two other contrast modalities had been known in microscopy: bright-field and dark-field contrast. The first one is based on the pure absorption properties of the object under examination. The second one is created by modifying the object's illumination and introducing a specifically designed condenser aperture, which blocks the central part of the incident light. Here, without the object, no light reaches the ocular lens. As soon as an object is placed in the beam, fine structures will appear bright in the produced image, as they scatter the incident light. Figure 1.1 shows the three contrast modalities obtained by visible light microscopy of a paper sample.

For a long time since the discovery of x-rays by Wilhelm Conrad Röntgen in

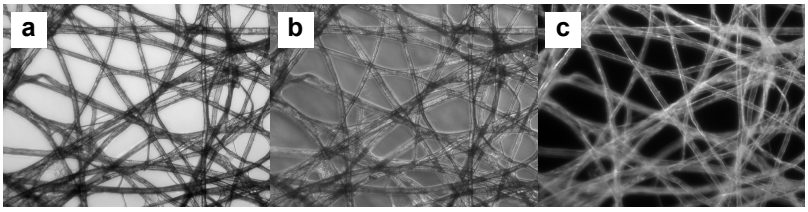

Fig. 1.1: Three contrast modalities of visible light microscopy. Micrographs of Whatman lens tissue paper at tenfold magnification. a) Bright-field contrast shows the absorbing parts of the specimen. b) Phase contrast, however, visualizes its phase-shifting properties, which is especially useful for thin biological samples. c) Dark-field contrast is sensitive to scattering structures only, as the direct light is blocked in this modality. (Images by Richard Wheeler [4–6].)

1895 [7], only one type of contrast modality was known and used with x-rays, namely transmission contrast. It finds its correspondence in the bright-field contrast of visible light microscopy. In 1901, Röntgen was awarded the Nobel Prize in Physics. In his award ceremony speech, C.T. Odhner, President of the Royal Swedish Academy of Sciences, described Röntgen's achievements in the following way [8]:

> *The Academy awarded the Nobel Prize in Physics to Wilhelm Conrad Röntgen, Professor in the University of Munich, for the discovery with which his name is linked for all time: the discovery of the so-called Röntgen rays or, as he himself called them, X-rays. These are, as we know, a new form of energy and have received the name "rays" on account of their property of propagating themselves in straight lines as light does. The actual constitution of this radiation of energy is still unknown. Several of its characteristic properties have, however, been discovered first by Röntgen himself and then by other physicists who have directed their researches into this field. And there is no doubt that much success will be gained in physical science when this strange energy form is sufficiently investigated and its wide field thoroughly explored.*

Röntgen himself did not give a Nobel lecture at that time. Due to the characteristics of x-rays – which are electromagnetic waves with wavelengths between 10 nm and 0.01 nm – and the unavailability of materials, that show sufficiently strong refraction at these wavelengths, no efficient optical devices such as lenses and mirrors can be constructed up to now. Thus, x-ray imaging techniques rely on other means to achieve this task. Although the first x-ray interferometer was built in the 1960s [9], the aforementioned phase-contrast and dark-field imaging methods have been intensively developed only since the 1990s for the x-ray regime. During that decade, Zernike's setup was directly transferred to the x-

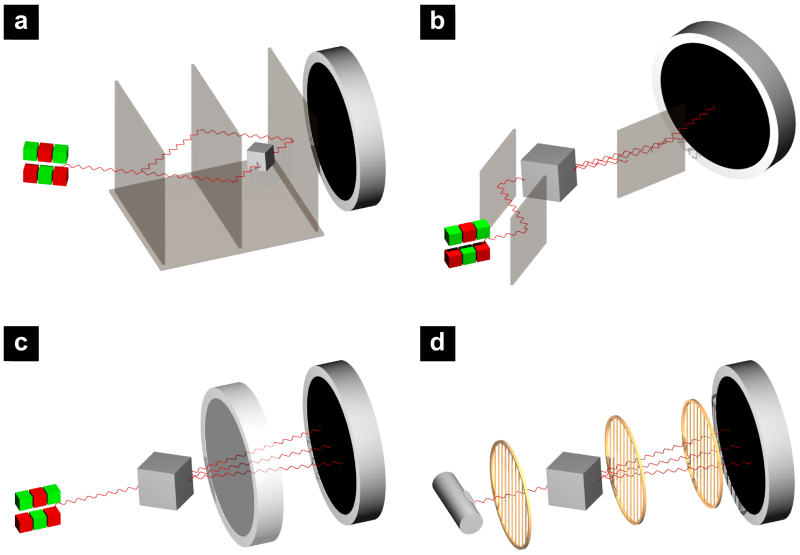

Fig. 1.2: Phase-contrast imaging techniques. a) Crystal interferometry: The incident x-ray beam is split up in two paths and recombined in front of the detector by three identical single-crystals. This produces an interference fringe pattern at the detector. The sample is located along one of the two beam paths and causes a distortion of the pattern, which is measured and allows to calculate the phase shift introduced by the sample. b) Analyzer-based imaging: An analyzer crystal is used to measure the angular dependence of the scattered waves. The incident radiation has to be filtered by a monochromator. c) Inline phase contrast: This technique exploits the effects of x-ray propagation by taking several images at different known distances from the sample. d) Grating interferometry: Similar to crystal interferometry, a well-defined pattern is imprinted on the wavefront by a grating interferometer. Deviations from reference images taken without a sample (flat field) are compared to those taken with the sample in place. This allows to calculate the differential phase shift introduced by the specimen. (Adapted from figs. 1 & 2 of [12].)

ray spectrum (see e.g. [10, 11]), but only for applications in microscopy using coherent radiation.

Nowadays, a large variety of different x-ray phase-contrast imaging techniques exists (see figure 1.2). Among them are propagation-based phase contrast [13, 14] (developed in 1995, also known as inline phase-contrast), crystal-interferometer-based phase contrast [9, 15] (developed in 1965 and refined for applicability in 1995), and diffraction-enhanced imaging [16–18] (developed in 1980 and improved in 1995, also known as analyzer-based imaging). Most of them are strongly limited to monochromatic and coherent illumination, suffer from a small field of view, or face high requirements with respect to setup stability

or photon flux. This strongly limits their applicability in a laboratory-based environment.

In contrast to these methods, x-ray grating interferometry – the method that this thesis is based on – does not face such restrictions. It is a very promising candidate to improve current imaging techniques in materials science and security scanning without the large effort of creating a completely new machine design. Instead, the existing machine design only needs to be altered to include the grating interferometer. Moreover, its potential in the field of medical diagnosis is currently evaluated [19–21].

The use of grating interferometry to avoid x-ray lenses was first proposed by Clauser and Reinsch in 1992 [22]. They already provided the theoretical treatment for interferometers consisting of two and three gratings. In 2002, David et al. developed a grating-based setup for x-rays, which was a combination of Talbot interferometry and the crystal-analyzer method [23]. The first pure Talbot interferometer for hard x-rays was reported by Momose et al. in 2003 [24]. Until 2005, only the Moiré fringes produced by grating interferometry were used for evaluation of the phase-shifting properties of the specimens. Weitkamp et al. introduced the phase stepping technique, where one of the gratings is moved sideways relative to the others and the resulting intensity changes are used to calculate the resulting signal [25]. In 2006, Pfeiffer et al. first used grating interferometry in combination with hard x-rays and a Talbot-Lau geometry at a laboratory setup with an ordinary x-ray tube instead of a synchrotron source [19, 20].

Besides transmission and phase-contrast imaging, grating interferometry also provides the dark-field contrast channel, which is well-known from visible light and electron microscopy as described above [21]. Like in visible light microscopy, it originates in fine structural changes on the micrometer scale, which scatter the x-ray photons. Without requiring high resolution detectors, dark-field radiography and tomography allow to draw conclusions about morphological parameters of sub-pixel-size structures such as their dimensions, location, and orientation [12, 26–34]. This is especially relevant in the medical field, as small detector pixels would require a significantly higher dose to keep the noise level low enough.

The ultimate goal of my PhD project was to develop a novel computed tomography technique based on the x-ray dark-field signal from grating interferometry. For that purpose, a deeper knowledge of the signal formation was required first. However, there is no simple link between sample morphology and x-ray dark-field contrast. As a foundation to understanding this connection, the following

sections will explain the physical principles of the interactions between x-rays and matter playing a role in dark-field imaging as well as the measurement technique in detail. The principles of computed tomography will be explained in section 1.5 followed by details on the current status of dark-field imaging and tomography in section 1.6.

1.1 Absorption, Refraction and Scattering Processes of Electromagnetic Waves

Although x-rays at first were believed to undergo neither scattering nor refraction at all [7, 35], soon indications were found by Charles Glover Barkla and Max von Laue that they are electromagnetic waves just as visible light [36–38]. As for all electromagnetic waves – when they pass through matter – their intensity and phase both change according to the material. In principle, one can discriminate three different processes which can be observed at object boundaries but have their origin in the material through which the rays traveled before: absorption, refraction, and reflection. Absorption is characterized by an intensity reduction in an energy range of the x-ray beam's spectrum. In the geometrical optics point of view, refraction is a change in beam direction for example at interfaces or, in general, wherever the medium changes. From a wave-optical point of view, refraction is a modification of the wavefront shape. Reflection is very weak for x-rays except below the critical angle, as the refractive index is near unity.

Absorption, refraction, and reflection are all macroscopically observable processes. Each of them is linked to another type of interaction occurring when electromagnetic waves interact with matter or elementary particles: scattering. For x-ray photon energies in the range between 10 keV and 100 keV, the relative size of the scattering particle has to be compared to $\frac{\lambda}{2\pi}$, which is bounded by $0.002\,\mathrm{nm} \lesssim \frac{\lambda}{2\pi} \lesssim 0.02\,\mathrm{nm}$. Consequently, the required particle diameter must be far below the atomic length scale. In this energy range of the electromagnetic spectrum, only scattering at elementary particles plays a role, which are electrons for all materials considered in this thesis.

When x-rays scatter at electrons, two processes can occur: Thomson and Compton scattering. The first one is elastic and the second one is inelastic, meaning that the x-ray photon energy stays constant or changes, respectively.

Compton scattering is most easily expressed relativistically in the particle image

as a collision between an x-ray photon and an electron. Depending on the deflection of electron and photon the x-ray photon energy changes. The Compton scattering cross section $\frac{\mathrm{d}\sigma}{\mathrm{d}\Omega_{\text{Compton}}}$ describes the probability of an x-ray photon being scattered in a certain spatial angle interval. It is expressed by the Klein-Nishina formula [39]:

$$\frac{\mathrm{d}\sigma}{\mathrm{d}\Omega_{\text{Compton}}} = \frac{r_0^2}{2} P^2(E_{\text{x-ray}}, \theta) \left[P(E_{\text{x-ray}}, \theta) + \frac{1}{P(E_{\text{x-ray}}, \theta)} - 1 + \cos^2\theta \right], \tag{1.1}$$

$$P(E_{\text{x-ray}}, \theta) = \frac{1}{1 + \frac{E_{\text{x-ray}}}{E_e}(1 - \cos\theta)}. \tag{1.2}$$

Here, r_0 is the classical electron radius also known as Thomson scattering length. θ specifies the scattering angle relative to the incident beam. The x-ray photon energy changes with respect to the scattering direction as follows:

$$E'_{\text{x-ray}} = E_{\text{x-ray}} P(E_{\text{x-ray}}, \theta). \tag{1.3}$$

Because of this photon energy change, the wavelength of the scattered photons deviates from the incident beam. Therefore, Compton scattering is incoherent.

Thomson scattering has its origin in the dipole-radiation of the electrons in a material, which are oscillating in the electromagnetic wave of the incoming x-ray beam [40]. This radiation has the same frequency and hence the same wavelength (elastic scattering) as the driving wave. For the purposes of this work, no free electrons need to be considered. All electrons are bound to an atom or molecule and oscillate in the atomic electrostatic potential driven by the external electromagnetic field introduced by the x-rays. Thomson scattering can be described classically by a driven harmonic oscillator model of electrons bound to an atom [41]. The Thomson differential scattering cross-section is defined as follows:

$$\frac{\mathrm{d}\sigma}{\mathrm{d}\Omega_{\text{Thomson}}} = \frac{r_0^2}{2} \left[1 + \cos^2\theta \right]. \tag{1.4}$$

The main effect of Thomson scattering inside a medium is that it introduces a phase-shift to the x-ray waves. As the oscillation frequency of the x-ray photons in the x-ray energy range in general is above several resonances of the bound electrons, the phase-shift of the x-ray waves emitted by the bound electrons relative to the incident beam is 180°. From the viewpoint of geometric scattering, this can equivalently be described by a change δ of the real part of the refractive index n relative to vacuum, $\mathrm{Re}(n) = 1 - \delta$. Consequently, Thomson scattering and geometric refraction are two sides of the same coin. For x-rays, δ is in the order of 10^{-5} and below. A detailed derivation connecting Thomson scattering and the refractive index decrement δ is given in [40]. More details on calculating δ for any given material can be found in section 2.2.2.

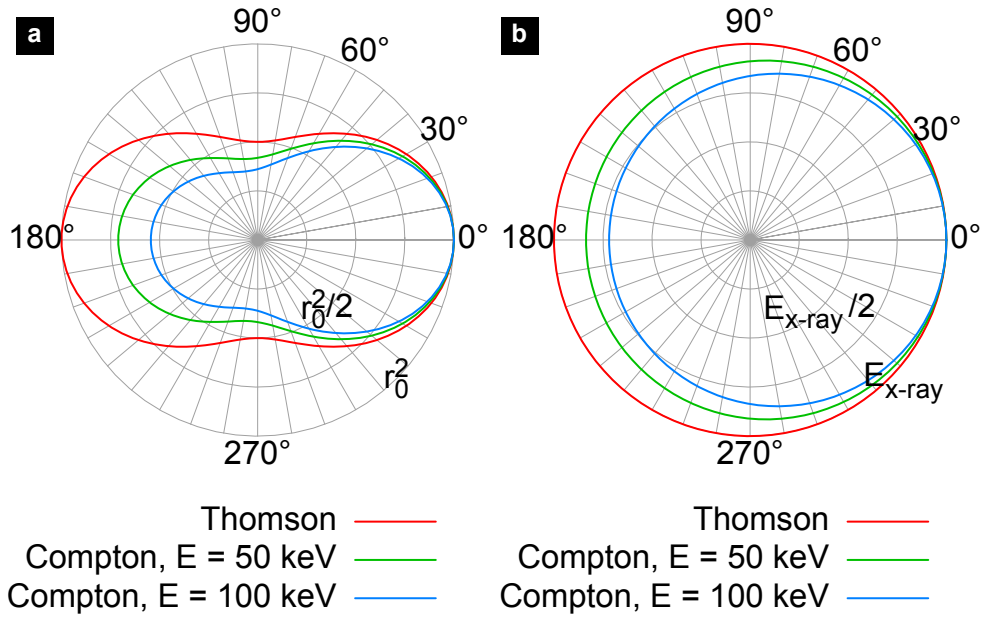

Fig. 1.3: The Thomson and Compton scattering cross-sections and x-ray photon energy change. a) The Thomson and Compton differential scattering cross-sections $\frac{d\sigma}{d\Omega}$ with respect to the scattering angle θ following from the Klein-Nishina formula. b) The energy of the scattered x-ray photon with respect to the scattering angle. Thomson scattering is valid for very low x-ray energies below the electron rest energy (511 keV). The typical photon energies in this study lie below 100 keV. Therefore, two scenarios for Compton scattering were calculated, one for 50 keV and the other at 100 keV. For the forward directions between $-10°$ and $+10°$, Compton scattering does not deviate significantly from Thomson scattering with respect to both the scattering cross-section and the energy change.

Thomson scattering can be regarded as the low-energy limit of Compton scattering (see fig. 1.3), where the latter converges towards the elastic case. This is only with respect to the change in energy, as Compton scattering is always incoherent [41]. Here, low x-ray energy means well below the electron rest energy:

$$E_{\text{x-ray}} \ll E_{\text{e}} \approx 511\,\text{keV}. \tag{1.5}$$

This is met by all experiments and numerical simulations which are described in this thesis. Especially in the forward direction, in between $\pm 10°$, the change in x-ray energy is less than 0.1 %. The analyzer grating used in grating-based phase-contrast imaging strongly limits the angular range of photons arriving at the detector. Those photons scattered outside this angular range will not arrive at the detector and thus contribute to the absorption signal. However, the small fraction of all Compton-scattered photons that arrives at the detector was scattered incoherently and does not contribute to the interference pattern measured by the grating interferometry setup. In this small angular range Compton scattering contributes a diffuse background of approximately the same energy as the incident beam. This background affects the dark-field signal but is ignored throughout this thesis as it is considered rather small.

Absorption is mainly caused by the photoelectric effect, Compton scattering and – only at very high photon energies – by pair production. In terms of a material's refractive index n, absorption is represented by its imaginary part: $\text{Im}(n) = \beta$. More details on calculating the absorption cross-section and β for any given material can be found in section 2.2.2. In the next section, after explaining its working principle, I will relate absorption and refraction to the measured quantities of x-ray grating interferometry. For x-ray dark-field imaging, refraction plays the major role.

1.2 X-Ray Grating Interferometry

In his Nobel lecture, Frits Zernike spoke about the original developments leading to his invention of phase-contrast microscopy [1]:

> *«Phase contrast» was not discovered while working with a microscope, but in a different part of optics. It started from my interest in diffraction gratings, about from 1920 on.*

It is fascinating, that even though phase-contrast imaging started from observations with diffraction gratings, this was not transferred to the field of x-rays for

such a long time. Already in 1836, William Henry Fox Talbot discovered the so-called Talbot effect, which he described the following way:

> *About ten or twenty feet from the radiant point, I placed in the path of the ray an equidistant grating [footnote: A plate of glass covered with gold-leaf, on which several hundred parallel lines are cut, in order to transmit the light at equal intervals.] made by Fraunhofer, with its lines vertical. I then viewed the light which had passed through this grating with a lens of considerable magnifying power. The appearance was very curious, being a regular alternation of numerous lines or bands of red and green colour, having their direction parallel to the lines of the grating. On removing the lens a little further from the grating, the bands gradually changed their colours, and became alternately blue and yellow. When the lens was a little more removed, the bands again became red and green. And this change continued to take place for an indefinite number of times, as the distance between the lens and grating increased. In all cases the bands exhibited two complementary colours. [42]*

What Talbot actually saw, were images of the grating, which appeared at certain distances from it. As he used polychromatic light, these distances differed depending on the wavelength. In between these locations the intensity is distributed more evenly over the field of view. Thus he saw the grating's images in changing color. These self-images are the foundations to the working principle of x-ray grating interferometry.

A typical x-ray grating interferometry setup is sketched in figure 1.4. Starting from a conventional x-ray radiography or tomography setup containing an x-ray source X, a sample S, and a detector D, grating interferometry in addition to that introduces two or three grating structures (G_0, G_1, G_2) along the optical axis. The first grating (G_0) is commonly referred to as the source grating. It ensures that the illumination of the actual grating interferometer formed by G_1 and G_2 provides high enough transversal coherence [19]. Otherwise no interference effects could be observed. Of course, if the source already provides enough coherence, like many synchrotron sources do, this grating can be omitted. G_1 introduces a periodic line pattern to the incoming beam with period p_1. The lines either modulate the wavefront's intensity or shift its phase. All setups relevant for this thesis work with a phase-shifting grating G_1. Therefore it is also called phase grating. By the fractional Talbot effect [42, 43] the phase-shift is then transferred into a well-defined intensity pattern at certain distances along the beam path behind G_1. Because of this transfer, the fractional Talbot effect does not create exact self-images and the term Lohmann images is used instead. At these spots, the intensity more or less resembles the periodicity of the phase grating. The phase gratings used for this thesis all had a duty cycle (ratio between the width of the

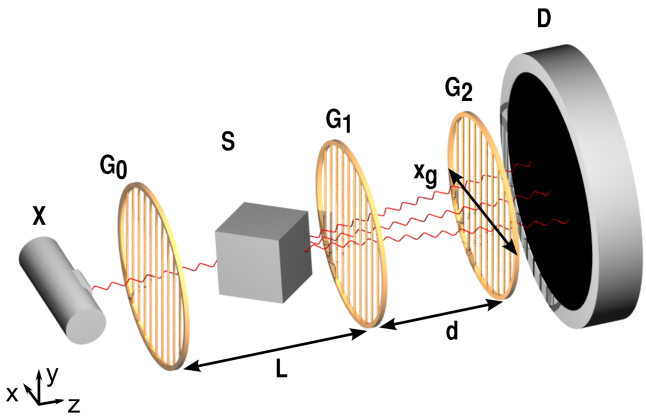

Fig. 1.4: Sketch of a typical x-ray grating interferometry setup. It consists of an x-ray source X, a sample S, the Talbot-Lau interferometer formed by the source grating G_0, the phase grating G_1 and the analyzer grating G_2, and the detector D. If the source provides sufficiently coherent illumination, the source grating can be omitted. This can typically be the case at a synchrotron, whereas x-ray tubes usually have too large focal spot sizes. The distance between G_0 and G_1 is commonly denoted by L, the distance between G_1 and G_2 by d. During measurement one grating is moved sideways. Here, this is G_2 and its position is given by x_g.

spaces and the period) of 0.5. Then, for a total phase shift of π, the resulting intensity patterns have a period which is half the one of G_1. For a total phase shift of $\pi/2$, the period is identical to p_1. The exact distances where these self-images arise, are called fractional Talbot distances. These distances also depend on the phase shift which is introduced by the lines of G_1, the x-ray wavelength λ, and the phase grating period p_1. They can be specified relative to the full Talbot distance z_T, which in a non-magnifying setup is given by:

$$z_T = \frac{2p_1^2}{\lambda}. \tag{1.6}$$

For a phase shift of $\pi/2$, intensity self-images of G_1 appear at fractions $\alpha = \frac{1}{4}, \frac{3}{4}$, etc. of the full Talbot distance z_T, for a phase shift of π at $\alpha = \frac{1}{16}, \frac{3}{16}$, and so on (cf. [43]). In a magnifying geometry with magnification $m = \frac{L+d}{L}$, where L is the distance between the source grating and the phase grating and d the distance between the phase grating and the self-image, the full and the fractional Talbot distances change accordingly:

$$z_T' = z_T \frac{L}{L - z_T}, \tag{1.7}$$

$$d = \alpha z_T'. \tag{1.8}$$

The last grating, G_2, is placed exactly at one of these positions d and its period p_2 is chosen identical to the period of the intensity pattern. Here too, the mag-

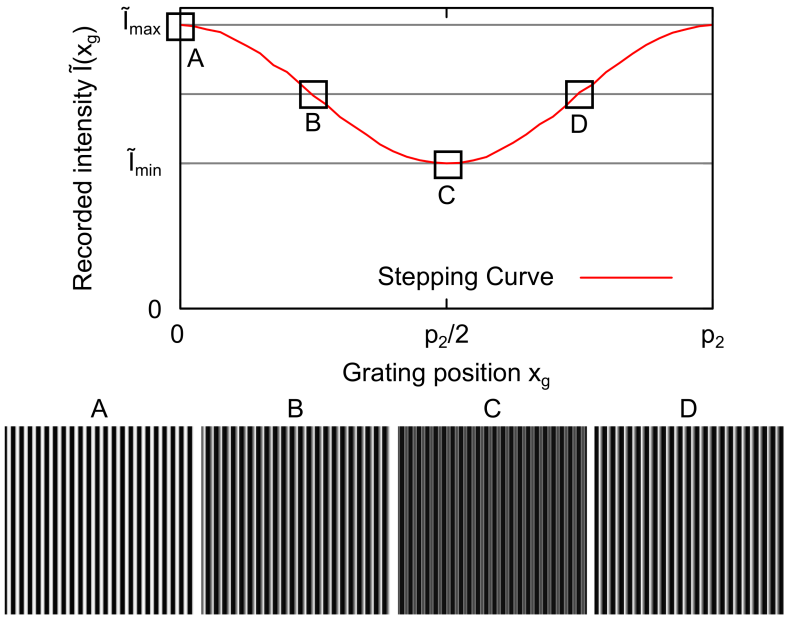

Fig. 1.5: The stepping curve. When displacing one of the gratings (here it is G_2) sideways relative to the others for the distance x_g, the recorded intensity in each detector pixel oscillates harmonically. This is used to evaluate the effects of a sample introduced into the beam. The lower row shows the intensity seen by a single detector pixel for the stepping positions A-D marked in the plot. Typically the detector pixels are a lot larger than the period of the interference pattern to keep the detector noise and, in medical scenarios, also the dose at a low level.

nification of the interference pattern has to be taken into account. The period of the interference pattern is magnified by the factor m. A good description on how to choose the parameters of such a grating interferometer can be found in [44] and a detailed discussion of different basic setup geometries is given in [12]. The interference pattern itself has a period which usually is too small to be recorded directly by a detector, unless the x-ray intensity is high enough. In tube-based setups, the required flux for a sufficiently high count rate or sufficiently low signal-to-noise ratio in each detector pixel cannot be provided by the tube. And especially for medical applications, the maximum dose applicable to the patient limits the intensity and the exposure time. Therefore, the detector pixels in tube-based setups have to be orders of magnitude larger than the interference pattern. Nevertheless, information about changes in the interference pattern can be obtained. This approach is similar to Schlieren imaging [45]. When moving one of the gratings sideways for the distance x_g in several discrete steps, the intensity recorded in each detector pixel oscillates approximately harmonically (cf. fig. 1.5). This procedure is called a stepping scan (cf. [25]). In the ideal case of a point source this curve would have a triangular profile, as the rectangular interference pattern is analyzed with a rectangular

profile grating (G_2). For the laboratory-based setups used in this thesis, the illumination is given by the source grating and, therefore, is further smoothed by another rectangular function producing a stepping curve which is section-wise parabolic.

The working principle of the grating interferometer is similar to the one of a lock-in amplifier known from electronics. There as well, a signal of known frequency is imprinted on the measured signal, which corresponds to the interference pattern created by the phase grating. The lock-in amplifier can then be used to significantly improve the signal-to-noise ratio of the original signal or to measure the phase-shift introduced by it.

Let us return to x-ray grating interferometry. When a sample is introduced into the beam path, it can influence the interference pattern and thereby the stepping curve in three ways (cf. fig. 1.6). Absorbing samples rescale the stepping curve by a constant factor. From this change, conventional attenuation contrast can be extracted. Phase-shifting samples move the stepping curve sideways. The shift of the stepping curve is directly related to the phase gradient introduced by the sample. If changes in the phase gradient contain spatial frequencies varying on larger length scales than the detector pixel pitch, this will appear as (differential) phase contrast. Specimens containing fine substructures shift the interference pattern locally in different directions and, thus, only affect the amplitude of the stepping curve while leaving its offset and phase unaltered. Calculating the changes in this amplitude serves the dark-field contrast. Both differential phase and dark-field contrast have their origin in the same physical process: refraction. Of course this is only true when looking at it from a macrosopic, ray-optics viewpoint. From a microscopic viewpoint, Thomson scattering causes the phase-shift in the specimen and thus produces both contrasts. Throughout this thesis I will use the term scattering whenever the structures causing refraction are rather fine, and the term refraction for rather coarse structural variations to distinguish between the two modalities dark-field and phase-contrast.

1.3 Signal Extraction / Raw Data Processing

With respect to grating interferometry, the term processing refers to extracting the three contrast modalities from the stepping curve on a pixel-by-pixel basis. Here, several approaches exist, two of which were used in the work described below. As each stepping curve is to a good approximation identical to a sine/cosine, the three contrast channels were either extracted by Fourier trans-

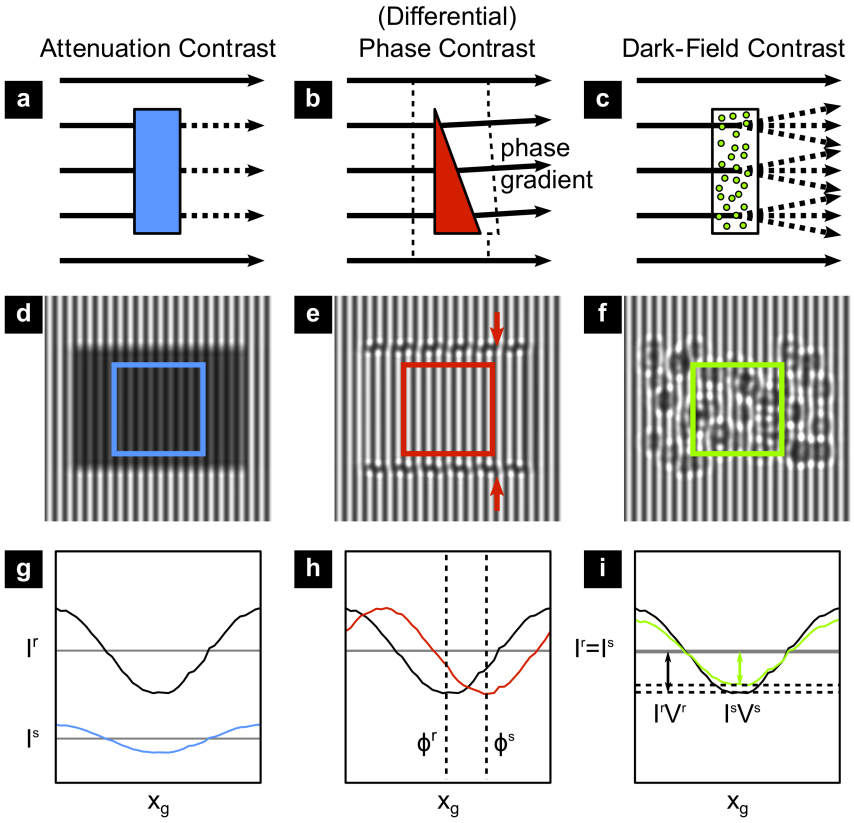

Fig. 1.6: Effects of idealized sample types. Any sample can affect the interference pattern in one of three ways, which affects the stepping curve recorded in each detector pixel. a)-c) show sketches of idealized samples. d)-f) demonstrate the effect on the interference pattern. The size of a single detector pixel is indicated by a square in each of the subfigures. g)-i) display the corresponding stepping curve. Left: Absorption rescales the curve. Middle: A sample, which introduces a phase gradient to the x-ray wavefront that varies on a length scale above the detector pixel pitch, moves the interference pattern sideways. Two example locations, where this shift becomes visible, are marked by arrows. As this shift is the same over the whole detector pixel, only the phase of the stepping curve changes (differential phase contrast). Right: If the phase gradient varies on length scales comparable to or below the detector pixel pitch, the interference pattern is locally moved sideways in different directions. This causes a reduced amplitude of the stepping curve (dark-field contrast).

forming the stepping curve and using the zeroth and first order coefficients or by least-squares-fitting of a sine and cosine. In the first case the stepping curve with ($\tilde{I}^{\mathrm{s}}$) and without ($\tilde{I}^{\mathrm{r}}$) sample is approximated by

$$\begin{aligned}\tilde{I}^{\mathrm{s/r}}(x,y;x_{\mathrm{g}}) &\approx I^{\mathrm{s/r}}(x,y) + V^{\mathrm{s/r}}(x,y) I^{\mathrm{s/r}}(x,y) \sin\left(2\pi\frac{x_{\mathrm{g}}}{p_2} + \phi^{\mathrm{s/r}}(x,y)\right) \quad (1.9)\\ &= I^{\mathrm{s/r}}(x,y)\left[1 + V^{\mathrm{s/r}}(x,y)\sin\left(2\pi\frac{x_{\mathrm{g}}}{p_2} + \phi^{\mathrm{s/r}}(x,y)\right)\right]\end{aligned}$$

and the transmission T, differential phase shift $\Delta\phi$, and dark-field D signal calculated from

$$T = \frac{I^{\mathrm{s}}}{I^{\mathrm{r}}}, \quad (1.10)$$

$$\Delta\phi = \phi^{\mathrm{s}} - \phi^{\mathrm{r}}, \quad (1.11)$$

$$D = \frac{V^{\mathrm{s}}}{V^{\mathrm{r}}}. \quad (1.12)$$

Here $I^{\mathrm{s/r}}$ is the mean intensity during the stepping process, $\phi^{\mathrm{s/r}}$ the phases, and $V^{\mathrm{s/r}}$ the visibilities (amplitudes relative to mean intensity) extracted from the stepping curves with and without sample. The images forming the reference stepping curves for each detector pixel are commonly also called flat field.

In the alternative least-squares harmonic fit approach, the approximation for the stepping curve is written as

$$\tilde{I}^{\mathrm{s/r}}(x,y;x_{\mathrm{g}}) \approx A^{\mathrm{s/r}}(x,y)\sin x_{\mathrm{g}} + B^{\mathrm{s/r}}(x,y)\cos x_{\mathrm{g}} + I^{\mathrm{s/r}}(x,y), \quad (1.13)$$

$$V^{\mathrm{s/r}}(x,y) = \frac{\sqrt{\left(A^{\mathrm{s/r}}(x,y)\right)^2 + \left(B^{\mathrm{s/r}}(x,y)\right)^2}}{I^{\mathrm{s/r}}(x,y)}, \quad (1.14)$$

$$\phi^{\mathrm{s/r}}(x,y) = \operatorname{arctan2}\left(B^{\mathrm{s/r}}(x,y), A^{\mathrm{s/r}}(x,y)\right). \quad (1.15)$$

Because of the low number of points recorded for each stepping curve (typically below 20), both methods can be regarded as equally computationally expensive. The least-squares fit allows to calculate goodness-of-fit parameters, which can then be useful for further processing of the data. These can be beneficial for example in computed tomography, which will be explained in section 1.5. The following section introduces the coordinate system convention, which is a prerequisite to all measurement techniques described thereafter.

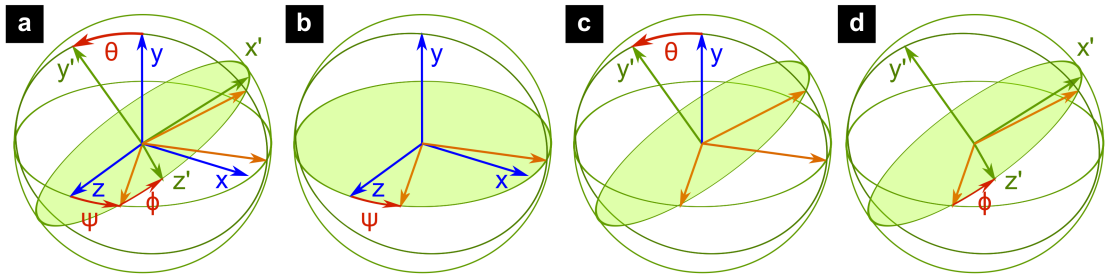

Fig. 1.7: Coordinate systems and Eulerian angles. a) Throughout this thesis, the laboratory coordinate system will be denoted by the coordinates x, y, z, whereas the coordinate system fixed to the specimen will be given by x', y', and z'. Depending on the measurement technique, the sample will be rotated around one or several different axes given by the Eulerian angles ϕ, θ, and ψ as demonstrated in b)-d). b) First the sample is rotated around the y axis by ψ. At this stage this is identical to a rotation around the y' axis. c) Then the sample is rotated around its z' axis by θ. d) Finally, another rotation by the angle ϕ follows, which is around the sample's y' axis.

1.4 Coordinate Systems and Eulerian Angles

The laboratory coordinate system used throughout this thesis will always be Cartesian and oriented in the following way: The positive z direction is given by the optical axis from the source to the detector. The x axis then is aligned horizontally and the y axis is pointing upward. Thus, the laboratory coordinate system is right-handed. The sample may be rotated around one or several different axes depending on the measurement technique. An Eulerian rotation scheme involving three rotation angles (ϕ, θ, ψ) will be used, which is shown by fig. 1.7 a). With x', y', z' being the Cartesian sample coordinate axes and x, y, z the Cartesian lab coordinate system, θ is the angle between the y and y' axis, ψ the rotation angle around y and ϕ the rotation angle around y'. Fig. 1.7 b)-d) demonstrates how the whole transformation can be decomposed into three consecutive rotations defined by these three angles. The rotation between the two coordinate systems can be expressed by the rotation matrix M:

$$\mathbf{r} = M\mathbf{r}', \tag{1.16}$$

$$M = \begin{pmatrix} l_1 & m_1 & n_1 \\ l_2 & m_2 & n_2 \\ l_3 & m_3 & n_3 \end{pmatrix}. \tag{1.17}$$

Here, the coordinates of vector $\mathbf{r}'$ are specified in the sample coordinate system and the coordinates of $\mathbf{r}$ in the laboratory coordinate system. With these

definitions, M has the following entries:

$$\begin{aligned} l_1 &= -\sin\psi\sin\phi + \cos\theta\cos\psi\cos\phi, \\ l_2 &= \sin\theta\cos\phi, \\ l_3 &= -\cos\psi\sin\phi - \cos\theta\sin\psi\cos\phi, \\ m_1 &= -\sin\theta\cos\psi, \\ m_2 &= \cos\theta, \\ m_3 &= \sin\theta\sin\psi, \\ n_1 &= \sin\psi\cos\phi + \cos\theta\cos\psi\sin\phi, \\ n_2 &= \sin\theta\sin\phi, \\ n_3 &= \cos\psi\cos\phi - \cos\theta\sin\psi\sin\phi. \end{aligned} \tag{1.18}$$

Conventional computed tomography, as described in the next section, only needs rotations around a single axis (rotation angle ϕ), whereas XTT requires more degrees of freedom for the sample orientation.

1.5 Computed Tomography

Computed Tomography was developed independently by Allan M. Cormack and Godfrey N. Hounsfield in the 1960s and beginning 1970s. Cormack discovered parts of the underlying algorithms [46, 47], while Hounsfield invented the first scanner [48]. Both were awarded the Nobel prize in Physiology or Medicine in 1979. In his Nobel lecture, Hounsfield himself described computed tomography the following way:

> *Computed tomography [...] measures the attenuation of X-ray beams passing through sections of the body from hundreds of different angles, and then, from the evidence of these measurements, a computer is able to reconstruct pictures of the body's interior. Pictures are based on the separate examination of a series of contiguous cross sections, as though we looked at the body separated into a series of thin "slices". By doing so, we virtually obtain total three-dimensional information about the body. [49]*

The physical basis of computed tomography is the Beer-Lambert law, which describes the absorption of x-rays penetrating matter:

$$T(x,y) = \exp\left(-\int \mu(x,y,z)\,\mathrm{d}z\right). \tag{1.19}$$

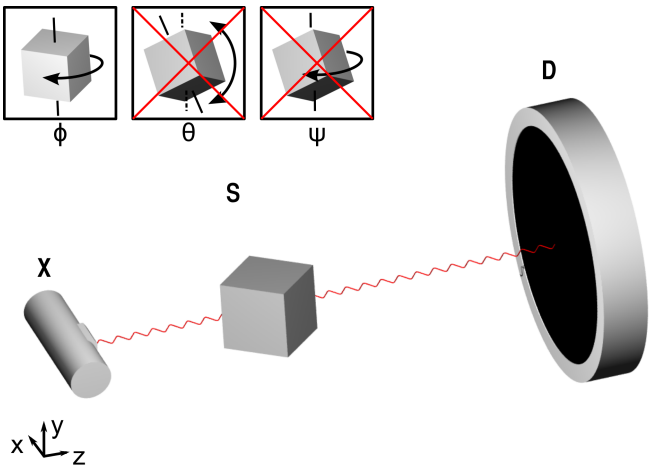

Fig. 1.8: Sketch of a typical absorption tomography setup. It contains an x-ray source X and a detector D. The specimen S is rotated around a direction perpendicular to the optical axis. Alternatively both source and detector can be rotated around the sample, which e.g. is the case for many clinical applications. The angle of rotation is denoted by ϕ.

The x-rays are assumed to travel along the z direction and μ is the attenuation coefficient, which is specific to each material and related to the imaginary part of the refractive index. It describes the absorption power with respect to the position. Mathematically, computed tomography is called an inverse problem, because it calculates the local attenuation coefficient from a set of transmission values measured for a large number of rays passing through the patient or specimen. Calculating the transmission values from given attenuation coefficients is the corresponding forward problem.

That solving this inverse problem is possible at all, is expressed by the Fourier slice theorem, which in its simplest form can be stated as follows: *The values along the one-dimensional Fourier transform of a parallel projection of an object's slice are equal to those along a line parallel to the detector through the center of the slice's two-dimensional Fourier transform.* By rotating source and detector around the sample or the sample itself (cf. fig. 1.8), it is thus possible to acquire an increasing amount of coefficients of the two-dimensional Fourier transform of each sample slice. Figure 1.9 gives a visual representation of the Fourier slice theorem. In the following, the axis of rotation will be the Cartesian y axis. From figure 1.9, one can already see that the sampling points in Fourier space are located on radial lines. Therefore, their distance increases for higher spatial frequencies. A theoretical algorithm that could be used for reconstruction starts with recording projections for all angles of rotation around the fixed axis. Mathematically, this

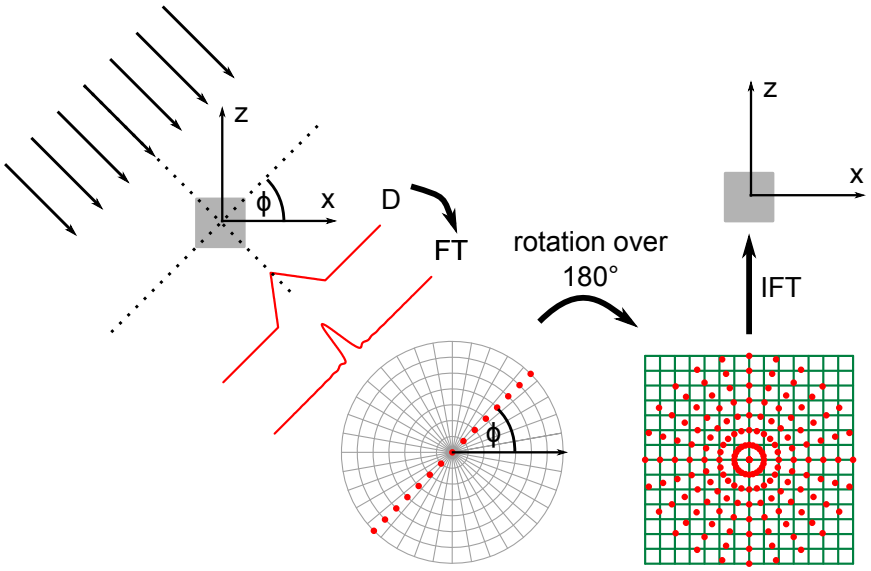

Fig. 1.9: The Fourier slice theorem. The one-dimensional intensity recorded by a single detector row D is Fourier transformed (FT). Then the result is identical to the central slice through the two-dimensional Fourier transform parallel to the detector row. This is used in analytical reconstruction methods to fill the object's Fourier space and apply the inverse Fourier transform (IFT) to retrieve the actual object (adapted from [50]).

is equivalent to the Radon transform of the object:

$$\begin{aligned} P_\phi(x,y) &= \mathcal{R}\{f(x',y,z')\}(r,\phi) \\ &= \int f(x\cos\phi + t\sin\phi, y, x\sin\phi - t\cos\phi)\,\mathrm{d}t. \end{aligned} \tag{1.20}$$

Here, $P_\phi(x,y)$ denotes the projection data and $f(x,y,z)$ is the object function. To agree with the form of (1.20), the Beer-Lambert law has to be recast by applying the logarithm:

$$-\ln T(x,y) = \int \mu(x,y,z)\,\mathrm{d}z. \tag{1.21}$$

For each projection, its Fourier transform is calculated and all the one-dimensional Fourier transforms for each height step y are summed up to get the two-dimensional Fourier transform of a slice through the object at this height, which is then inverted. This is also called inverse Radon transform ($\mathcal{R}^{-1}$). This approach only suffers from the fact that it is impossible to sample the whole Fourier space on an infinitesimally fine grid in finite time. Therefore, an approximation has to be used, which allows to limit the recording time and takes into account the increasing sampling point distances towards higher spatial frequencies.

The approximating algorithm, which nowadays is most commonly used, is Fil-

tered Backprojection (FBP). For this algorithm, it has been shown that, to produce an accurate reconstruction result with respect to sampling theory (Nyquist theorem), projections for at least a total of

$$N_\phi = w\frac{\pi}{2} \tag{1.22}$$

equidistant angles have to be taken if an object's projection spans w detector pixels [50]. As the data is recorded along radial lines through the axis of rotation, the points at which the Fourier space is sampled in general do not coincide with the equidistant Cartesian grid points of the object's discretized two-dimensional Fourier transform. FBP tackles this problem by expressing the two-dimensional inverse Fourier transform in polar coordinates (cf. [50]):

$$\begin{aligned} f(x,y,z) &= \int_{-\infty}^{\infty}\int_{-\infty}^{\infty} F(u,y,v)e^{2\pi i(ux+vz)}\,\mathrm{d}u\mathrm{d}v \\ &= \int_{0}^{2\pi}\int_{0}^{\infty} F(q\cos\phi, y, q\sin\phi)e^{2\pi iq(x\cos\phi+z\sin\phi)}q\,\mathrm{d}q\mathrm{d}\phi. \end{aligned} \tag{1.23}$$

The Jacobian of this coordinate transformation introduces a factor of q into the integral. This compensates for the larger sampling point distances towards higher spatial frequencies. Taking the symmetries of F into account, namely

$$\begin{aligned} \operatorname{Re} F(q\cos\phi, y, q\sin\phi) &= \operatorname{Re} F(-q\cos(\phi+\pi), y, -q\sin(\phi+\pi)) \\ &= \operatorname{Re} F(-q\cos\phi, y, -q\sin\phi) \\ &= \operatorname{Re} F(q\cos(\phi+\pi), y, q\sin(\phi+\pi)), \end{aligned} \tag{1.24}$$

$$\begin{aligned} \operatorname{Im} F(q\cos\phi, y, q\sin\phi) &= \operatorname{Im} F(-q\cos(\phi+\pi), y, -q\sin(\phi+\pi)) \\ &= -\operatorname{Im} F(-q\cos\phi, y, -q\sin\phi) \\ &= -\operatorname{Im} F(q\cos(\phi+\pi), y, q\sin(\phi+\pi)), \end{aligned} \tag{1.25}$$

this can be written as (cf. [50]):

$$f(x,y,z) = \int_{0}^{\pi}\int_{-\infty}^{\infty} F(q\cos\phi, y, q\sin\phi)e^{2\pi iq(x\cos\phi+z\sin\phi)}\,|q|\,\mathrm{d}q\mathrm{d}\phi. \tag{1.26}$$

With this form of the Radon inversion formula, the grids of required and recorded data points are identical and

$$F(q\cos\phi, y, q\sin\phi) = \int_{-\infty}^{\infty} P_\phi(x,y)e^{-2\pi ixq}\,\mathrm{d}x \tag{1.27}$$

is the Fourier transform of the detector row at height y. The Jacobian can be interpreted as a filter function. With these steps, the reconstruction of a single slice can be calculated as in the following listing:

Listing 1.1: The FBP algorithm (python pseudo code adapted from [50]).

```
import numpy

# Initialize volume
volume = numpy.zeros(volume_size, dtype=numpy.double)

# For every recorded angle
for angle_index in range(number_of_angles):
    # Calculate the one-dimensional Fourier transform
    # along each detector row
    F = numpy.fft.fft(projection[angle_index], axis=1)

    # Apply filter to F along horizontal axis
    F_filtered = apply_filter(F, axis=1)

    # Apply inverse Fourier transform
    f_single_angle = numpy.fft.ifft(F_filtered, axis=1)

    # Add the result to the volume
    volume += add_line_to_volume(f_single_angle)
```

Hounsfield originally used a completely different algorithm to compute the tomographic reconstruction, the Algebraic Reconstruction Technique (ART) [51]. Here, the reconstruction problem is treated by discretizing the object function f (reconstructed quantity) with respect to the position into volume elements f_j and formulating a set of equations, which in the case of absorption-based x-ray CT are given by the Beer-Lambert law but in general can realize any physical model (cf. [52]):

$$\begin{aligned} p_1 &= w_{11}f_1 + w_{12}f_2 + w_{13}f_3 + \ldots + w_{1N}f_N, \\ p_2 &= w_{21}f_1 + w_{22}f_2 + w_{23}f_3 + \ldots + w_{2N}f_N, \\ &\vdots \\ p_M &= w_{M1}f_1 + w_{M2}f_2 + w_{M3}f_3 + \ldots + w_{MN}f_N. \end{aligned} \tag{1.28}$$

Each equation corresponds to a single ray from the source to a specific detector pixel. The resulting values of these equations are given by the detector's measurement values p_i for each detector pixel and rotation step. The coefficients

of the equations w_{ij} describe the contribution of each volume element f_j to the measurement value p_i. They form the so-called system matrix. Now the aim is to invert this system matrix to calculate the reconstructed quantity, which is difficult because of its sheer size. Consequently, this is computationally a lot more expensive than FBP, which can build on very fast numerical implementations of the Fourier transform like FFTW [53]. ART applies the Kaczmarz algorithm to perform the matrix inversion iteratively (see e.g. [51]). This algorithm uses one equation out of the whole set at a time and corrects the reconstructed volume such that the detector reading agrees better with the result given by the system matrix. Each update step can be expressed mathematically by the equation (cf. [52])

$$f_j^{(k+1)} = f_j^{(k)} + \lambda_\mathrm{u} \frac{p_i - \sum_{n=1}^{N} w_{in} f_n^{(k)}}{\sum_{n=1}^{N} w_{in}^2} w_{ij}, \forall 1 \leq j \leq N. \tag{1.29}$$

This way, the technique, in each step, corrects the volume according to a single hyperplane in solution space. With $\lambda_\mathrm{u} = 1$, the i-th line of the system of equations (1.28) is fulfilled exactly after the corresponding update step. To reduce possible correction overshoot, it is beneficial to use $0 < \lambda_\mathrm{u} < 1$ (see [52]). The index of the measurement value used for a certain update step can be chosen in different ways. Commonly, this is done in random order or consecutively. One iteration of the algorithm runs through all equations of the whole set. Several iterations are required to finally converge to a solution within a given error.

For the purposes of this work, I used an improved variant of this iterative reconstruction approach, the Simultaneous Algebraic Reconstruction Technique (SART) [54]. Instead of solving for single rays, it computes the update based on all rays forming a complete detector image. Here the reconstruction algorithm can be described as follows:

Listing 1.2: The SART algorithm (python pseudo code adapted from [52]).

```
import numpy

# Initialize volume
volume = numpy.zeros(volume_size, dtype=numpy.double)

# Until convergence or - in this case - until a certain
# number of iterations is reached
for iteration in range(number_of_iterations):
    # Generate a random permutation of the set of
```

```
10      # projection indices
11      angle_indices = numpy.random.permutation(
12                                          number_of_projections)
13
14      # Iterate over all projections (in random order)
15      for random_index in angle_indices:
16          # Image projection: Compute line integrals through
17          # all detector pixels of the currently selected
18          # projection
19          temp = project(volume, angle[random_index])
20
21          # Correction image: For all detector pixels
22          # calculate the correction images from the
23          # difference to the measured projections
24          difference = projection[random_index] - temp
25
26          # Image backprojection: Distribute corrections
27          # onto grid
28          volume += update_weight * backproject(difference,
29                                          angle[random_index])
```

In this algorithm, first the reconstructed volume is initialized. This is done here by filling it with zeros, but other schemes are possible as well. For example, it is very common to use the results of Filtered Backprojection as a starting point. Then, the algorithm iterates until convergence is reached or, as in this case, a given number of iterations was performed. In the case of SART, an iteration consists of updates for every single recorded projection P_ϕ.

$$P_\phi = \{\, i \,|\, \text{measurement value } p_i \text{ was recorded under angle } \phi \}.$$

For each iteration and every recorded projection, the current volume is used to calculate a projection image, which then is compared to the actually recorded one denoted by P_ϕ. The difference then is weighed by a constant factor λ_u (`update_weight` in listing 1.2) and distributed over the volume. This updated volume is used to calculate the next projection, which then resembles the changed values in the volume. A proof for the convergence of this algorithm is given in [55]. It is beneficial to randomize the order, in which the projections are selected, as this speeds up the convergence of the algorithm (cf. [52]). Therefore, a distinct but randomly chosen angle ϕ and projection image P_ϕ correspond to each specific update step. Mathematically, each update step k to $k+1$ can be

expressed by (cf. [52]):

$$f_j^{(k+1)} = f_j^{(k)} + \frac{\sum_{i \in P_\phi} \lambda_u \frac{p_i - \sum_{n=1}^{N} w_{in} f_n^{(k)}}{\sum_{n=1}^{N} w_{in}} w_{ij}}{\sum_{i \in P_\phi} w_{ij}}, \forall 1 \leq j \leq N. \tag{1.30}$$

In the equation the forward projection is marked in red and the backward projection in blue. A difference to the Kaczmarz algorithm presented in eq. (1.29) arises: the normalization by quadratic weight factors is split up into a normalization with respect to the contributing volume elements and another one with respect to the contributing rays. In the presence of measurement errors like noise, no unique solution to the system of equations (1.28) exists. Then the algorithm starts oscillating around the unique solution, which would be the result without any errors, and only gives a result close to it [51]. Therefore, the algorithm presented above is written such that it stops after a fixed number of iterations.

Instead of rotating only around a single axis, X-Ray Tensor Tomography requires rotations around several axes and P_ϕ has to be replaced by $P_{(\phi,\theta,\psi)}$ (see chapter 4 for details). A more detailed treatment of computed tomography, available algorithms, and its implementation is given for example in [50, 51].

1.6 Current Status of X-Ray Dark-Field Methods and Open Questions

Bech et al. showed in 2009 that the x-ray dark-field signal obeys a relation similar to the Beer-Lambert law, which is the basis of conventional x-ray absorption radiography and tomography [44]:

$$D(x,y) = \frac{V^s}{V^r} = \exp\left(-\int \mu_d(x,y,z)\,\mathrm{d}z\right). \tag{1.31}$$

Here, μ_d denotes the scattering coefficient. It describes the local scattering power of the material passed by the x-ray beam under the assumption that scattering is isotropic. In their work, Bech et al. used a stair of paper to demonstrate this exponential behavior. Because of the similarity to the Beer-Lambert law, they proved that it is possible to reconstruct a scattering tomogram with conventional

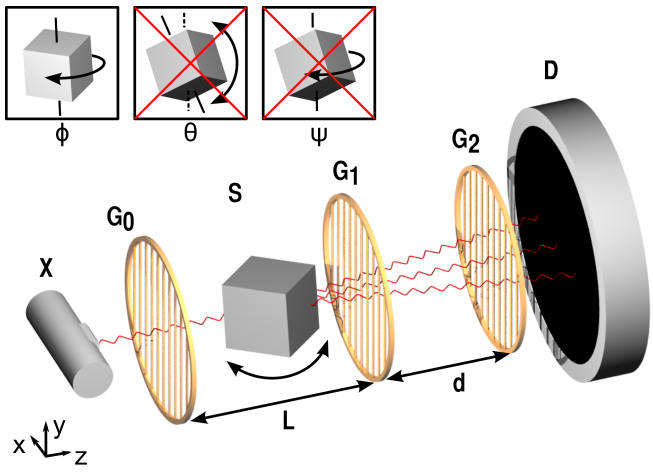

Fig. 1.10: Sketch of a typical dark-field tomography setup. It contains the same components as fig. 1.4. For tomography the sample S is rotated around the axis parallel to the grating interferometer's lines. The angle of rotation is denoted by ϕ.

reconstruction methods by simply exchanging the transmission data with the dark-field data. Figure 1.10 shows a typical setup for dark-field tomography. The only difference to imaging is the rotation of the specimen around the vertical axis throughout the experiment.

By contrast, Wen et al. [26] and Jensen et al. [56, 57], already found that the scattering and, consequently, the dark-field signal strongly depends on the relative orientation between the sample's sub-pixel structures and the grating lines of the interferometer. Jensen et al. exploited this in their radiography method called Directional Dark-Field Imaging (DDFI). The experimental principle is demonstrated in figure 1.11. Here, the sample is rotated around the optical instead of the vertical axis. Upon rotation, the intensity of the dark-field signal changes with the orientation of the sample's scattering structures relative to the grating lines (see chapter 3 for details).

Nevertheless, this dependence on the relative orientation contradicts the assumption of an isotropic scattering contribution produced by the sample when rotating it during a dark-field tomography scan. In addition to that, the changing illumination direction during a tomographic scan could also cause the local amount of scattering to change. Only isotropic structures would cause constant scattering. Thus, the simple tomographic approach for dark-field imaging is limited to isotropically scattering samples only.

In this work, I will present a reconstruction method called X-Ray Tensor Tomography (XTT), which takes the changes in scattering strength with respect to the sample orientation into account. Here, the reconstructed volume in every vol-

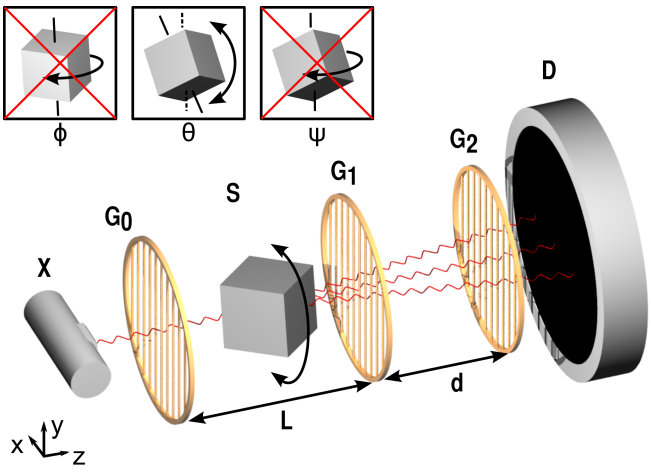

Fig. 1.11: Sketch of a typical directional dark-field radiography setup. Like for dark-field tomography, the setup contains the same components. Only the axis of rotation is different. For Directional Dark-Field Imaging, the sample is rotated around the optical axis. The corresponding angle is denoted by θ throughout this thesis.

ume element contains a tensor describing the amount of scattering with respect to the incident beam direction. From this tensor, deductions about the local sample morphology can be drawn without resolving each single structural element with the x-ray detector. One example for a practical application is computed tomography in the medical field. XTT could visualize the orientation of fine bone structures below 100 µm in thickness (e.g. trabecular bone), which can not be resolved up to now. As a consequence, this might improve detection of bone pathologies or treatment monitoring.

With these goals in mind, I first developed a numerical simulation framework, which allows to predict the outcome of a grating interferometry experiment. Chapter 2 presents the details of this numerical approach and an examination of the influence that structural sample parameters have on the measured dark-field signal. This, at the same time, was used to check the correctness of the simulations. To be able to perform XTT, an analytical model had to be developed, which in analogy to the Beer-Lambert law describes how the recorded directional dark-field image is formed from the signals originating from different locations along the beam path through the investigated object. This was done, on the one hand, on the basis of simulations and, on the other hand, by use of experiments (see chapter 3). Finally, I extended this model for X-Ray Tensor Tomography. Chapter 4 covers the development of the underlying theory and the first experimental results for a well-defined specimen gained with XTT. More future developments and possible applications based on this technique are discussed in chapter 5.

2 Numerical Simulations of X-Ray Grating Interferometry

A theory is something nobody believes, except the person who made it. An experiment is something everybody believes, except the person who made it.

Attributed to Albert Einstein

Fully understanding the novel contrast mechanisms provided by grating-based x-ray phase-contrast imaging is vital for its applications in non-destructive testing, materials science, and in the medical field. While the formation of the transmission and phase-contrast signal have been intensively investigated and understood in the recent past, a proper and profound knowledge of the formation of the dark-field imaging signal is still not available. Several studies have analyzed the influences of sample parameters and noise [26–33, 56–58]. To analyze the relation between the dark-field signal and specific morphologic sample parameters, I wrote a numerical simulation framework: pyXSFW[1]. This tool gives full flexibility with respect to the design of the specimen, whereas even specifically tailored real-world samples never provide a perfectly known geometry. With the comprehensive control of all simulated experimental parameters, predictions of the outcome of real experiments can be made.

In this chapter, I will first present the necessary theoretical background behind the simulations (section 2.1), followed by an overview of the logical structure of the simulation software (section 2.2). A first step, before reliably using this numerical approach, was to prove its validity. Therefore, I cross-checked the simulation results by comparing them to existing theoretical predictions and experimental data. This is covered in section 2.3. The results presented in this chapter strongly reflect the publication in Europhysics Letters [34].

[1] Python X-Ray Simulation Framework

2.1 Theoretical Foundations

Because of their very short wavelength, the simplest way of describing x-rays is – nomen est omen – by ray optics. However, due to the fact that grating interferometry relies on interference effects and simple ray optics is unable to describe these phenomena, the numerical simulation tool presented in this work (`pyXSFW`) is based on a Fourier optics approach. Each simulation step takes an x-ray wavefront as input, performs calculations with these input data, and returns a modified wavefront as output. A wavefront $\psi(x, y; z)$ is described by the local amplitude and phase of the electromagnetic field in a plane $z = z_1$ perpendicular to the propagation direction (z). The following sections will justify this approach by deriving it from the Maxwell equations.

2.1.1. Scalar Diffraction Theory

Our first aim is to develop a time-independent description of an electromagnetic wave, a so-called phasor representation, and relate it to the optical properties of the surrounding medium. The values of this phasor only depend on the location, but the time-dependence can easily be included later on if necessary. The following derivation closely follows the one given in chapter 1 of the book written by Schmidt [59].

Like every electromagnetic phenomenon, x-rays also obey the well-known Maxwell equations:

$$\langle \nabla, \mathbf{D} \rangle = \rho, \tag{2.1}$$
$$\langle \nabla, \mathbf{B} \rangle = 0, \tag{2.2}$$
$$\nabla \times \mathbf{E} = -\frac{\partial \mathbf{B}}{\partial t}, \tag{2.3}$$
$$\nabla \times \mathbf{H} = \mathbf{J} + \frac{\partial \mathbf{D}}{\partial t}, \tag{2.4}$$

with

$$\mathbf{D} = \epsilon_0 \mathbf{E} + \mathbf{P}, \tag{2.5}$$
$$\mathbf{H} = \frac{\mathbf{B}}{\mu_0} - \mathbf{M}. \tag{2.6}$$

Here, $\langle \cdot, \cdot \rangle$ is the Euclidian scalar product and $\cdot \times \cdot$ denotes the vector product. ∇ is the del operator. $\mathbf{E}$ denotes the electric field, $\mathbf{D}$ the electric displacement

field, **B** the magnetic flux density, **H** the magnetic field, **P** the polarization, **M** the magnetization, and **J** the free current density. $\epsilon_0 = 8.8541878 \cdot 10^{-12}\,\mathrm{Fm}^{-1}$ is the vacuum permittivity, and $\mu_0 = 4\pi \cdot 10^{-7}\,\mathrm{NA}^{-2}$ the free space permeability.

As we first want to describe electromagnetic waves propagating in free space (vacuum[2]), we can set ρ, **J**, **P**, and **M** to zero. Then we arrive at the following set of equations:

$$\langle \nabla, \mathbf{E} \rangle = 0, \tag{2.7}$$
$$\langle \nabla, \mathbf{B} \rangle = 0, \tag{2.8}$$
$$\nabla \times \mathbf{E} = -\frac{\partial \mathbf{B}}{\partial t}, \tag{2.9}$$
$$\nabla \times \mathbf{B} = \epsilon_0 \mu_0 \frac{\partial \mathbf{E}}{\partial t}. \tag{2.10}$$

To state this in separate equations for **E** and **B**, we calculate the curl of equations (2.9) and (2.10), apply the vector identity $\nabla \times (\nabla \times \cdot) = \nabla \langle \nabla, \cdot \rangle - \nabla^2 \cdot$, and obtain:

$$\nabla \times (\nabla \times \mathbf{E}) = \nabla \langle \nabla, \mathbf{E} \rangle - \nabla^2 \mathbf{E} = -\frac{\partial}{\partial t}(\nabla \times \mathbf{B}), \tag{2.11}$$
$$\nabla \times (\nabla \times \mathbf{B}) = \nabla \langle \nabla, \mathbf{B} \rangle - \nabla^2 \mathbf{B} = \epsilon_0 \mu_0 \frac{\partial}{\partial t}(\nabla \times \mathbf{E}). \tag{2.12}$$

$\langle \nabla, \mathbf{E} \rangle$, $\langle \nabla, \mathbf{B} \rangle$, $\nabla \times \mathbf{B}$, and $\nabla \times \mathbf{E}$ are already given by equations (2.7) - (2.10) and can be replaced. This yields:

$$\nabla^2 \mathbf{E} - \epsilon_0 \mu_0 \frac{\partial^2}{\partial t^2} \mathbf{E} = \mathbf{0}, \tag{2.13}$$
$$\nabla^2 \mathbf{B} - \epsilon_0 \mu_0 \frac{\partial^2}{\partial t^2} \mathbf{B} = \mathbf{0}. \tag{2.14}$$

This is the electromagnetic wave equation. It consists of six equations of the components of the electric field **E** and the magnetic flux density **B**. They are coupled by the requirements of equations (2.9) and (2.10), which for example state that $\mathbf{B} \perp \mathbf{E}$. Consequently, as soon as a solution for **E** is known, **B** is fixed, too. Each of the wave equations can be written as

$$\left(\nabla^2 - \epsilon_0 \mu_0 \frac{\partial^2}{\partial t^2} \right) U(x, y, z, t) = 0, \tag{2.15}$$

with U being a scalar field representing one distinct vector component (E_x, E_y, etc.). For convenience, the solutions to equations (2.13) - (2.15) will be expressed as complex-valued functions from now on.

[2] Because of its very low absorption at high x-ray energies, air can be treated as vacuum, too.

When equation (2.15) shall be valid for an arbitrary medium, it has to be modified accordingly. For the purpose of simulating x-ray grating interferometry, we can restrict all media to the class of linear, isotropic, dispersive, and dielectric ones. Polarization effects shall be neglected. Then equation (2.15) reads

$$\left(\nabla^2 - \epsilon\mu_0 \frac{\partial^2}{\partial t^2}\right) U(x,y,z,t) = 0, \tag{2.16}$$

where ϵ is the absolute permittivity of the medium. Isotropic in this context refers to ϵ being a scalar value. The refractive index n is related to the relative permittivity ϵ/ϵ_0 and the speed of light c to ϵ_0 and μ_0 by

$$n = \sqrt{\frac{\epsilon}{\epsilon_0}}, \quad c = \frac{1}{\sqrt{\epsilon_0\mu_0}}. \tag{2.17}$$

This leads to the formulation

$$\left(\nabla^2 - \frac{n^2}{c^2}\frac{\partial^2}{\partial t^2}\right) U(x,y,z,t) = 0. \tag{2.18}$$

Applying separation of variables, we factorize the solutions of (2.18) into a location-dependent and a time-dependent part:

$$U(x,y,z,t) = \psi(x,y,z)\chi(t), \tag{2.19}$$

with

$$\chi(t) = \exp(\pm i\omega t). \tag{2.20}$$

Here, $\omega > 0$ is the circular frequency of the solution wave. Waves with positive sign would travel back in time while those with negative sign travel forward. Consequently, the solutions we look for are of the form

$$U(x,y,z,t) = \psi(x,y,z)\exp(-i\omega t). \tag{2.21}$$

Putting this into equation (2.18) yields

$$\left(\nabla^2 + \frac{n^2\omega^2}{c^2}\right)\{\psi(x,y,z)\}\exp(-i\omega t) = 0. \tag{2.22}$$

Here, we can drop the time dependence as it can always be added again later and introduce the wavenumber $k = \frac{\omega}{c}$ and finally reach the scalar Helmholtz equation

$$\left(\nabla^2 + \frac{n^2\omega^2}{c^2}\right)\psi(x,y,z) = 0. \tag{2.23}$$

Commonly, this equation is written in terms of the wavenumber in vacuum

$$k = \frac{2\pi}{\lambda} = \frac{\omega}{c}, \tag{2.24}$$

where λ denotes the vacuum wavelength:

$$\left(\nabla^2 + k^2 n^2\right) \psi(x, y, z) = 0. \tag{2.25}$$

With this formulation, the wavenumber inside the medium is then written as $k' = kn$.

$\psi(x, y, z)$ now is the phasor part of the x-ray waves, which fully describes the optical wave's amplitude and phase with respect to the position. This is also the quantity which will be computed throughout the numerical simulation at several positions within the virtual experimental setup.

2.1.2. Wave Propagation and Fourier Optics

An essential part of the simulation algorithm will be to compute the propagation effects introduced to an arbitrary wavefront. Given a wavefront at position z_1, the wavefront at a different location z_2 has to be calculated. The Huygens-Fresnel principle gives an exact answer to this problem, which in many cases can be simplified to allow numerical calculations as well as to meet the requirements with respect to efficiency and computation time. This leads to the field of Fourier optics.

The Huygens-Fresnel principle can be derived from Rayleigh-Sommerfeld theory and stated as follows [60]:

$$\psi(x_2, y_2; z_2) = \frac{1}{i\lambda} \iint\limits_{\partial V} \psi(x_1, y_1; z_1) \frac{\exp(ik\,|\mathbf{r}_2 - \mathbf{r}_1|)}{|\mathbf{r}_2 - \mathbf{r}_1|} \cos\theta \, \mathrm{d}r_1. \tag{2.26}$$

Here, ψ denotes the phasor part of the x-ray waves and $\mathbf{r}_{1/2} = (x_{1/2}, y_{1/2}, z_{1/2})^T$. ∂V refers to the closed surface of the volume of integration V containing (x_2, y_2, z_2). V can be chosen corresponding to the locations where ψ is already known. θ is the angle between $\mathbf{r}_1 - \mathbf{r}_2$ and the normal vector on the integration surface. The z coordinates were separated from the others by a semicolon to point out that this will be the intended propagation direction later on. With positive z being the direction of propagation, the normal vector points against the propagation direction and

$$\cos\theta = \frac{z_2 - z_1}{|\mathbf{r}_2 - \mathbf{r}_1|}. \tag{2.27}$$

Therefore, (2.26) can be reformulated as follows:

$$\psi(x_2, y_2; z_2) = \frac{z_2 - z_1}{i\lambda} \iint\limits_{\partial V} \psi(x_1, y_1; z_1) \frac{\exp(ik\,|\mathbf{r}_2 - \mathbf{r}_1|)}{|\mathbf{r}_2 - \mathbf{r}_1|^2} \, \mathrm{d}r_1. \tag{2.28}$$

Several approximations to (2.28) exist. The most common ones are the Fraunhofer approximation (far field) and the Fresnel approximation (near field). Both are based on the Taylor expansion of $|\mathbf{r}_2 - \mathbf{r}_1|$ under the assumption that $(z_2 - z_1)^2 \gg (x_2 - x_1)^2 + (y_2 - y_1)^2$:

$$\begin{aligned} |\mathbf{r}_2 - \mathbf{r}_1| &= \sqrt{(z_2 - z_1)^2 + (x_2 - x_1)^2 + (y_2 - y_1)^2} \\ &= (z_2 - z_1)\sqrt{1 + \left(\frac{x_2 - x_1}{z_2 - z_1}\right)^2 + \left(\frac{y_2 - y_1}{z_2 - z_1}\right)^2} \\ &= (z_2 - z_1)\left[1 + \frac{1}{2}\left(\frac{x_2 - x_1}{z_2 - z_1}\right)^2 + \frac{1}{2}\left(\frac{y_2 - y_1}{z_2 - z_1}\right)^2 + \dots\right]. \end{aligned}$$

For the Fresnel approximation, the occurrence of $|\mathbf{r}_2 - \mathbf{r}_1|$ in the denominator is approximated by using the zeroth order term only and the occurrence in the complex exponential by using zeroth and first order. This can be justified by the strong dependence of the complex exponential in eq. (2.28) on the actual value of its argument, whereas the linear denominator stays almost constant throughout the whole integration path. Consequently, the Fresnel approximation reads

$$\psi(x_2, y_2; z_2) = \frac{e^{ik(z_2 - z_1)}}{i\lambda(z_2 - z_1)} \iint_{z=z_1} \psi(x_1, y_1; z_1) e^{ik\frac{(x_2 - x_1)^2 + (y_2 - y_1)^2}{2(z_2 - z_1)}} \,\mathrm{d}x_1 \mathrm{d}y_1. \tag{2.29}$$

The surface of integration in this case is chosen such that it reaches from the plane $z = z_1$ – where the input wavefront is defined – to infinity in the half-space containing z_2. Hence the only contributions to the integral come from the plane $z = z_1$ and the integral is defined for every ψ with compact support on this plane. The Fresnel approximation is valid only for small angles of diffraction with respect to the optical axis. Therefore, it is equivalent to the paraxial approximation [60].

The Fraunhofer approximation follows from the additional assumption

$$z_2 - z_1 \gg \frac{k(x_1^2 + y_1^2)_{\max}}{2} \tag{2.30}$$

and simplifies the Fresnel approximation one step further:

$$\psi(x_2, y_2; z_2) = \frac{e^{ik(z_2 - z_1)} e^{i\frac{k(x_2^2 + y_2^2)}{(z_2 - z_1)}}}{i\lambda(z_2 - z_1)} \iint_{z=z_1} \psi(x_1, y_1; z_1) e^{-i\frac{k(x_2 x_1 + y_2 y_1)}{(z_2 - z_1)}} \,\mathrm{d}x_1 \mathrm{d}y_1. \tag{2.31}$$

For the purposes of this work, the Fresnel approximation is the appropriate one. The propagation distances are around 1 m and the mean x-ray energy approximately 50 keV meaning $k \approx 2.5 \cdot 10^{11}\,\mathrm{m}^{-1}$. This would limit all investigated setup components to the nanometer range to fulfill (2.30), which is for example far below the structural dimensions of the gratings.

The Fresnel diffraction integral can be interpreted as a convolution with the free-space propagator function

$$H(x, y; \Delta z) = \frac{e^{ik\Delta z}}{i\lambda\Delta z} e^{ik\frac{x^2+y^2}{2\Delta z}}, \tag{2.32}$$

where Δz is the propagation distance. Direct evaluation of this convolution is possible and is also part of the simulation framework presented below. However, this does not give full flexibility with respect to the discretization of the wavefront throughout the whole simulation. While the grid size has to be kept constant, it is possible to change the grid spacing when the Fresnel integral is reformulated appropriately. There are basically two ways to achieve this, called two-step propagation and angular spectrum propagation (cf. [59]), where both involve two Fourier transforms but different computations in between.

To make it easier to understand the different computational steps, an operator notation is very handy. Here, we use the notation from [59]:

$$\mathcal{Q}[c, x', y']\{\psi(x, y)\} \equiv e^{i\frac{k}{2}c(x'^2+y'^2)}\psi(x', y'), \tag{2.33}$$

$$\mathcal{V}[b, x', y']\{\psi(x, y)\} \equiv b\psi(bx', by'), \tag{2.34}$$

$$\mathcal{F}[x', y', f_x, f_y]\{\psi(x, y)\} \equiv \int_{-\infty}^{\infty} \psi(x', y') e^{-i2\pi(f_x x' + f_y y')}\,\mathrm{d}x'\mathrm{d}y', \tag{2.35}$$

$$\mathcal{F}^{-1}[f'_x, f'_y, x, y]\{\psi(f_x, f_y)\} \equiv \int_{-\infty}^{\infty} \psi(f'_x, f'_y) e^{i2\pi(f'_x x + f'_y y)}\,\mathrm{d}f'_x\mathrm{d}f'_y, \tag{2.36}$$

$$\mathcal{Q}_2[d, x', y']\{\psi(x, y)\} \equiv e^{i\pi^2\frac{2d}{k}(x'^2+y'^2)}\psi(x', y'). \tag{2.37}$$

With this operator notation, the Fresnel integral can be reformulated according

to the two-step propagation approach as follows (cf. [59]):

$$\begin{aligned}\psi(x_2, y_2; z_2) \;=\; & \mathcal{Q}\left[\frac{1}{z_2 - z_1^a}, x_2, y_2\right] \mathcal{V}\left[\frac{1}{\lambda(z_2 - z_1^a)}, f_x^a, f_y^a\right] \\ & \circ\; \mathcal{F}[x_2, y_2, f_x^a, f_y^a]\, \mathcal{Q}\left[\frac{1}{z_2 - z_1^a}, x_1^a, y_1^a\right] \\ & \circ\; \mathcal{Q}\left[\frac{1}{z_1^a - z_1}, x_1^a, y_1^a\right] \mathcal{V}\left[\frac{1}{\lambda(z_1^a - z_1)}, f_{x1}, f_{y1}\right] \\ & \circ\; \mathcal{F}[x_1, y_1, f_{x1}, f_{y1}]\, \mathcal{Q}\left[\frac{1}{z_1^a - z_1}, x_1, y_1\right] \{\psi(x_1, y_1; z_1)\}.\end{aligned} \tag{2.38}$$

The composition operator in this and all following equations is denoted by $\circ$. As can already be deduced from its name, two-step propagation first calculates a temporary wavefront at an intermediate plane (denoted by x_1^a, y_1^a, z_1^a, ...) and then propagates to the target plane. This is reflected by the repetition of the composite operator $\mathcal{QVFQ}$. The location of the intermediate plane can be found from the boundary conditions given by the grid spacings in the initial and the final plane, δ_1 and δ_2. The magnification m between these two planes then is (see [59]):

$$m = \frac{\delta_2}{\delta_1} = \left|\frac{z_2 - z_1^a}{z_1^a - z_1}\right|. \tag{2.39}$$

This also defines the location of the intermediate plane. One can choose arbitrarily from two solutions. The numerical implementation always uses the intermediate plane, which is between z_1 and z_2.

The angular spectrum representation A of a wavefront ψ is given by its two-dimensional in-plane Fourier transform (cf. [60]):

$$A\left(\frac{\alpha_x}{\lambda}, \frac{\alpha_y}{\lambda}\right) = \iint_{-\infty}^{+\infty} \psi(x_1, y_1; z_1) e^{-i2\pi\left(\frac{\alpha_x}{\lambda}x + \frac{\alpha_y}{\lambda}y\right)} \,\mathrm{d}x\mathrm{d}y. \tag{2.40}$$

Each coefficient of the Fourier transform is reinterpreted as the amplitude and phase of a plane wave traveling in a direction given by the direction cosines α_x and α_y. These plane waves can be propagated separately, which is identical to evaluating the convolution with the free-space propagator from eq. (2.32) in Fourier space. In this thesis, I use the term angular spectrum propagation only for the modified variant, which allows to rescale the grid sizes between the source and target plane. For this variant, the Fresnel integral is written as follows

(cf. [59]):

$$\begin{aligned}\psi(x_2, y_2; z_2) &= \mathcal{Q}\left[\frac{m \pm 1}{m(z_2 - z_1)}, x_2, y_2\right] \mathcal{F}^{-1}\left[f_{x1}, f_{y1}, \mp\frac{x_2}{m}, \mp\frac{y_2}{m}\right] \\ &\circ \quad \mathcal{Q}_2\left[\pm\frac{z_2 - z_1}{m}, f_{x1}, f_{y1}\right] \mathcal{F}[x_1, y_1, f_{x1}, f_{y1}] \\ &\circ \quad \mathcal{Q}\left[\frac{1 \pm m}{z_2 - z_1}, x_1, y_1\right] \left(\mp\frac{1}{m}\right) \{\psi(x_1, y_1; z_1)\}. \end{aligned} \tag{2.41}$$

Here, both signs of m give a valid solution. The implementation of this propagation method also automatically splits the complete propagation distance into smaller parts if necessary. A detailed description of this multi-step approach can be found in [59]. All computational steps represented by the single operators can easily be parallelized to speed them up or are already available in very fast implementations like the Fourier transform library *FFTW* [53].

2.2 Numerical Implementation (pyXSFW)

To simulate x-ray grating interferometry experiments numerically, I started developing an object-oriented software framework. It is called `pyXSFW` and written in python with parallelized extensions in C++. Because of its object-oriented approach it can be extended flexibly or adapted to fit to any possible future application. Fig. 2.1 shows an overview of the main classes forming the framework. There exist three main types of classes: Simulation components, propagators, and a wavefront class. Simulation components represent actual experimental setup parts and are subclasses of `SimulationComponent`, which defines common attributes and methods of all components. For example, in the case of grating interferometry, these required classes would be a source, the gratings, different types of samples and a detector. Propagators are used to connect the different components by free-space propagation steps. All numerical operations are performed on a `Wavefront` object, which is hidden from the user most of the time and basically contains a two-dimensional array representing a wavefront in a plane perpendicular to the propagation direction at a location along the x-ray beam path. The x-ray energy and the current position along the beam path are stored here as well. Several convenience methods allow for example to transform the wavefront to Fourier space and back. The simulation's Cartesian coordinate system is right-handed with the z axis pointing in the direction of propagation, the x axis aligned horizontally and the y axis pointing upward (cf. section 1.4). `Material` is a helper class which provides the complex refractive index of elements and compound materials for any given x-ray energy.

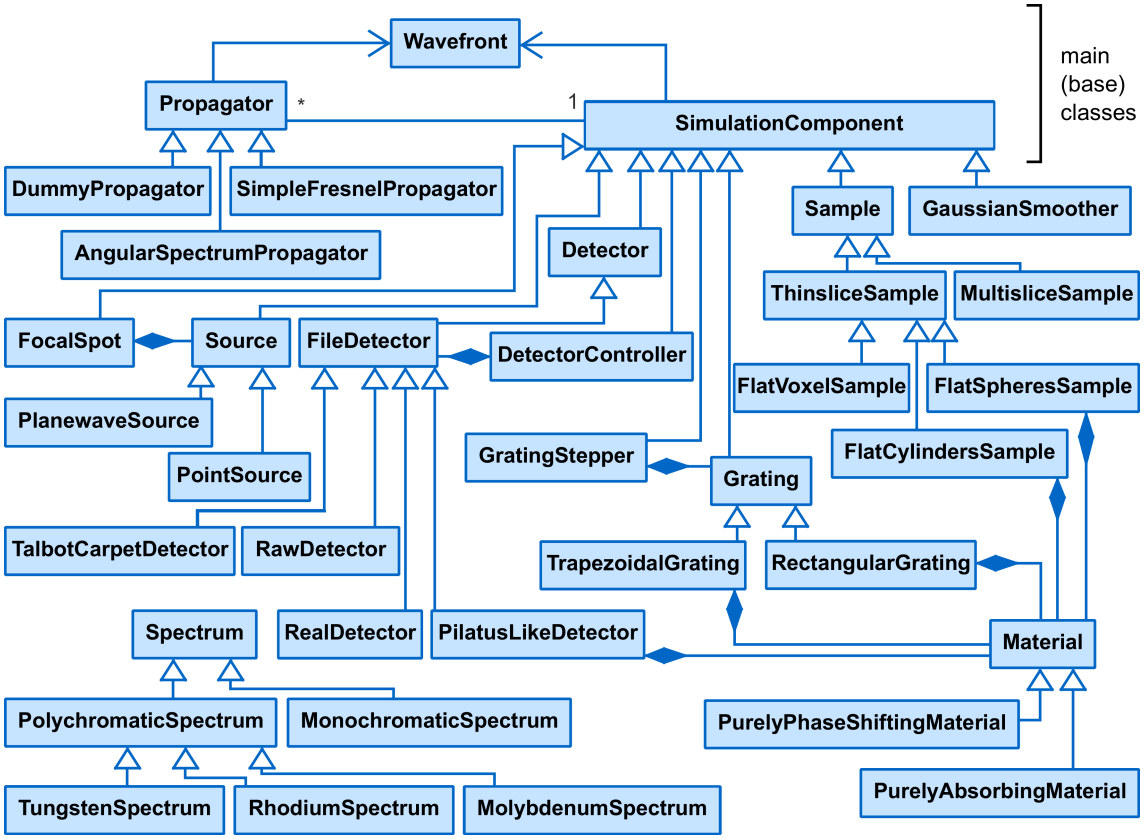

Fig. 2.1: UML class diagram of the numerical x-ray simulation framework (pyXSFW). The central classes are `Wavefront`, `SimulationComponent`, and `Propagator`. A `Wavefront` object stores the actual pixels of a wavefront, its position, x-ray energy, and grid spacing. It also offers several methods for convenience, e.g. to transform the representation of the wavefront to Fourier space and back. `SimulationComponent` is the superclass for all experimental setup components. The subclasses of `Propagator` implement different propagation methods as described in section 2.1.2.

The available propagation methods in this simulation framework reach from a simple implementation of the Fresnel integral without any flexibility (`SimpleFresnelPropagator`) over the two-step propagation approach to the angular spectrum propagation method (cf. section 2.1.2). Another type of propagator was added to the simulation framework, which only connects consecutive simulation components, but does not perform any actual propagation and is therefore called `DummyPropagator`. It is especially useful as a fast replacement of another propagator when checking the output of a certain setup component, because no positions have to be changed. The set of available setup components consists of two types of sources, a source emitting a plane wave and a point source, a variety of specialized sample types, gratings and detectors. All existing detector classes store their recorded images in a HDF5 file [61], whose filename is specified when creating the detector object. The two classes `GratingStepper` and `DetectorController` both play a special role among the available setup components. A `DetectorController` object evaluates the steps a `Wavefront` object has undergone since its creation by the source and modifies the controlled detector output path accordingly. The `GratingStepper` splits up the logical path of a `Wavefront` through the simulated scenario. For each iteration of the specified stepping scan, a copy of the input wave is created. Then, the grating controlled by the stepper is moved to the correct position and the simulation is continued for each step separately. The `DetectorController` eventually reacts on the presence of a grating stepper such that for each step every single resulting detector image is stored at a separate location in the output file.

Most of the computationally expensive methods provided by `pyXSFW`'s classes use parallelization with POSIX threads (pthreads) as well as the parallelized variant of *FFTW* wherever applicaple to reduce computation time. In the following sections the most important classes provided by `pyXSFW` will be described shortly. An in-depth description of every single class of the simulation framework is beyond the scope of this thesis. Please refer to the extensively documented electronic copy of the software, which can be obtained via the following website: `http://www.e17.ph.tum.de/`.

2.2.1. Simulating Different Source Types

The simplest type of source emits a plane wave, which is represented in the simulation by a wavefront with identical amplitude and phase in all locations. The `PlanewaveSource` class creates such an instance of `Wavefront` and normalizes its integral intensity over the simulated grid area to 1. The initial phase is

zero, meaning that the imaginary part of the wavefront is zero everywhere. The two-dimensional Fourier transform of this wavefront is strongly bandlimited as it only contains one delta peak at frequency zero.

Apart from this rather simple type of source, `pyXSFW` also offers a point source emitting spherical waves to simulate divergent setup geometries. Simulating a point source at its origin is rather tricky:

> *The field [of a point source] has a Fourier spectrum that is constant across all spatial frequencies. This means that it has infinite spatial bandwidth, which is unusual because most optical sources are spatially bandlimited. The infinite spatial bandwidth is a problem for the discretely sampled and finite-sized grid that we must use in computer simulations. [...] Therefore a bandlimited version of a point source must suffice. The point source in the simulation must have a finite spatial extent. [59]*

The point source implementation in `pyXSFW` follows the approach presented in [59]. It basically consists of calculating an analytical expression from the wavefront of a point source at a given distance, which is then propagated back to the location of the source. This gives an approximate expression for the point source, which can be discretized. Because the wavefront spreads out when propagating away from the source location, an absorbing boundary is added to avoid numerical wrap-around. This aperture is located a distance Δz away from the source and has dimension D_A. Both values have to be specified when creating an instance of the `PointSource` class. Otherwise those parts of the wavefront leaving the simulated area at one side would enter it on the opposite side again. To avoid aliasing effects with respect to the phase of the point source wavefront a Gaussian is added, which smears out the borders of the aperture slightly. A detailed derivation can be found in [59]. Here, I only state the result:

$$\begin{aligned}\psi_{\text{point source}}(x_1, y_1) &= A e^{-i\frac{k}{2\Delta z}(x_1^2+y_1^2)} e^{i\frac{k}{2\Delta z}(x_c^2+y_c^2)} e^{-i\frac{k}{\Delta z}(x_c x_1 + y_c y_1)} \\ &\times \left(\frac{D_\mathrm{A}}{\lambda\Delta z}\right)^2 \operatorname{sinc}\left[\frac{D_\mathrm{A}(x_1-x_c)}{\lambda\Delta z}\right] \operatorname{sinc}\left[\frac{D_\mathrm{A}(y_1-y_c)}{\lambda\Delta z}\right] \\ &\times e^{-\left(\frac{D_\mathrm{A}}{4\lambda\Delta z}\right)^2 (x_1^2+y_1^2)}.\end{aligned} \tag{2.42}$$

In this equation, A is an arbitrary amplitude of the wavefront and $\operatorname{sinc} x = \frac{\sin \pi x}{\pi x}$. As the `PointSource` class usually normalizes the integral intensity of the created wavefront, A is calculated implicitly. x_c and y_c specify the position of the source and are set to zero in the numerical implementation.

In order to simulate realistic tube sources, the subclasses of `PolychromaticSpectrum` provide x-ray emission spectra in the energy range between 1 keV and 150 keV for a number of different anode materials. The underlying algorithm is an adapted version of Spektr [62], which does allow to calculate not only a tungsten spectrum but also those generated by molybdenum and rhodium.

2.2.2. Calculation of Material Properties

If one is not interested in simulating experimental setup components with ideal optical properties only, this requires an exact calculation of their complex refractive index $n = 1 - \delta + i\beta$ at any given x-ray energy. This functionality is provided by the `Material` class and its subclasses. They calculate β and δ separately for the simulated materials.

The values for β are calculated with an adapted version of *mucal* written by Bandyopadhyay and Segre [63] from the absorption coefficient μ using

$$\beta = \frac{\mu\lambda}{4\pi} = \frac{\rho N_A \lambda}{4\pi A}\sigma_a \tag{2.43}$$

with the atomic density ρ, Avogadro's number N_A, the atomic mass number A and the absorption cross-section per atom σ_a (cf. [40]). *mucal* provides tabulated values of absorption edges, the atomic weight, atomic density, coherent and incoherent scattering cross-sections and allows to compute the absorption cross-section from fit curves for every element with an atomic number $Z \in \{1, \ldots, 83, 86, 90, 92, 94\}$.

The `Material` class extends these features by allowing to calculate the decrement of the real part of the refractive index δ, too. These values are calculated from the material's density ρ, its atomic number Z and mass m_A using the relation

$$\delta = \frac{Z\rho r_0 \lambda^2}{2\pi m_A} \tag{2.44}$$

(cf. [40] and section 1.1). Here, r_0 denotes the classical electron radius or Thomson scattering length (cf. section 1.1). Only near absorption edges, the calculated values will deviate from the correct solution.

The only parameters required to compute the complex refractive index for an element – apart from the x-ray wavelength, physical constants, and tabulated values – are the element's chemical formula and the material's density. For

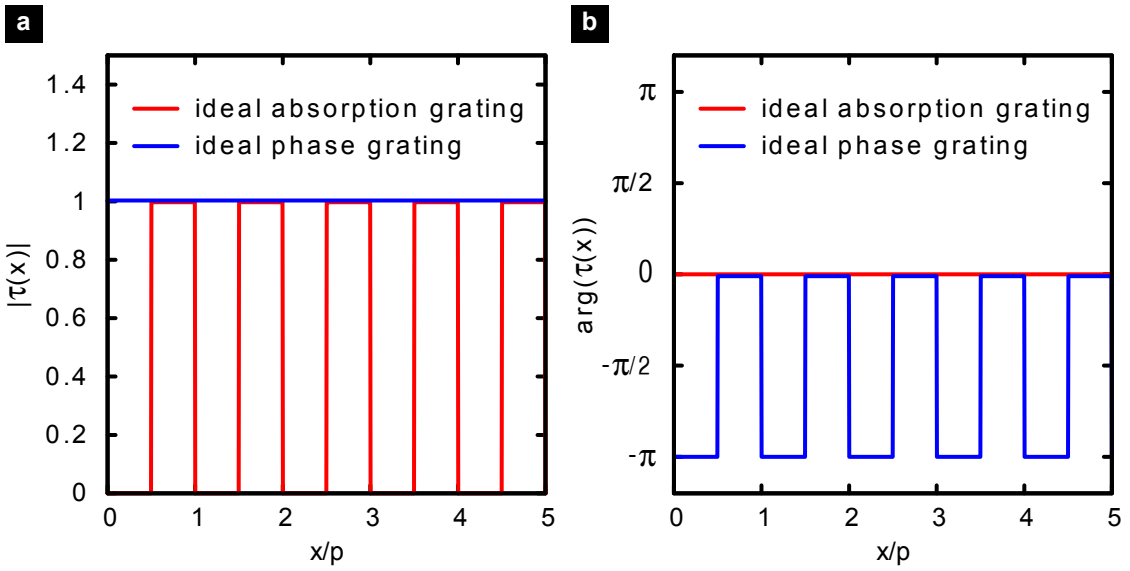

Fig. 2.2: Cross-sections of the ideal complex amplitude transmission functions τ of an absorbing and a phase shifting grating. Both the absolute value $|\tau(x)|$ and the phase shift $\arg\tau(x)$ introduced by the gratings are shown in a) and b), respectively. The absorption grating (red) completely absorbs x-rays with its lines, whereas the spaces leave the intensity unaltered. It also shows no variations with respect to the phase. The phase grating (blue) introduces a phase shift of $-\pi$ with its lines and leaves the x-ray intensity unaltered. The scale of the x axis is relative to the grating period p.

compounds, δ and β are calculated as a weighted sum of the respective values of the compound's constituents. Here, instead of a single element, a chemical sum formula can be specified. In this case, β and δ of the compound are calculated (cf. [40]) from the mass densities ρ_j of the specified elements, their refractive indices, and the mass density ρ of the compound using

$$\mu = \rho \sum_j w_j \left(\frac{\mu_j}{\rho_j} \right), \tag{2.45}$$

and

$$\delta = \rho \sum_j w_j \left(\frac{\delta_j}{\rho_j} \right). \tag{2.46}$$

Here, w_j is the atomic weight fraction of each component.

2.2.3. Numerical Implementation of Gratings

The effects of the gratings in the simulation framework are taken into account by representing them as two-dimensional, infinitesimally thin, absorb-

ing, and phase shifting objects. Their optical properties are calculated using the `Material` class instantiated with the corresponding chemical formula and mass density. The effects of these gratings are calculated fastest by multiplying the incoming wavefront in real space with the complex amplitude transmission function τ of the grating (projection approximation). τ is calculated the following way:

$$\tau(x,y) = \exp\left(i\frac{2\pi}{\lambda}\int (n(x,y,z)-1)\,\mathrm{d}z\right). \tag{2.47}$$

Figure 2.2 shows the absolute value and the phase of two typical transmission functions for ideal purely absorbing or phase shifting gratings with rectangular profile. As long as multiple interactions of photons with the grating structures can be neglected, this approach produces a good approximation to the exact result. For x-rays this definitely can be assumed. Only for x-ray beams with strong divergence, errors will be introduced, because the beam does not pass the grating parallel to its structures.

The two grating types currently provided by `pyXSFW` are `RectangularGrating` and `TrapezoidalGrating`. The latter allows to change the grating profile freely between the two extreme cases of rectangular and triangular. Although not used for the studies presented here, different grating shapes appear to have favorable properties concerning the Talbot effect and this will certainly be helpful for future examinations.

2.2.4. Detectors

Up to now, only a variety of strongly idealized detectors exists in `pyXSFW`. They all are derived from the `FileDetector` class and store their results as HDF5 [61] files in the file system. The `RawDetector` stores the plain complex-valued wavefront, while the `RealDetector` first computes the intensities $I = |\psi|^2$ from the amplitude values and stores them instead. In addition to calculating intensity values, the `PilatusLikeDetector` weighs the intensities with the absorption of a silicon layer and integrates them over each single detector pixel area (rebinning). Both the silicon thickness and the detector pixel size can be specified. The results are the intensities as they would be measured with a coarse detector resolution, typically much smaller than the one of the grid used inside the simulation. Finally, the `TalbotCarpetDetector` records a Talbot carpet, the intensity at a given height step y as it develops with the distance to a certain point along the beam path. Typically, this kind of detector is put downstream from a grating.

2.2.5. Samples

A large variety of different specimens can be simulated flexibly. They all are represented by subclasses of `Sample`. If no fitting sample class exists, simply a new subclass of `Sample` has to be created, which then can be tailored to the specific needs. Among the already existing classes is `FlatVoxelSample`, which takes a three-dimensional volume of index values. Each index points to an entry in a list containing material definitions and represents a specified material. From the refractive indices specified by this list, the complex transmission function of the whole volume is calculated. Although specified in three dimensions, the sample is assumed flat (projection approximation), when it comes to calculating its effect on the incoming wavefront.

If computation time does not play a role and the setup geometry makes it necessary, `MultisliceSample` can be used to avoid the projection approximation. Here, the propagation through the sample is calculated in equidistant steps. Effectively, the whole sample is split in several slices with propagation steps in between and each slice is represented by its transmission function. Hence the name.

For the results presented below the `FlatSpheresSample` was used. It simulates a number of spheres, whose positions are read from a text file, computes their complex transmission function (projection approximation), and applies it to the input wavefront. This is equivalent to thinking of the sample as an infinitesimally thin slice. The class also allows to create a random distribution of spheres and store it to a text file, which can be read in again later on during a simulation.

2.2.6. Sampling Constraints and Choice of Simulation Parameters

A correct choice of the main numerical simulation parameters – grid spacing δ and grid size N – can be quite hard, especially if the amount of memory and computing power is limited. A good treatment of this topic can be found in [59]. Here, only the key steps of choosing these parameters shall be presented.

One of the main challenges is posed by correctly sampling the quadratic phase factors appearing in the implementations. As the phases of the operators $\mathcal{Q}$

and $\mathcal{Q}_2$ (cf. equations (2.33) and (2.37)) oscillate at higher and higher frequency towards the boundaries of the simulated area, it has to be ensured that the sampling grid points lie close enough to each other to avoid aliasing.

This directly follows from the Nyquist sampling criterion and can be expressed by the condition (cf. [59])

$$N \geq \frac{\lambda \Delta z}{\delta_1 \delta_2}, \tag{2.48}$$

posed by $\mathcal{Q}_2$, with Δz being the propagation distance. δ_1 and δ_2 refer to the grid spacing in the input and output plane, respectively. Basically the same condition applies for the `SimpleFresnelPropagator`. The condition for $\mathcal{Q}$ can be computed in a similar manner (see [59] for details):

$$\left| \delta_2 - \left(1 + \frac{\Delta z}{R}\right) \delta_1 \right| \leq \frac{\lambda \Delta z}{D_1}. \tag{2.49}$$

Here R is the radius of curvature of an idealized spherical input wavefront and D_1 is the source aperture size.

Plane waves exhibit infinitesimal extent in Fourier space. Consequently they are strongly bandlimited and (2.48) can be ignored confidently. If $\delta_2 = \delta_1$, the same is true for (2.49), because its left side becomes zero, as $\left(1 + \frac{\Delta z}{R}\right) = 1$, and the right side is positive and the inequality is always fulfilled.

In addition to (2.48) and (2.49), two more conditions have to be met, which are caused by the plain propagation geometry, that is by diverging partial waves and finite grid sizes in the input and output plane. Here, only a rough estimation for a simple set of boundary conditions can be given. Its validity should always be checked for each simulated geometry for a case with a well-known result. We assume that the input wavefront is limited by an aperture of size D_1 and the output wavefront shall be examined in the area D_2 only.

First, it has to be ensured that the frequency bandwidth of the input wavefront does not restrict the wavevector components present in the beam. The spatial frequency components of the input wavefront can be interpreted as the angular spectrum content of the wavefront (angular spectrum formulation). Each frequency then corresponds to a plane wave component of the input wave traveling in a direction defined by the two direction cosines α_x and α_y:

$$\alpha_x = \lambda f_x, \quad \alpha_y = \lambda f_y. \tag{2.50}$$

The Nyquist theorem then states that, in order to resolve the maximum spatial frequency and, at the same time, the maximum angle, the grid spacing δ_1 is

limited by

$$\delta_1 \leq \frac{\lambda}{2\alpha_{\max}}. \tag{2.51}$$

The direction cosine $\alpha_{\max}$ is given by the propagation geometry, the grid spacing in the output plane δ_2 and the input and output aperture sizes D_1 and D_2. After examining the geometry in detail, we obtain (see [59]):

$$\delta_2 \leq -\frac{D_2}{D_1}\delta_1 + \frac{\lambda \Delta z}{D_1}. \tag{2.52}$$

Second, it has to be ensured that each single wave component, even those that deviate most from the optical axis, do not wrap around the finite simulated area. This results in

$$N \geq \frac{D_1}{2\delta_1} + \frac{D_2}{2\delta_2} + \frac{\lambda \Delta z}{2\delta_1 \delta_2}. \tag{2.53}$$

Please refer to [59] for further details behind all relations presented in this section.

2.2.7. An Example Python Script

The following python script was used to simulate a typical flat field for the setup described in section 2.3. It first creates every necessary setup component, then connects them with the corresponding propagator and finally calls `source.calculate_results()`. This starts the calculation and stores the resulting detector intensity images in the file with the name passed to the detector. The required grid size and grid spacing were calculated manually (cf. section 2.2.6).

Listing 2.1: Example python simulation script calculating the results of a flat-field scan.

```
1  # -*- coding: utf-8 -*-
2  """
3  flat_field.py
4
5  Dark field simulation script.
6
7  This script calculates the flat field (reference result
8  without sample).
9
10 @author: Andreas Malecki
11
12 """
```

```
13
14  import time
15  from pyXSFW.material import Material
16  from pyXSFW.propagation import (AngularSpectrumPropagator,
17                                  DummyPropagator)
18  from pyXSFW.components import (PlanewaveSource,
19                                 RectangularGrating,
20                                 GratingStepper,
21                                 PilatusLikeDetector,
22                                 DetectorController,
23                                 GaussianSmoother)
24
25  start = time.time()
26
27  source = PlanewaveSource(name='Source',
28                           position=(0, 0, -1.0),
29                           energy=45.7e3, N=(4096, 4096),
30                           delta=5e-6/20)
31
32  G1 = RectangularGrating(name='G1',
33                    position=(0, 0, 0), period=5e-6,
34                    dutycycle=0.5,
35                    material_substrate=Material('Si', 2.336),
36                    material_lines=Material('Ni', 8.908),
37                    material_spaces=Material(),
38                    height_substrate=500e-6,
39                    height_lines=8e-6,
40                    height_spaces=0e-6)
41
42  smoother = GaussianSmoother(name='Smoother',
43                              position=(0., 0., 0.46075),
44                              sigma_x=1e-6,
45                              sigma_y=1e-6)
46
47  G2 = RectangularGrating(name='G2',
48                    position=(2.5e-6, 0., 0.46075),
49                    period=5e-6, dutycycle=0.5,
50                    material_substrate=Material('Si', 2.336),
51                    material_lines=Material('Au', 19.32),
52                    material_spaces=Material(),
53                    height_substrate=500e-6,
54                    height_lines=150e-6,
```

```
                  height_spaces=0e-6)

stepper = GratingStepper(name='Stepper',
                         grating=G2, steps=8,
                         distance=(G2.get_period(), 0))

detector = PilatusLikeDetector(name='Detector',
                     filename='results/flat_field.h5',
                     position=(0, 0, 0.46075),
                     pixelsize=(250e-6, 250e-6),
                     sensor_material=Material('Si', 2.336),
                     sensor_thickness=450e-6)

controller = DetectorController('Controller',
                                detector=detector)

source.add_propagator(AngularSpectrumPropagator(to=G1))
G1.add_propagator(AngularSpectrumPropagator(to=smoother))
smoother.add_propagator(DummyPropagator(to=stepper))
stepper.add_propagator(DummyPropagator(to=controller))

source.calculate_results()

end = time.time()
print 'The complete simulation took %f s.' % (end-start)
```

In this script a `GaussianSmoother` object is used, which will be explained in section 2.3.1.

2.3 Validation of the Simulation Framework

The aim behind the simulation study presented in this section was to correctly account for the underlying physical interactions that give rise to the image formation process, and quantitatively predict the outcome of dark-field imaging experiments on various samples. This study was carried out together with Guillaume Potdevin and Franz Pfeiffer. It focused on the analysis of the complementarity of the conventional transmission and dark-field imaging signal of samples containing an ensemble of scatterers modeled by sub-pixel diameter

spheres. In several different sets of simulation runs, we varied their diameter, material, and number and examine the resulting transmission and dark-field signals.

The basis for comparing the results to existing work was the ground-breaking publication by Wataru Yashiro et al. [27]. In their work, they present a theoretical model for the dark-field signal gained from grating interferometry by splitting up the phase shift introduced by the specimen in both a fast and a slowly varying part with respect to the spatial frequency transversal to the propagation direction ($\Delta\Phi_\mathrm{f}$, $\Delta\Phi_\mathrm{s}$). The slowly varying part gives rise to the phase-contrast signal, whereas the dark-field signal is attributed to the fast varying part. In addition to that, they modeled the scattering processes by a Gaussian model with standard deviation of the scattering angles σ. With these assumptions they derived an expression for the dark-field signal D at position (x, y) for a phase grating with $\pi/2$ phase shift:

$$D = \frac{V^\mathrm{s}}{V^\mathrm{r}} \approx \overline{\exp[i\Delta\Phi_\mathrm{f}(x, y; \alpha p_2)]} \approx \exp[-\sigma^2(x, y)\{1 - \gamma(x, y; -\alpha p_2)\}]. \tag{2.54}$$

As in section 1.2, p_2 denotes the period of the analyzer grating. α is the relative Talbot order, which in this publication corresponds to the Talbot distance $z_T = \alpha p_1^2/\lambda$. γ denotes the normalized autocorrelation function defined by

$$\gamma(x, y; \Delta x) = \frac{\overline{\Phi_\mathrm{f}(x, y)\Phi_\mathrm{f}(x + \Delta x, y)}}{\sigma^2}. \tag{2.55}$$

Susanna K. Lynch et al. [32] explicitly calculated the autocorrelation function for a sample containing a large number of spheres and arrived at the following expression:

$$D(x, y) = \frac{V^\mathrm{s}}{V^\mathrm{r}} = \exp\left(-\int \mu_\mathrm{d}(x, y, z)\,\mathrm{d}z\right), \tag{2.56}$$

$$\mu_\mathrm{d} = \frac{3\pi^2}{\lambda^2} f\,|\Delta\chi|^2\, d_0 \begin{cases} D' - \sqrt{D'^2 - 1}(1 + D'^{-2}/2) + \\ \qquad (D'^{-1} - D'^{-3}/4) \\ \qquad \ln[(D' + \sqrt{D'^2 - 1})/ \\ (D' - \sqrt{D'^2 - 1})], \text{ for } d_s > d_0; \\ \\ \qquad D', \text{ for } d_s \leq d_0. \end{cases} \tag{2.57}$$

Here, μ_d is the visibility extinction coefficient (scattering coefficient), a scalar value representing the scattering power of the sample at a certain position. Equation (2.56) had been found previously in experiment by Bech et al. [29]. For a sample consisting of homogeneous spheres, μ_d is a constant and can be calculated analytically. In (2.57), f denotes the volume fraction occupied by the

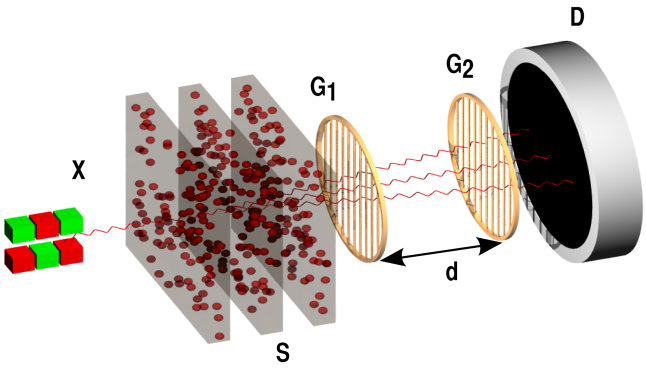

Fig. 2.3: Experimental setup simulated to characterize the dependence of the x-ray dark-field signal on the scattering properties of the sample. It consisted of an x-ray source X, a sample S, the Talbot interferometer formed by the phase grating G_1 and the analyzer grating G_2, and the detector D. The sample was designed to contain one or more slices of an ensemble of randomly distributed sub-pixel scatterers (spheres).

spheres and $\Delta\chi$ is the difference in complex refractive index between the sphere material and the surrounding medium. $d_0 = \frac{\lambda}{p_2}L$, where L is the distance between sample and analyzer grating, and

$$D' = d_s/d_0 \tag{2.58}$$

is the ratio between the sphere diameter d_s and d_0.

Both the theoretical results of Yashiro et al. and Lynch et al. were verified experimentally in the named publications. Consequently, by validating the simulation results against these predictions, the correctness of the simulation can be proven.

2.3.1. Simulation Details

The simulated x-ray grating interferometry setup considered particularly in this chapter, is shown in fig. 2.3. X-rays are emitted by a monochromatic x-ray source in coherent plane waves at the energy $E_{ph} = 45.7\,\text{keV}$, corresponding to a wavelength $\lambda = 0.271\,\text{Å}$. The different samples are located between the source and the first grating G_1. This grating is made of $8.0\,\mu\text{m}$ high Nickel lines on a $500\,\mu\text{m}$ thick silicon substrate introducing a phase difference between its lines and spaces of $\pi/2$ to the incoming beam at the given energy. The grating period p_1 is $5.0\,\mu\text{m}$ and the duty cycle 0.5 (Ronchi ruling). The second grating G_2 is located exactly at the first fractional Talbot distance $d = p_1^2/2\lambda = 46.1\,\text{cm}$ behind

G_1. The interference pattern in this case has the same period as the phase grating G_1. The period of G_2 is $p_2 = p_1 = 5.0\,\mu m$. The grating lines of G_2 are made of 150 µm of gold on a silicon substrate of 500 µm thickness. A pixelated photon counting detector is placed right behind G_2. Its pixels are $D_x \times D_y = 250\,\mu m \times 250\,\mu m$ large. To retrieve the three different contrast signals, the last grating (G_2) is moved perpendicular to the beam over one grating period in 8 steps (phase stepping) [25].

The initial wavefront amplitude at the source position was constant and normalized to an integral intensity of 1 over the simulated area, thus, resembling a plane wave (`PlanewaveSource`). The grid spacing was chosen to be $\Delta = p_1/20 = p_2/20 = 0.25\,\mu m$. This allowed sampling the finest structures in the simulation well below the Nyquist frequency. With this grid spacing, aliasing effects could be reduced to a minimum, too. All setup components and propagation steps were sampled at this resolution. The gratings were represented by instances of `RectangularGrating`. The detector class, which was used for this study, was the `PilatusLikeDetector`. With the number of grid points of 4096 x 4096 the simulation covered approximately 5 x 5 detector pixels. Only the center pixel was used for further evaluation to avoid possible border effects originating in the wavefront propagation or caused by the sample boundaries. Propagation from one setup component to the next was done with the `AngularSpectrumPropagator`.

To account for a finite focal spot size of the source and grating imperfections, the intensity pattern was convoluted using a two-dimensional isotropic Gaussian filter kernel with a standard deviation of $\sigma = 1\,\mu m$ before applying the second grating. This is done by the `GaussianSmoother` class from the simulation framework. As in a real experiment, the second grating G_2 was scanned over one grating period (`GratingStepper`). For each scanning position a detector image was taken.

All samples were subdivided into one or more slices consisting of spheres randomly distributed over an area of $500 \times 500\ \mu m^2$ (several instances of `FlatSpheresSample`). The slices were positioned in the center of the simulated area and, thus, covered the central detector pixel and half or a quarter of its direct neighbors. The number of spheres N_S per slice as well as the sphere diameter d_S were chosen according to the examined properties of interest. d_S was chosen (deliberately) between the grating periods and the detector pixel size: $p_1 \lesssim d_S < 250\,\mu m$.

2.3.2. The Influence of the Sample Morphology on the X-Ray Dark-Field Signal

The computed transmission and dark-field signal were examined regarding their dependence on the sample thickness, the diameter of the sample's substructures, the number of spheres inside the sample, and the material density. Furthermore, it was checked whether the use of the projection approximation was valid as well as how the signal behaves for samples containing mixed structure sizes as opposed to the parts containing only one size of substructures.

Dark-Field Contrast and Sample Thickness

A first set of simulations was performed to analyze the transmission and the dark-field signal with respect to the sample thickness (results shown in fig. 2.4). For this purpose the sample was separated into 9 layers containing a fixed number N_S of calcium spheres per layer with a diameter of 50 µm each and a density $\rho = 1.55\,\mathrm{g/cm^3}$. The simulation was run for 3 different numbers of spheres $N_S \in \{250, 500, 1000\}$ and $N_L \in \{1, \ldots, 9\}$ layers. For each thickness 10 simulations differing only in the random positions of the spheres were carried out, which allowed to calculate a statistical mean and to estimate the possible errors caused by the finite number of spheres inside the sample (see fig. 2.4). The relation for both contrast mechanisms was found to be exponential with stronger signal for increasing sample thickness. The transmission is much less affected by the increasing thickness because of the low absorption of calcium at 45.7 keV compared to the scattering caused by the numerous spheres resulting in a strong dark-field signal.

The intensity reduction of x-rays passing through matter follows the Beer-Lambert law:

$$T(x,y) = \exp\left(-\int \mu(x,y,z)\,\mathrm{d}z\right). \tag{2.59}$$

Here, the x-rays travel along the z direction. This relation stays valid for the transmission signal calculated from the stepping procedure [21]. For the given kind of sample the transmission measured by one detector pixel can be approximated by:

$$T \approx \exp\left(-\mu\langle\Delta z\rangle\right) = \exp\left(-\mu\frac{N_S\pi}{6A_S}d_S^3\right). \tag{2.60}$$

A derivation of this equation is given in appendix A. Here, μ is the absorption coefficient of the sphere material, $\langle\Delta z\rangle$ the thickness of penetrated material

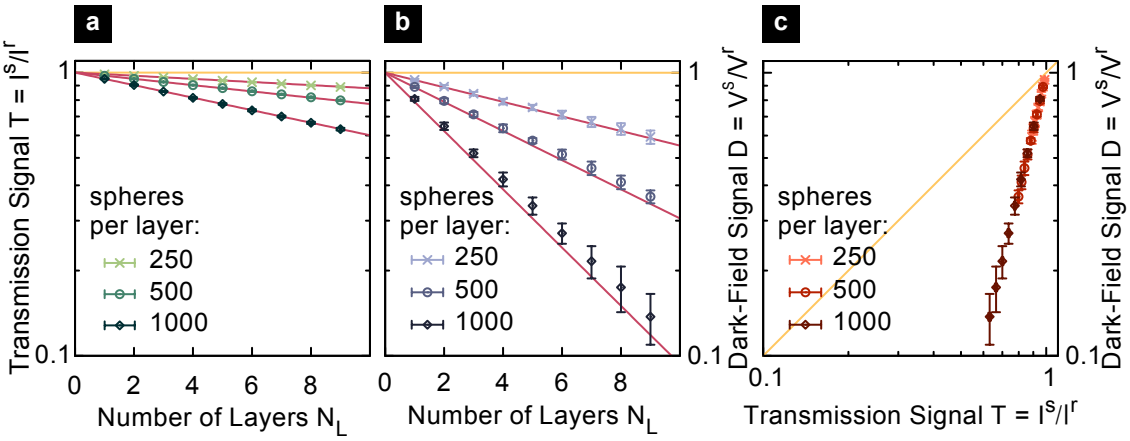

Fig. 2.4: Dependence of a sample's dark-field signal on the sample's thickness. a)+b) Semi-logarithmic plots of the simulated transmission and the dark-field signal ($T = I^{\mathrm{s}}/I^{\mathrm{r}}$ and $D = V^{\mathrm{s}}/V^{\mathrm{r}}$) with respect to the number of scattering sample layers $N_L \in \{1,\ldots,9\}$. The sample consisted of an increasing number of slices each containing a fixed number of calcium spheres $N_S \in \{250, 500, 1000\}$ at randomly distributed positions with a diameter of 50 µm and a density $\rho = 1.55\,\mathrm{g/cm^3}$. The shown statistical mean and errors were calculated by evaluating 10 different sets of slices. The theoretical curves are shown in solid red lines. c) A two-dimensional histogram plot showing the correlation of the dark-field signal with the transmission signal for each sample thickness N_L and number of spheres N_S.

averaged over one detector pixel, and A_S denotes the area covered by the sample ($500 \times 500\,\mu\mathrm{m}^2$). This approximation is valid only for samples whose mean thickness does not vary too much over one detector pixel area. The theoretical curves calculated from eq. (2.60) are shown in fig. 2.4a). They agree very well with the simulation results.

The dark-field signal as well obeys a similar exponential law found in the aforementioned theoretical and experimental works [27, 29, 32]. For the parameters used in this study, the expression for the line integral in equation (2.57) can be simplified to

$$\begin{aligned}\int \mu_{\mathrm{d}}\,dz &= \mu_{\mathrm{d}}\Delta z \\ &= \frac{L\pi\lambda^3 N_S d_S^3}{8p_2 A_S}\left[(r_0 Z\rho/m_{\mathrm{A}})^2+\mu^2\right] \\ &\quad\Big(D' - \sqrt{D'^2-1}(1+D'^{-2}/2) \\ &\quad +(D'^{-1}-D'^{-3}/4) \\ &\quad \times \ln[(D'+\sqrt{D'^2-1})/(D'-\sqrt{D'^2-1})]\Big)\,.\end{aligned} \tag{2.61}$$

Here, L is the distance from the sample to the detector, Z, ρ, m_{A}, μ are

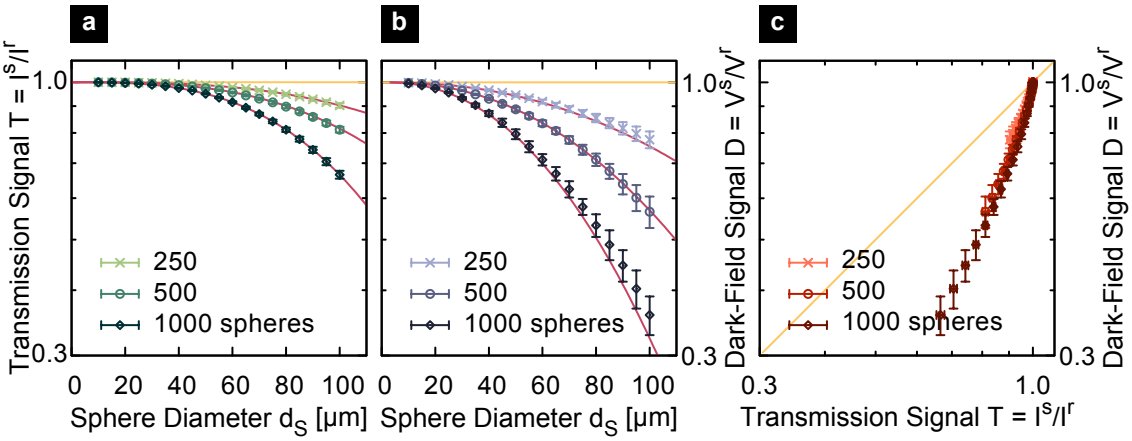

Fig. 2.5: Dependence of a sample's dark-field signal on the structure size inside the sample when the number of structures is kept constant. a)+b) Simulation results for the dependence of the transmission and the dark-field contrast ($T = I^s/I^r$ and $D = V^s/V^r$) on the diameter of the spheres inside the sample d_S for 3 different sphere numbers $N_S \in \{250, 500, 1000\}$. The spheres were made of calcium with a density of $\rho = 1.55\,\mathrm{g/cm^3}$ and their diameters d_S were varied in 5 µm steps from 10 µm up to 100 µm. c) Comparison of the two signals in a two-dimensional histogram correlating the dark-field signal to the transmission signal for each sphere diameter d_S and number of spheres N_S.

the material properties, and $D' = d_S p_2/\lambda L$. The calculated theoretical curves for the dark-field signal also agree well with the simulation results (cf. fig. 2.4b)).

For rather homogeneous samples – as assumed in the simulated setup – the exponents of the Beer-Lambert law and its dark-field equivalent only differ by a constant factor, as can be seen from the two-dimensional histogram in fig. 2.4c), which highlights the high level of correlation between the two signals. The dark-field signal mostly depends on the position of the sphere borders, where the x-rays are refracted most, while the transmission relates to the average material thickness lying in front of the detector pixel. Consequently, the statistical deviations in the dark-field signal are larger than those for the transmission.

Dark-Field Contrast and Structure Size at Constant Number of Structures

Furthermore, we investigated the behavior of the two signals as a function of the sphere diameter d_S, while keeping the number of spheres inside the sample (N_S) constant. Hence the total volume occupied by the sample material changed

as well. Now the sample consisted of one single slice filled with 250, 500, or 1000 calcium spheres, respectively. Their diameters were varied in 5 µm steps from 10 µm up to 100 µm (see fig. 2.5) and their density was $\rho = 1.55\,\mathrm{g/cm^3}$. We observe that both signals become stronger with growing sphere diameter. The small absorption power of calcium at 45.7 keV causes rather weak losses in the transmission signal. Again, the dark field is affected much stronger because of the scattering at the large number of substructures inside the sample.

The transmission and the dark field, again, follow the expected curves given in eq. (2.60) and eqs. (2.56) and (2.61), respectively. In fig. 2.5a) the red solid lines belong to the $\exp(x^3)$-law and fit agreeably to the simulated data. In contrast to the previous case, the dark-field signal deviates significantly from the transmission as it roughly follows an $\exp(x^4)$-law (cf. fig. 2.5b)+c)). For larger sphere diameters the transmission is expected to dominate more and more as the particles reach the detector pixel size.

Dark-Field Contrast and Structure Size at Constant Amount of Material

A third set of simulation runs provided data for the relationship between the transmission or dark-field signal and the number of scattering spheres in the beam while the volume fraction occupied by the spheres was kept constant. The scatterers were located in a single sample slice and made of three different materials, Carbon (C), Silicon (Si), and Calcium (Ca) with densities $\rho = 2.2\,\mathrm{g/cm^3}$, $2.336\,\mathrm{g/cm^3}$, and $1.55\,\mathrm{g/cm^3}$, respectively. As in the last section, the sphere diameter was varied in 5 µm steps from 10 µm up to 100 µm. To examine the interferometer's region of maximum sensitivity in detail we added a refined set of data points in the range from 3 µm up to 10 µm in steps of 0.5 µm. The number of spheres inside the sample then followed from the constant integrated sphere volume $V_{\mathrm{total}} = 0.0655\,\mathrm{mm^3}$. This value results for 1000 spheres with a diameter of 50 µm.

While the transmission for a certain total volume is constant for a certain material, the dark-field signal becomes stronger with an increasing number of scattering structures inside the sample, which is equivalent to a decrease in diameter (see fig. 2.6a)+b)). The dark-field signal is stronger for the two materials with smaller atomic number, carbon and silicon, and weaker for calcium.

From eq. (2.60) and the constant average thickness of the penetrated material

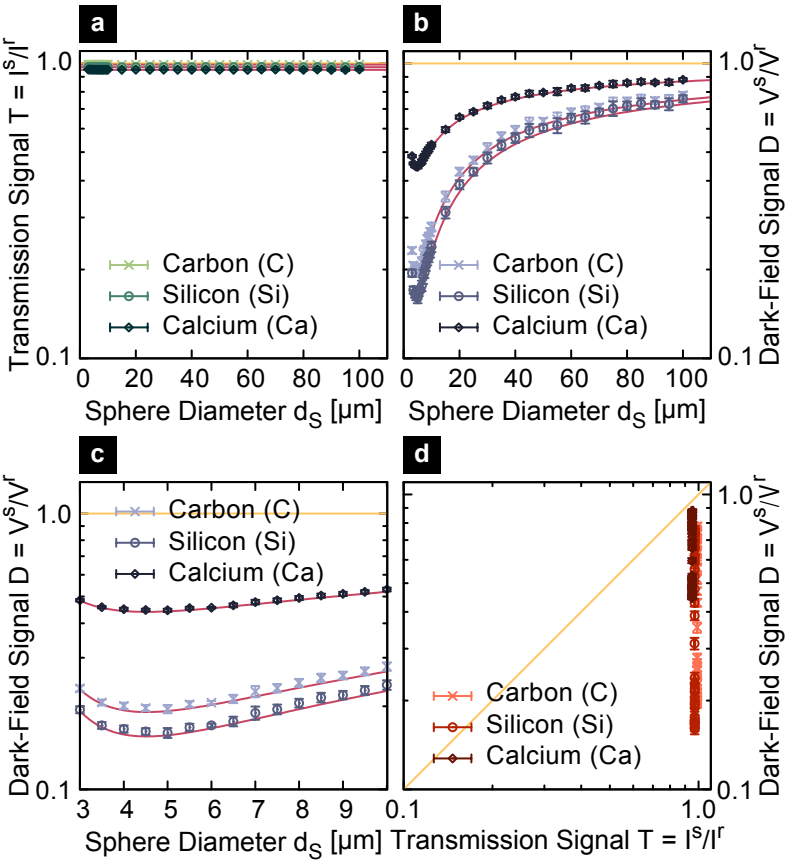

Fig. 2.6: Dependence of a sample's dark-field signal on the structure size inside the sample when the amount of material is kept constant. a)-c): Dependence of the transmission and the dark-field signal ($T = I^s/I^r$ and $D = V^s/V^r$) on the number of structures inside the sample. The total volume occupied by all equally sized spheres was kept at the constant value $V_{\text{total}} = 0.0655\,\text{mm}^3$. From left to right the sphere diameter increases from 3 µm up to 10 µm in steps of 0.5 µm and from 10 µm up to 100 µm in steps of 5 µm. The number of spheres changes accordingly. To visualize the details in the region of maximum sensitivity c) shows a magnification of the results below 10 µm. d): Two-dimensional histogram correlation of the two signals.

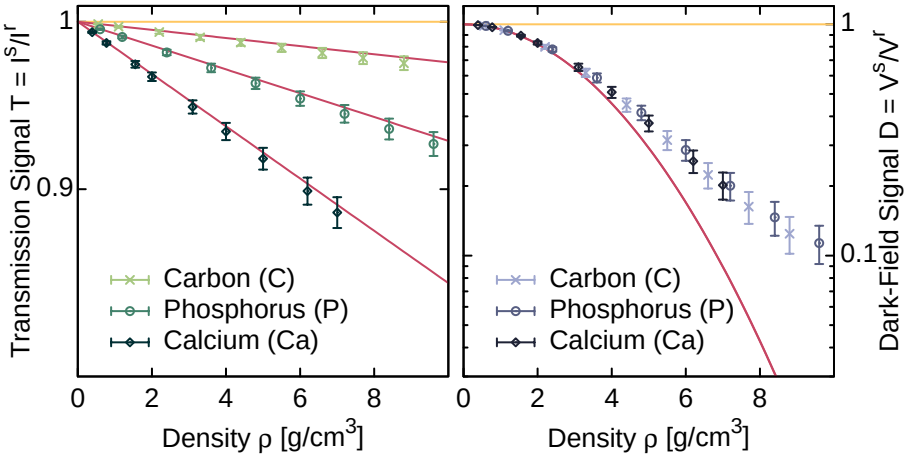

Fig. 2.7: Dependence of a sample's dark-field signal on the material density. The sample contained a total of 500 spheres with a diameter of 50 µm each. The spheres consisted of carbon (C), phosphorus (P), and calcium (Ca), respectively. Left: The transmission decreases exponentially with increasing density. The simulated values coincide with the theoretical predictions given by the red lines. Right: The exponent of the dark-field signal law contains a quadratic dependence on the density. The theoretical curves (red) agree with the simulation results only for small density values. Above a density of approximately $4\,\mathrm{g/cm^3}$, the simulated dark-field signal is much weaker than theoretically expected.

there follows that the transmission signal stays constant for a constant volume occupied by the carbon spheres. In contrast to that, the dark-field signal becomes stronger for more numerous and smaller scattering structures. Here, the increasing number more or less clearly outweighs the changes in sphere diameter. This way, it becomes possible to discriminate between a perfectly homogeneous solid material with low absorption and a material containing denser substructures. From eqs. (2.56) and (2.61), we can deduce that for a constant volume occupied by the scattering spheres, the dark-field signal only depends on D'. The simulation results agree with the theoretical prediction also in this scenario. Moreover, they clearly show the theoretically expected maximum at structure sizes around 4.5 µm (see fig. 2.6c)). In this setup the main potential of the dark-field signal becomes clearly visible. It visualizes the number of scattering substructures in the sample without requiring a high detector resolution.

Dark-Field Contrast and Material Density

In addition to the thickness and the number of spheres, I also performed simulations which varied the density ρ of the sphere material. The spheres consisted

of carbon (C), phosphorus (P), or calcium (Ca), respectively. The material density was varied between $0.55\,\mathrm{g/cm^3}$ and $9.6\,\mathrm{g/cm^3}$, while the number of spheres was kept constant at 500. Each sphere had a diameter of $50\,\mu\mathrm{m}$. For each density and material, 10 simulation runs were performed with different random positions of the spheres. Fig. 2.7 shows the results for transmission and dark-field signal together with the theoretically expected curves (red). The transmission increases exponentially with increasing density, whereas the dark-field signal shows a different behavior. It first increases stronger and stronger until $\rho \approx 5\,\mathrm{g/cm^3}$. For larger densities, the increase in dark-field signal diminishes again.

From equations (2.60) and (2.43), one would expect exactly the behavior seen for the transmission signal. The exponent of the dark-field signal, however, should depend on the density quadratically (cf. eq. (2.57)). For small densities, theory and simulation agree within the statistical error. For densities larger then approximately $4\,\mathrm{g/cm^3}$, the dark-field signal deviates significantly from the theoretical expectations. One possible reason for this error may be a too low simulation resolution. Regarding the complex transmission function of a single sphere, the phase of the output wave changes strongly at the sphere's borders. For very dense materials, the simulation resolution has to be fine enough to adequately sample these borders. Let us examine two simulated pixels inside the sphere. The first one shall be directly at the border but still inside the sphere. The second one shall be its neighbor towards the sphere center. At the given photon energy of 45.7 keV, a grid spacing of $0.25\,\mu\mathrm{m}$, and a material made of phosphorus with a density of $7\,\mathrm{g/cm^3}$, the change in phase between these two simulation pixels is roughly 25°. Consequently, for such a strongly refracting material, the grid spacing is too large. As most of the signal originates in this area, this explains the large deviations between theory and simulation.

Projection Approximation and Inhomogeneous Samples

All sample slices used in the simulation were treated in projection approximation. This ignores possible multiple interaction of x-rays with the sample matter. To show that this can safely be neglected for the chosen setup parameters another simulation was done for a sample consisting of two parts moved apart along the beam direction. Each part contained 1000 carbon spheres with a diameter of $50\,\mu\mathrm{m}$ and a density $\rho = 2.2\,\mathrm{g/cm^3}$. If the interaction inside the sample played a role the resulting dark-field signal should depend on the distance between both sample parts. The distance between the two sample slices was increased from 0 mm to 200 mm in steps of 10 mm and the resulting trans-

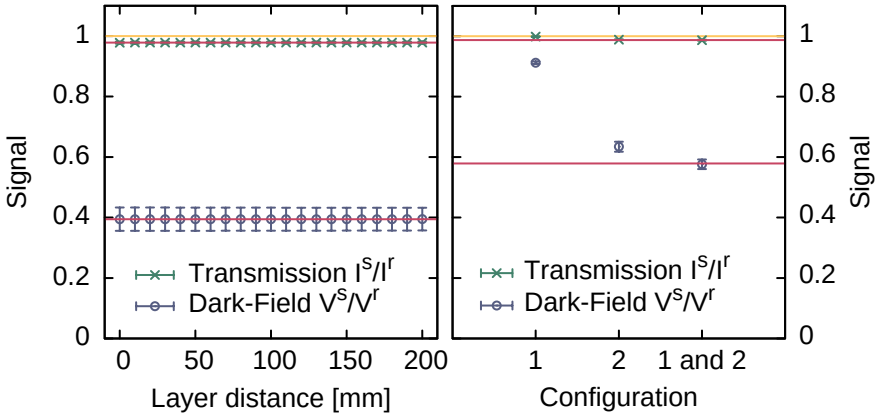

Fig. 2.8: Validation of projection approximation in the simulation and cross-check for a simulated sample containing different structure sizes. Left: Transmission and dark-field contrast for samples consisting of two parts. The distance between these two parts was varied. Right: Simulation results for two different structure sizes inside the sample. Configuration 1: 25 µm. Configuration 2: 50 µm. Configuration 3: Both sizes combined in two slabs one after the other.

mission and dark-field signal calculated (see fig. 2.8 on the left). Transmission and dark-field signal both are constant and, consequently, prove the validity of using the projection approximation[3]. A comparison of these findings to the theoretical predictions shows that for the given setup the dark-field coefficient is almost independent of the sample to detector distance, which cancels out in eq. (2.61).

To ensure that all the above results also hold for mixed structure sizes, another sample configuration was tested as well. Here, the sample consisted of two slices a distance of 10 mm one after the other containing 1000 carbon spheres each. The spheres in the first slice had a diameter of 25 µm while those in the second slice were 50 µm large. A simulation run was done for samples consisting of only one of the two slices and for both of them (see fig. 2.8 on the right). The combined sample exactly causes the same drop in transmission and dark field as the product of both its parts. In consequence, relations (2.59) and especially (2.56) and (2.61) stay true for mixed structure sizes.

[3]For a cone-beam geometry this would not hold unless the sample is sufficiently small.

2.4 Conclusion

The wave-optical numerical simulation framework `pyXSFW`, which was presented in detail in this chapter with respect to the underlying theory and numerical approaches, quantitatively models the dark-field signal formation in a grating interferometry imaging setup. This could be shown for a specimen consisting of an ensemble of sub-pixel sized spheres. The dark-field signal simulations showed which additional complementary information about the sample can be obtained when compared to the transmission signal. For samples containing substructures of sub-pixel size the dark-field signal is more sensitive to the thickness of the sample. It also depends on the size of the substructures and strongly discriminates between samples containing the same amount of material distributed, on the one hand, over a few large particles and, on the other hand, over many smaller ones while the transmission is not influenced at all. The simulation results prove as well that the origin of the dark-field signal can be found in refraction at structures with sizes below the detector pixel pitch. The lower bound to structures giving a strong signal is one order of magnitude below the period of the interference pattern, which can be inferred from fig. 2.6. Moreover, it was shown that the projection approximation is valid for the given setup parameters and that mixed structure sizes do not affect the validity of the results. All results agree well with theoretical and experimental work done previously showing their validity and accuracy. The only deviations found for very dense materials could be explained by a too coarse simulation grid. On top of that the simulation approach allows to examine arbitrary samples that may not be described analytically.

The next chapter will present an investigation of an extension method to simple x-ray dark-field imaging: Directional Dark-Field Imaging. This study was also substantially based on simulation results gained from `pyXSFW`.

3 Superposition in Directional Dark-Field Imaging

If I'm sitting next to a swimming pool, and somebody dives in - and she's not too pretty, so I can think of something else - I think of the waves and things that have formed in the water. And, uh, when there's lots of people have dived in the pool there's a very great choppiness of all these waves all over the water and to think that it's possible, maybe, that in those waves there's a clue as to what's happening in the pool.

Richard Feynman

Dark-field contrast obtained from x-ray grating interferometry does not only offer to perform radiography and tomography. It also provides another experimental method to retrieve information about the sub-pixel structure orientation and anisotropy called Directional Dark-Field Imaging (DDFI) or X-Ray Vector Radiography (XVR). As described in section 1.3, the dark-field contrast signal D is extracted from the visibility of the interference pattern created by the grating interferometer. The more the interference pattern is distorted and its visibility decreases, the stronger is the measured dark-field signal. One result of chapter 2 was that scattering in the sense of x-ray dark-field imaging can be regarded as refraction at small structures. Since the interferometer is built from two-dimensional plane gratings made of one-dimensional lines and spaces, it is only sensitive to distortions that occur perpendicular to these lines. This direction-dependence is utilized in Directional Dark-Field Imaging. Here, the dark-field signal is examined for different orientations of the sample relative to the interferometer lines. By rotating the sample and recording the dark-field signal $D(\theta)$ with respect to its orientation θ, it allows to draw conclusions on the anisotropy of the sub-pixel size structures as it will be described further below.

For thin specimens, the x-ray beam passes only through a few structures located one behind the other. Here, the scattering signal recorded by each detector pixel is produced by at most one single sample feature. Because of that, almost all structures that contribute to the dark-field signal in each single detector pixel can be assumed to be parallel and it is easy to deduce their direction and anisotropy from the orientations producing the maximum signal. Jensen et al. showed this for several different specimens: A strawberry leaf, a chicken wing, a fiber mesh and a tooth slice [56, 57, 64]. For weakly scattering samples they found that the dark-field signal D in detector pixel (j,k) with respect to the angle of rotation θ can be approximated by a Fourier expansion up to the first order [64]:

$$\begin{aligned} D(j,k,\theta) &= \sum_{n=0}^{\infty} b_n(j,k)\cos[2n(\theta-\tau_n(j,k))+\pi], \\ &\approx b_0(j,k)+b_1(j,k)\cos[2(\theta-\tau_1(j,k))+\pi]. \end{aligned} \tag{3.1}$$

They interpreted b_0 as the local average scattering power, b_1 as the scattering asymmetry, and τ the preferred scattering direction. For strongly ordered systems, where the amount of scattering can reduce the visibility of the interference pattern below the noise level, they proposed a different model:

$$D(j,k,\theta) = (1-\alpha)+\alpha\exp\left[\frac{-2\pi^2\sigma^2}{p_2^2}\right]. \tag{3.2}$$

In this Gaussian model, α denotes the amount of photons scattered by the sample, σ is the standard deviation of the scattering directions with respect to the angle, and p_2 is the analyzer grating period. The simulation results discussed in section 3.2 show that the assumption of a Gaussian profile does not hold and that the Fourier expansion should be performed on $-\log D$ instead of D.

In [28], we performed XVR on several thin vertebral bone slices and showed that the resulting signal can be explained by each sample's structural arrangement.[4] However, for thick samples the connection between the recorded directional dark-field signal and the morphology is not self-evident. Here, several differently oriented layers of substructures can lie behind each other, each layer producing its own direction-dependent signal. Knowing the physics behind the signal formation is a fundamental prerequisite for potential future medical diagnostic and materials science applications. Moreover the direction-dependent

[4] These early works like those by Jensen et al. assumed the dark-field signal itself to be cosine-shaped instead of its logarithm.

computed tomography method described in chapter 4 is based on this knowledge.

In this chapter, the x-ray directional dark-field signal of the superposition of arbitrarily oriented structure layers is related to the signal created by each component alone. In contrast to the experimental work by Revol et al. [65] – which was published independently and parallel to mine – this study is theoretically based on numerical simulations carried out with the simulation framework presented in chapter 2. The predictions from the simulations give rise to a theoretical model describing the superposition principle, which additionally can be related to setup parameters. The model then is validated qualitatively and quantitatively with experimental data of samples containing a large number of highly oriented sub-pixel size structures. Instead of spheres, like in the previous chapter, these were cylinders. I published most parts of this chapter's contents in PLoS ONE together with Guillaume Potdevin, Thomas Biernath, Elena Eggl, Eduardo Grande Garcia, Thomas Baum, Peter B. Noël, Jan S. Bauer, and Franz Pfeiffer [66].

3.1 The Simulation Procedure

Let us first focus on the theoretical predictions for the superposition of directional dark-field signals that can be drawn from simulations. For that purpose, we simulated a complete but simplified x-ray grating interferometry setup for Directional Dark-Field Imaging using `pyXSFW` (see fig. 3.1). It consisted of a monochromatic x-ray source (X) emitting plane waves, two sample layers (L_1 and L_2), the grating interferometer (G_1 and G_2) and a detector D. The source was represented by a `PlaneWaveSource` object with a photon energy of $E_{\mathrm{ph}} = 45.7\,\mathrm{keV}$. From this point on, angular spectrum propagation was used to connect the different setup components. The wavefront was discretized at 8192×8192 grid points that were $\delta = 0.125\,\mu\mathrm{m}$ apart.

The two gratings G_1 (phase grating) and G_2 (analyzer grating) had a period of $5.0\,\mu\mathrm{m}$ and a duty cycle of 0.5 (`RectangularGrating`). The height of the phase grating lines was $8.0\,\mu\mathrm{m}$, which is equivalent to a phase shift of $\pi/2$ at the chosen photon energy. The analyzer grating was located 46.1 cm behind G_1, which corresponds to the first fractional Talbot distance at this energy. Its lines were made of $150\,\mu\mathrm{m}$ of gold to ensure high absorption and interference pattern visibility. The grating lines were oriented along the vertical direction at all times. Right after the last grating followed a pixelated photon counting detector with

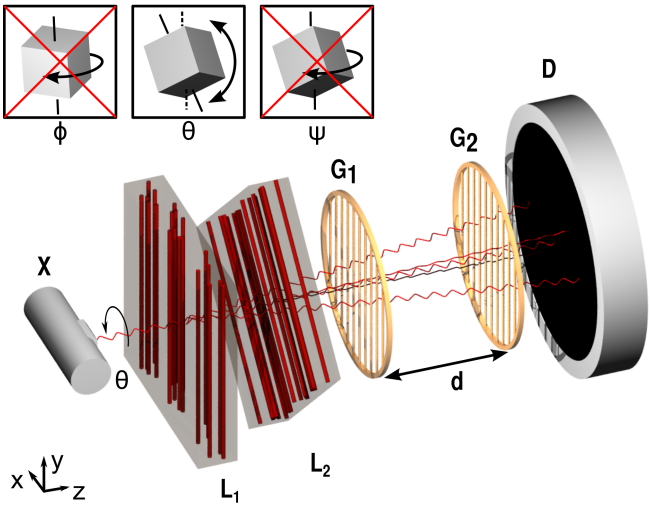

Fig. 3.1: Schematics of the x-ray grating interferometry setup used to study the superposition principle in Directional Dark-Field Imaging. The simulated setup consisted of an x-ray source , two layers of highly oriented structures (cylinders, L_1 and L_2), the grating interferometer (G_1 and G_2), and a detector (D). For the experiment, an additional grating (G_0) was used right behind the source to enforce the coherence conditions required by the interferometer. The sample layers were rotated independently from each other around the optical axis to retrieve the direction-dependence of the dark-field signal.

a pixel size of $D_x \times D_y = 250\,\mu\text{m} \times 250\,\mu\text{m}$ (`PilatusLikeDetector`). The finite focal spot size was taken into account by smoothing the intensity of the wavefront right behind the analyzer grating with a Gaussian filter kernel of width 1 µm (`GaussianSmoother`).

Here, we considered a sample consisting of 2×250 parallel cylinders all lying in two separate planes perpendicular to the beam axis and one plane behind the other. Each cylinder has a well-defined scattering direction perpendicular to the cylinder axis. In consequence, we expected the signal to be completely anisotropic meaning a strong cosine oscillation with respect to the angle of rotation around the beam axis as it was found previously in experiments [56, 57, 64]. The cylinder positions were randomly distributed over an area of $500\,\mu\text{m} \times 500\,\mu\text{m}$ around the beam axis. Every single cylinder consisted of calcium (density $\rho = 1.55\,\text{g/cm}^3$), was oriented perpendicular to the beam direction, and had a diameter of 50 µm and a height of 1000 µm. Because of the much smaller dimensions of the detector pixels, we avoided border effects of the cylinder endcaps. Two instances of the class `FlatCylindersSample` were used to represent the two separate sample layers. `FlatCylindersSample` is basically identical to `FlatSpheresSample` described in section 2.2.5. Instead of spheres, it computes the transmission function of long parallel cylinders. The two sample layers

(L_1 and L_2) were located 3.0 cm and 2.0 cm in front of the phase grating G_1. Each sample layer was applied to the wavefront separately with an angular spectrum propagation step in between.

At first, each layer was simulated separately to retrieve its independent contribution to the dark-field signal. To get the directional information, we rotated the sample in discrete steps of 22.5° around the beam axis. The angle of rotation θ is measured between the horizontal axis and the cylinder axis. For each sample orientation, a stepping curve was recorded by moving the analyzer grating (G_2) in horizontal direction over one grating period in 8 steps. The simulated area covered roughly 5 x 5 detector pixels, but only the center pixel provided the dark-field data used for this study. Each simulated orientation was repeated 9 times with different random positions of the cylinders. This allowed to estimate the average and spread of the dark-field values. Afterwards, both sample layers were simulated together for certain constant relative angles $\Delta\theta = 0°, 45°, 90°$ in between the two of them. In addition to that, the 45° orientation was simulated with the first layer containing only 125 cylinders corresponding to half the thickness. The listing in appendix B shows the python script used for this study. We calculated the three different contrast signals from the Fourier transform of the resulting intensity variation as it was described in section 1.3.

3.2 Predictions Drawn from the Simulation Results

Each simulated single sample layer on its own produces a dark-field signal which can be described to a good approximation by (see fig. 3.2)

$$D(\theta) = \exp[-A(\cos[2(\theta - \tau)] + 1)]. \tag{3.3}$$

This relation is deduced from the plot of a single layer and visualized by the corresponding fit curve shown in addition to the data points in gray color. The constant parameter τ gives the orientation causing the strongest signal (lowest values of D). A is related to the amount of direction-dependent scattering and depends on the setup parameters as well as the structure dimensions inside the sample. The maximum signal is reached for orientations where the cylinders are oriented parallel to the direction of the interferometer's grating lines. Analogously, when the cylinders are orientated perpendicular to the grating lines the dark-field signal vanishes completely. From the cosine curves, the average

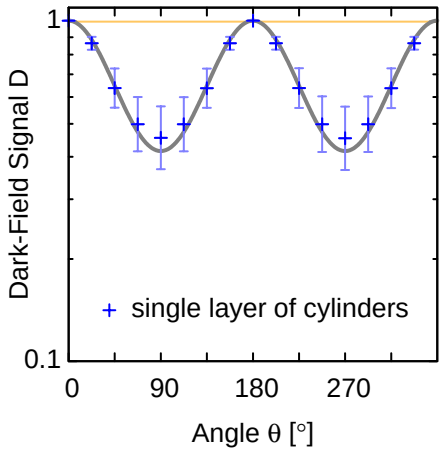

Fig. 3.2: Directional dark-field simulation results for a single strongly oriented sample layer. The sample layer contained 250 cylinders with randomly distributed positions. The logarithmic dark-field signal with respect to the orientation of the cylinders has the shape of a cosine with period π.

logarithmic dark-field signal and the anisotropy with respect to the angle of rotation can be calculated. The average signal is equal to the constant offset of the cosine curves. Since the cylinders are perfectly anisotropic, the offset matches the amplitude A in equation (3.3). The anisotropy is calculated from the amplitude of the oscillation relative to this offset. Consequently, for a completely anisotropic signal the amplitude of the cosine is equal to its offset. Therefore, the anisotropy calculated from the dark-field signal takes values between 1 (perfectly anisotropic) and 0 (isotropic). With respect to these calculations, we deviated from the earlier descriptions by Jensen et al. [56] by using the (negative) logarithmic dark-field signal for the calculation of the average dark-field signal and the main orientiation instead of the dark-field signal itself. This was done due to the fact that for large oscillation amplitudes the directional dark-field signal $D(\theta)$ significantly deviates from a cosine. The Gaussian profile proposed for strongly oriented systems by Jensen et al. in [57] is inadequate as well. In this work, the scattering produced by the specimen was strong enough to decrease the visibility below the noise level of the measurement. Therefore, the actual cosine curves are cut off at the noise level and only appear similar to a Gaussian. This is visualized in fig. 3.3. The setup sensitivity with respect to the dark-field signal can be tuned by choosing the distance between the sample and the detector appropriately. This has been studied by Michael Chabior [12] and can be deduced from equation (2.57). Consequently, the dark-field sensitivity can be optimized for Directional Dark-Field Imaging such that a cut-off due to noise can be avoided.

Figure 3.4 visualizes the directional dark-field signal produced by each single

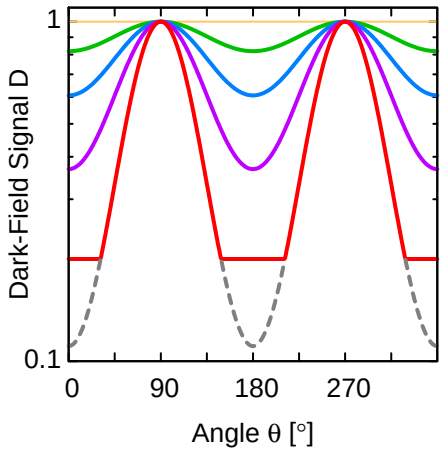

Fig. 3.3: Effect of noise on the angular profile of the directional dark-field signal. For weakly scattering anisotropic samples, the directional dark-field signal is always above the noise level, which in this plot is assumed to be at dark-field values of 0.2. For strongly scattering anisotropic specimens, the dark-field signal can no longer be extracted reliably from the measurement data, when it drops below the noise level. The resulting curve appears like a Gaussian, although it is a truncated cosine.

sample layer and by both layers together for different angles between the two layers. The signal of both layers together shows the same angular dependence as the two single layers but with varying amplitude and phase depending on the relative orientation and the amplitudes of the signal of each single layer. When the orientations of the structures in both layers are chosen to be parallel, the sum signal only changes in amplitude compared to the individual signals. The variance of the superposition signal with respect to the actual microstate of the statistical ensemble of cylinders is quite large. We ascribe this to the high correlation between both layers and the grating lines. For a relative angle of $\Delta\theta = 45^\circ$ between the two layers, the superposition signal has its maximum right in the middle between the maxima produced by the separate layers and it has a slightly larger amplitude. When the structures inside the two layers are oriented perpendicular to each other, the resulting directional dark-field signal is almost constant. The remaining oscillations originate in the randomly distributed locations of the cylinders. Finally, if the first layer contains less scatterers, the phase of the sum signal is less affected by this layer and consequently approaches the phase of the dominating signal produced by layer two.

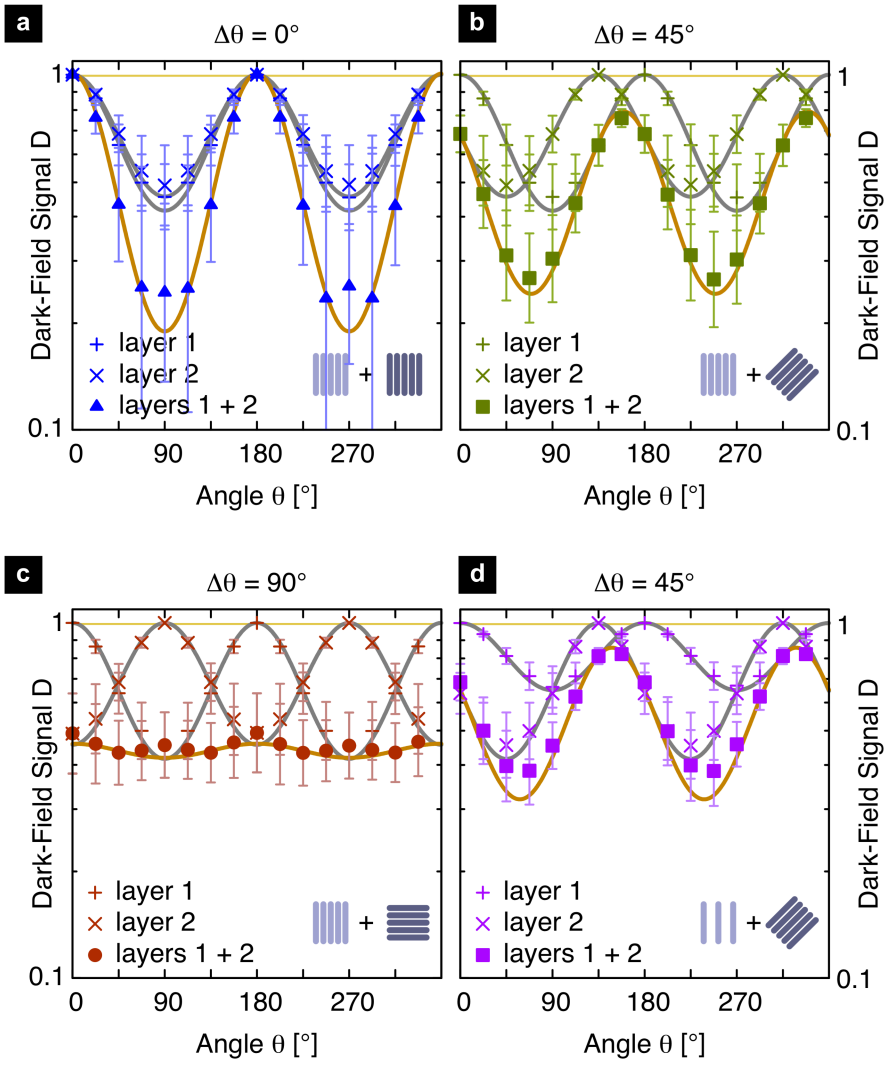

Fig. 3.4: Directional dark-field simulation results for three different relative orientations of two strongly oriented sample layers. a)-c) show the dark-field signal with respect to the orientation of two sample layers containing 250 cylinders each. The cylinders were randomly distributed over a plane perpendicular to the x-ray beam. We examined three different relative orientations between the layers $\Delta\theta = 0°, 45°, 90°$. For each relative orientation, the plots show the dark-field signals of the separate layers and both of them together. Clearly visible is the $\exp(\cos 2\theta)$ dependence for each single layer and the superposition of both of them. For the single layer results, we calculated the corresponding fit curves shown as solid gray lines. The product of both fit functions is shown as a solid orange line. It perfectly agrees with the simulation results for the superposition of both layers. In d) the first sample layer contained only 125 cylinders to simulate a layer of half the thickness. The shape of the signals does not change. From these results, we derived that the superposition signal is simply the product (logarithmic scale) of the two single layers. As a simple consequence, for a relative angle of $\Delta\theta = 90°$, the oscillation almost completely vanishes and the whole sample appears nearly perfectly isotropic.

3.3 A Model for the Superposition Principle

From these findings, we derived a physical model predicting the superposition principle of X-ray Directional Dark-Field Imaging. The directional dark-field signal of each single layer $D_1(\theta)$ and $D_2(\theta)$, respectively, is given by

$$\begin{aligned} D_{1/2}(\theta) &= \exp\left[-A_{1/2}(\cos[2(\theta-\tau_{1/2})]+1)\right] \\ &= \exp\left[-2A_{1/2}\cos^2(\theta-\tau_{1/2})\right]. \end{aligned} \tag{3.4}$$

Here, $\theta - \tau_{1/2}$ is equal to the angle between the direction of scattering of the sample and the direction of maximum sensitivity of the interferometer. A_1 and A_2 are the oscillation amplitudes. The second line in (3.4) follows from the first after applying an addition theorem for the cosine and the Pythagorean trigonometric identity.

Starting from eq. (3.4), we can express the scattering caused by each sample layer with a two-dimensional vector $\boldsymbol{\epsilon}_{1/2} \in \mathbb{R}^2$ with its magnitude corresponding to the scattering strength and its orientation giving the direction of scattering. The interferometer itself is only sensitive to scattering perpendicular to the orientation of the grating lines. This as well can be expressed by a two-dimensional vector quantity $\boldsymbol{t} \in \mathbb{R}^2$ with its magnitude being the sensitivity of the interferometer in the direction of $\boldsymbol{t}$. With these prerequisites, we reformulate eq. (3.4) and express the dark-field signal by

$$D_{1/2}(\theta) = \exp\left[-\langle \boldsymbol{\epsilon}_{1/2}, \boldsymbol{t}\rangle^2\right], \tag{3.5}$$

with $\langle\cdot,\cdot\rangle$ denoting the two-dimensional scalar product and $\sqrt{2A_{1/2}} = |\boldsymbol{\epsilon}_{1/2}|\,|\boldsymbol{t}|$.

From the plots in fig. 3.4 and the observations described above, we infer that the superposition signal is given by the product of both single layers:

$$\begin{aligned} D_{1\&2}(\theta) &= D_1(\theta)D_2(\theta) \\ &= \exp\left[-(\langle \boldsymbol{\epsilon}_1, \boldsymbol{t}\rangle^2 + \langle \boldsymbol{\epsilon}_2, \boldsymbol{t}\rangle^2)\right]. \end{aligned} \tag{3.6}$$

This equation describes the directional dark-field superposition principle for two completely anisotropic sample layers passed by an x-ray beam one after the other.

One immediate consequence of this equation is that the superposition of two orthogonal structures of equal scattering strength results in a constant scattering profile with respect to the rotation angle. In Directional Dark-Field Imaging such a sample will appear isotropic (see proof in eq. 3.8 below). Furthermore, every directional dark-field signal will be a superposition of harmonics of the same angular period and consequently be another harmonic with identical period.

For two arbitrary scattering directions and strengths, the logarithmic sum signal can be calculated by simply adding two harmonics. We predicted the results for the superposition signal by multiplying the fit curves of the single sample layers, which is equivalent to that. The expected curves are shown in fig. 3.4 as orange lines and the data points agree with this theoretical model.

Generalizing eq. (3.6) to a sample consisting of infinitesimally thin scattering layers leads to

$$D = \exp\left[-\int \langle \boldsymbol{\epsilon}(z), \boldsymbol{t}\rangle^2 \,\mathrm{d}z\right], \tag{3.7}$$

the line integral for anisotropic scattering samples. In eq. (3.7), $|\boldsymbol{\epsilon}(z)|^2$ is a scattering density instead of the absolute amount of scattering of a single layer, which was denoted by $|\boldsymbol{\epsilon}_{1/2}|^2$ in eq. (3.6). In this model, an isotropic scatterer can be represented by the superposition of two perpendicular scattering directions causing a dark-field signal that is independent of the sample orientation. This is proved most conveniently with the expression given in eq. (3.4) and the superposition principle stated in eq. (3.6). Let $\tau_2 = \tau_1 + 90^\circ$ and $A_1 = A_2$. Then

$$\begin{aligned} D_{1\&2}(\theta) &= \exp\left[-2A_1\cos^2(\theta-\tau_1)\right]\exp\left[-2A_2\cos^2(\theta-\tau_2)\right] \\ &= \exp\left[-2A_1\left(\cos^2(\theta-\tau_1)+\cos^2(\theta-\tau_1-90^\circ)\right)\right] \\ &= \exp\left[-2A_1\left(\cos^2(\theta-\tau_1)+\sin^2(\theta-\tau_1)\right)\right] \\ &= \exp\left[-2A_1\right]. \end{aligned} \tag{3.8}$$

Because of the addition of $\sin^2 x$ and $\cos^2 x$, the direction dependence vanishes. Therefore, the superposition signal $D_{1\&2}(\theta)$ does not depend on the angle of rotation θ and the sample appears isotropic. For a mixed isotropic and anisotropic sample, this leads to an additional constant offset of the cosine curves in the simulated/measured data. Consequently, an arbitrarily scattering sample can always be expressed by a superposition of perfectly anisotropic layers.

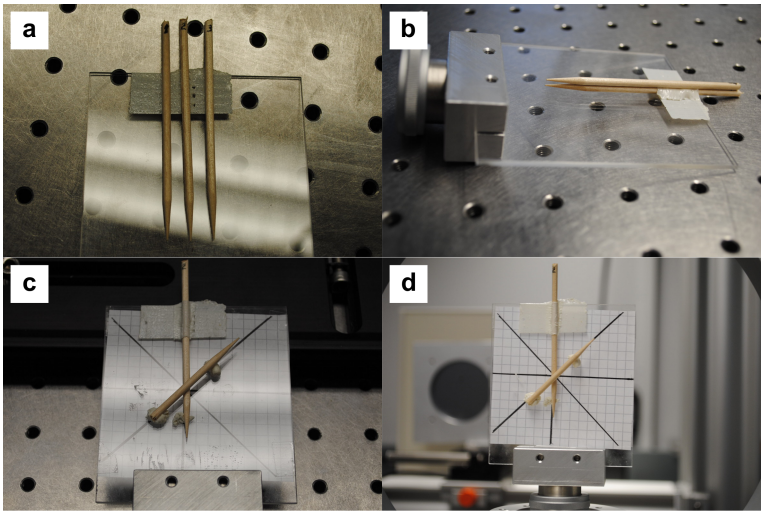

Fig. 3.5: Photographs of the skewer samples. From three skewers, the two with the most homogeneous orientation were selected. They were mounted on a plexiglass panel with double-sided scotch tape. First, each skewer was scanned separately and then both skewers together with several different relative orientations.

3.4 Experimental Realization by a Well-Defined Sample

The experiments were performed at a laboratory setup at the Technische Universität München consisting of a High Power X-Ray tube (MXR-160HP/11 by COMET AG, Switzerland) at an acceleration voltage of 65 kV and a current of 15 mA with a 3.0 mm aluminum filter. The gratings consisted of two absorption gratings (G_0 and G_2) with a silicon substrate height of 500 µm and 150 µm and $160 - 170$ µm high gold lines filled with SU-8 in between. The phase grating was made of 8 µm nickel lines on a 200 µm thick silicon substrate. The period of the gratings was 10 µm for the absorption gratings and 5 µm for the phase grating and their duty cycle was 0.5. A Varian PaxScan 2520D with a CsI scintillator served as x-ray detector.

The samples were measured in air while mounted on a plexiglass (PMMA) panel, which was fixed inside an Eulerian cradle manufactured by Huber Diffraktionstechnik GmbH & Co. KG, Germany. This goniometer allowed rotation of the samples around the beam axis. The distances between the gratings were 92.7 cm, which corresponds to a design energy of 46 keV of the interferometer. The samples were located 28 cm downstream from the phase grating and we ensured that their dark-field signal never reached saturation. In order to avoid noise effects, we applied a threshold when calculating the

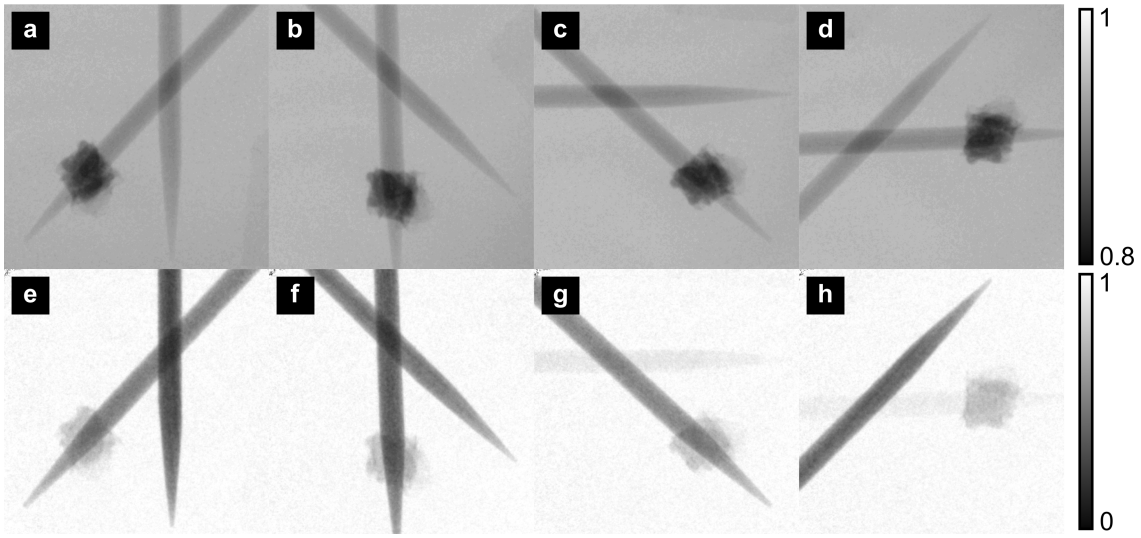

Fig. 3.6: Transmission and dark-field projections for four exemplary sample orientations. a)-d) Transmission radiographs of the two skewers with a relative orientation of 45° for rotation angles $\theta = 0°, 45°, 90°, 135°$. e)-h) Dark-field radiographs for the identical respective orientations. While the local transmission stays the same with respect to the orientation, the dark-field signal changes significantly depending on the relative orientation of the sample structures to the grating lines, which were oriented vertically.

anisotropy data, such that only data points with an average dark-field signal stronger than 0.97 (wooden skewers) or 0.94 (femur cubes) were taken into account.

To realize the simulated situation in experiment, we chose a specimen composed of two wooden skewers located one behind the other in the x-ray beam (see fig. 3.5). For these samples, scattering mainly occurs in directions perpendicular to the skewer axis because of the numerous wooden fibers oriented along this direction (cf. fig. 3.6). From three skewers the two were selected which showed the most homogeneous orientation to keep subsequent errors in the analysis to a minimum. For the experimental demonstration, we utilized a more involved setup than the simplified one used for the simulations above. We used a tube source for illumination, so that the introduction of a source grating (G_0) was necessary to meet the coherence requirements of the setup. Because of this, the illumination was polychromatic as well and the x-ray beam was divergent. Nevertheless, with respect to the physical effects in the sample and the setup, these changes did not affect the experimental results significantly. This can be deduced from the correct cosine-shaped rotation curves of the obtained dark-field signal presented in section 3.5. The angular area occupied by the sample was small enough to neglect the beam divergence. The scattering strength in the sample differs for the various photon energies, but concerning the measured

orientation and anisotropy, every part of the spectrum contributes in the same way.

Fig. 3.7 displays the transmission, average dark-field and anisotropy signals for three different relative orientations ($\Delta\theta = 0°, 45°, 90°$) of the two skewers. Here, the structure orientation is encoded in color, while the anisotropy is given by the brightness. Qualitatively, the superposed average dark-field signal – like the transmission – appears to be the product of the average dark-field signals generated by each skewer alone. As expected from the suggested model, for comparable sample thickness, the orientation of the sum signal is equal to the mean direction of the single skewers. This corresponds to a roughly equal amount of scattering structures in both skewers at this location. For perpendicular scattering directions, the anisotropy in the signal is strongly suppressed. In the following section these observations will be checked by a quantitative analysis.

3.5 Quantitative Check of the Model

A quantitative examination of several representative locations taken from the example in fig. 3.7 is shown in fig. 3.8. In accordance with the plotted directional dark-field curves, the locations containing only a single skewer in the beam path are marked by colored crosses. They are compared to data taken from locations where both skewers overlap. The latter are marked by filled triangles, squares, and circles for relative orientations $\Delta\theta = 0°, 45°$, and $90°$, respectively. Each single directional dark-field signal obeys eq. (3.7). Due to a remaining isotropic contribution caused by wood fibers that are not oriented along the skewer axis, the curves show a small additional offset. We derived the model parameters from these two curves by fitting the model to the data (shown in gray). From the directional dark-field signal of each single sample and the superposition principle derived above, we calculated the expected values for the superposition of both sample layers (shown in orange). The measured superposition signal follows the model in all cases, although some deviations remain. They originate in slight variations between the different locations from which the curves are taken.

For a relative orientation of $\Delta\theta = 45°$, the curves, on the one hand, show the results for a location where both sample layers have almost identical thickness (green) and, on the other hand, for a point moved a bit sideways such that the first layer has almost half the thickness (magenta). Here, the locations of the

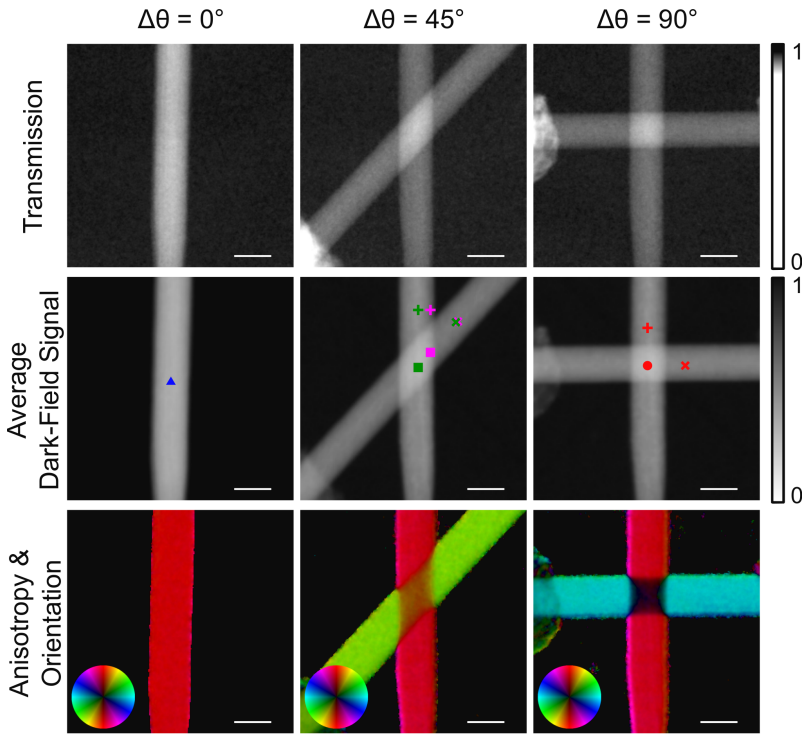

Fig. 3.7: Experimental realization of the simulated scenario of differently oriented layers on top of each other. Two wooden skewers were put on top of each other and examined with respect to different relative orientations. Because the fibers of the wood form highly oriented substructures parallel to one skewer's central axis, each skewer strongly scatters in a well-defined direction perpendicular to its central axis. The color scale has been adapted to increase the contrast for the transmission images. Compared to the rather weak absorption of the material, the dark-field signal clearly predominates for this kind of sample. Shown in the middle row, the mean value of the dark-field signal with respect to the rotation increases where the skewers overlap. A quantitative analysis shows that the superposition signal is the product of the mean directional dark-field values of each skewer, as it is the case for the transmission (cf. figs. 3.4 and 3.8). In the bottom row, the anisotropy images encode the direction of the structures in the color and the degree of anisotropy in the brightness. For completely parallel orientation of the two skewers ($\Delta\theta = 0°$), the superposition shows the same orientation. For an angle of $\Delta\theta = 45°$ between them, the resulting signal depends on the amount of material penetrated by the beam. Wherever both thicknesses are equal, the measured orientation is exactly the circular mean of both individual orientations. Otherwise, intermediate orientations appear wherever the penetrated thickness of one of both skewers is larger than for the other. For an angle of 90° and equal thicknesses, the anisotropy signal completely cancels out. Length of the scalebar: 5 mm.

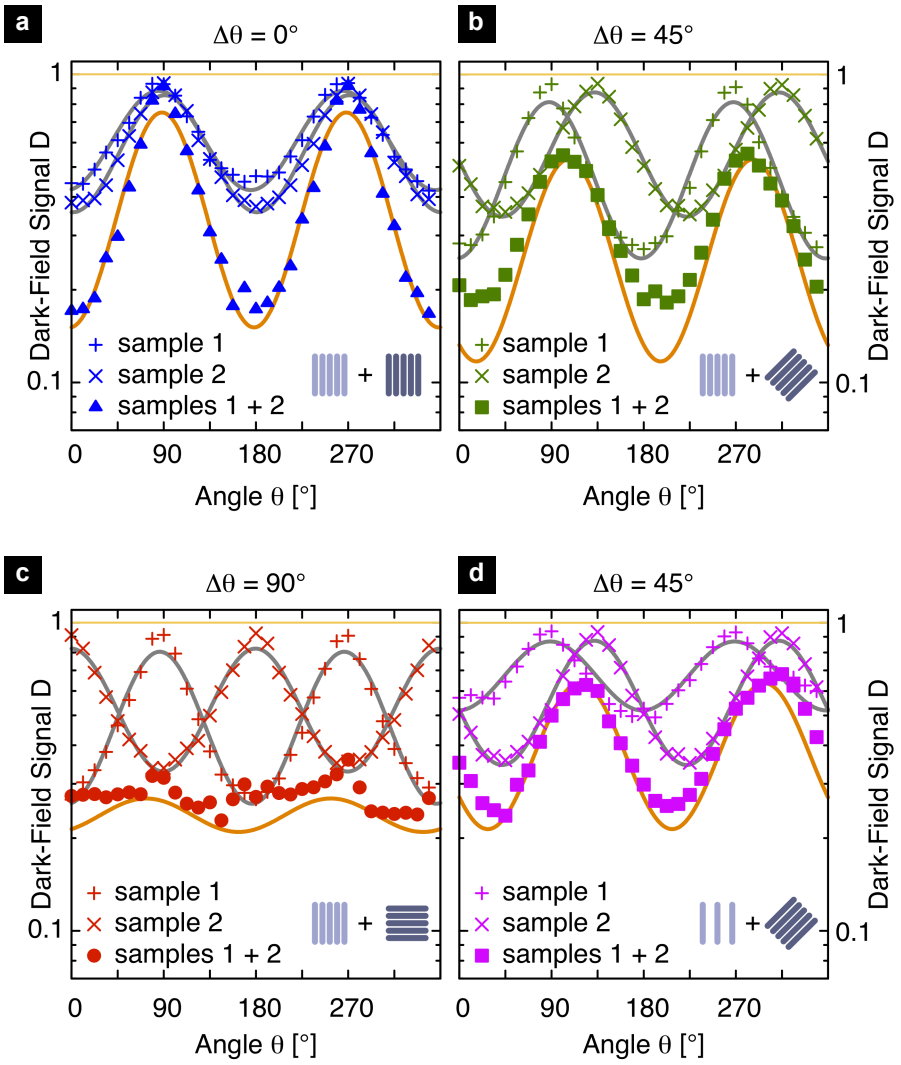

Fig. 3.8: Quantitative evaluation of the superposition principle at specific locations of the combined samples. a)-d) The positions from which the curves were taken correspond to locations on the wooden skewers, where either one of them were penetrated by the x-ray beam or both after each other. They are marked in fig. 3.7 by the corresponding symbols. For the parallel oriented samples shown in a), the single layer data were taken from separate scans of the single samples. To test the validity of the model derived from the simulation results, fit curves were calculated for the single samples shown in gray. The predicted superposition signals resulting from the fit parameters and the model are shown in orange color. The direction-dependent curves for the superposition of both samples coincide with the predictions drawn from the model and both single curves for every relative orientation between the two wooden skewers.

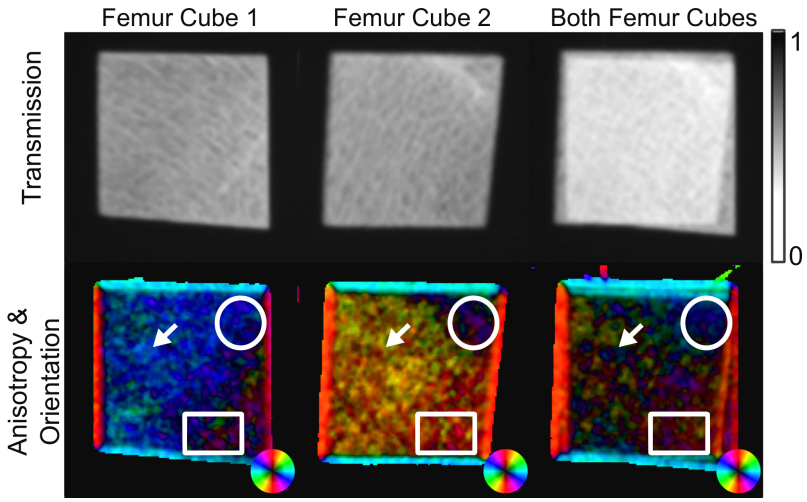

Fig. 3.9: A clinically relevant example for the application of the derived model. Here, the two sample layers consist of human femoral bone cut in cubes. Both cubes were each measured separately with the beam penetrating cube 1 in the anterior-posterior and cube 2 in the medial-lateral direction, and then once again when both cubes were placed on top of each other but oriented in the same way. The upper image row shows the resulting transmission images and the lower row the measured orientation and anisotropy. As before, the anisotropy images encode the direction of the structures in the color and the degree of anisotropy in the brightness. Depending on the local amount of anisotropy in both separate samples, the local direction of the combined sample is either dominated by one of the components (regions marked with circle and rectangle) or the anisotropy is strongly reduced because the average structure orientations are perpendicular to each other between both cubes (arrow).

superposition curve's extrema clearly move towards the locations of those of the skewer which has the stronger scattering contribution. As the scattering mainly depends on the amount of scatterers, this is the skewer which is thicker at the chosen location.

3.6 Application to Biomedical Specimens

Fig. 3.9 shows a biomedical example of an application of the superposition principle: Transmission and directional dark-field images of two human trabecular bone cubes, which were harvested from the femoral head of one female individual. In contrast to cortical bone, trabecular bone is a sponge-like structure of calcified bone matrix. The trabecular microstructure is aligned with the principle stress trajectories. Consequently, there exist preferred structure orientations depending on the anatomical location inside the femur.

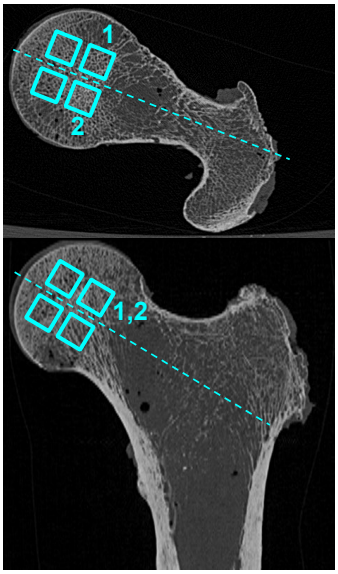

Fig. 3.10: Illustration for the harvesting process of the femoral bone cubes. The original anatomical locations and orientations of both cubes are marked with their indices.

Both cubical bone specimens ($10 \times 10 \times 10\,\mathrm{mm}^3$) were harvested from the head of a fresh frozen human femur (62 year-old female, 1.62 m, 72 kg). The femur was scanned with a 256 row multidetector CT (Philips Medical Care, Best, Netherlands) and no pathological lesions were observed on the macroscopic scale. Previous to the cutting process, the center of the femoral head and neck were mechanically defined. The specimens were cut from the center of the femoral head according to the anatomical direction of the femoral neck (cf. fig. 3.10). They were irrigated with 0.9 % saline during machining using a low speed diamond saw (Dia Tech, Dia BS200, GmbH, Stuttgart, Germany). Thereafter, the bone specimens were defatted chemically by submerging them in ethanol and acetone to allow storage for all imaging procedures. The donor had dedicated her body for educational and research purposes to the local Institute of Anatomy prior to death, in compliance with local institutional and legislative requirements. Written informed consent was obtained from the donor. The study was reviewed and approved by the local institutional review boards (Ethikkommission der Fakultät für Medizin der Technischen Universität München, Germany).

The two cubes were once measured separately with the viewing direction aligned along the anterior-posterior (cube 1) and the medial-lateral direction (cube 2). In the first case, the superior-inferior direction was pointing upward, while in the second case it was the anterior-posterior direction. The relative orientation was kept constant for the whole experiment.

Both femoral cubes showed a distinct preferred orientation as expected (cf. fig. 3.9, left and middle column). Their structures pointed roughly in perpendicular directions. In addition to that, another measurement was carried out, where both cubes were put on top of each other (cf. fig. 3.9, right column).

Depending on the amount of anisotropy found in each separate cube, the directional dark-field image of the combined sample shows a preferred direction that is more or less equal to the dominating component. Two such areas are marked by a circle (dominated by cube 1) and a rectangle (dominated by cube 2). A large fraction of the area that is occupied by both cubes in the combined sample shows less if no anisotropy at all. One location with strongly reduced anisotropy is marked by an arrow in the figure. This follows directly from the superposition model derived above and the perpendicular orientation of the structures between both cubes (cf. eq. (3.8)).

3.7 Conclusion

In summary, we have shown how the directional dark-field signal drawn from x-ray grating interferometry can be calculated for samples that are composed of highly anisotropic layers of differing orientation. Starting from theoretical predictions gained from simulations, we developed a model for the superposition of the signals originating in two different sample slices: The harmonic oscillations observed for the single layers can simply be added to retrieve the superposition signal. As a direct consequence, layers with perpendicular orientation and similar scattering strength will show no anisotropy in dark-field imaging. We checked the correctness of this model by means of experimental data and found very good agreement.

With this model at hand, it is now possible to predict and describe the directional dark-field signal for thick samples containing more than one layer of oriented scatterers. It will be extended in chapter 4 to perform direction-dependent computed tomography based on the dark-field signal. This will allow to reconstruct the sub-pixel structure orientation and anisotropy with respect to the exact anatomical location.

4 X-Ray Tensor Tomography

When I investigated the advantages over conventional X-ray techniques however, it became apparent that the conventional methods were not making full use of all the information the X-rays could give.

Godfrey N. Hounsfield [49]

The physical model for Directional Dark-Field Imaging, which was developed in chapter 3, applies to radiographic methods only. It suffers from averaging over all structures, which are passed by the x-ray beam. In the following, I will show how to combine the directional dark-field signal with computed tomography and reconstruct the local direction-dependent scattering of the sample. Because the scattering is represented by a tensor in every sample point, this reconstruction technique is called X-Ray Tensor Tomography (XTT). Most parts of this chapter will be published under the title "X-Ray Tensor Tomography" together with Guillaume Potdevin, Thomas Biernath, Elena Eggl, Konstantin Willer, Tobias Lasser, Jens Maisenbacher, Jens Gibmeier, Alexander Wanner, and Franz Pfeiffer [67]. Section 4.1 gives an account on the underlying theory. The experimental data were obtained from a well-defined specimen, which is described in section 4.2. The setup and scanning parameters are discussed in section 4.3 followed by a discussion of the reconstruction algorithm in section 4.4. In section 4.5 the correct reconstruction of the sample's scattering parameters is proven by comparing it to high-resolution micro-tomograms from the same specimen.

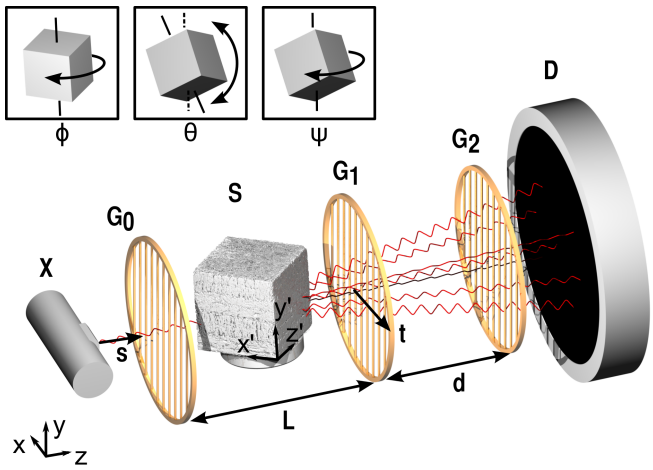

Fig. 4.1: Sketch of the X-Ray Tensor Tomography setup. It consists of an x-ray source (X), a sample (S), the grating interferometer (G_0, G_1, and G_2) and a detector (D). $\boldsymbol{s} \in \mathbb{R}^3$ and $\boldsymbol{t} \in \mathbb{R}^3$ mark the x-ray beam direction and the interferometer's direction of sensitivity (vertical to the grating lines), respectively. Here, the sample is a carbon fiber cube, which is mounted on a three-circle Eulerian cradle, a goniometer type often used in crystallography, and rotated around a fixed rotation center covering the maximum available spatial angular range. The orientation is defined by the three Eulerian angles (ψ, θ, and ϕ) as described in section 1.4. For each orientation, an x-ray dark-field image is recorded. For clarity, the laboratory and sample coordinate systems are shown as well.

4.1 Theory

The experimental approach of X-Ray Tensor Tomography is based on combining an imaging setup with multi-dimensional sample orientation (as known from crystallography). In this study, a typical laboratory-based experimental setup for grating interferometry was used (see fig. 4.1), but synchrotron-based imaging is equally possible. The setup consisted of an x-ray tube as source (X), a Talbot-Lau grating interferometer with three gratings (G_0, G_1, and G_2), and a detector (D). The sample (S) was mounted on a three-circle Eulerian cradle placed between source and phase grating. Consequently, its orientation could be chosen almost arbitrarily within a wide spatial angular range only limited by the goniometer's geometry. By contrast, for both dark-field tomography (cf. section 1.5) and Directional Dark-Field Imaging (cf. chapter 3), only a single axis of rotation is required.

To reconstruct direction-dependent x-ray scattering, we developed a physical model starting from relations well-known from Directional Dark-Field Imaging. It has been shown in section 3.3 that the physical model behind X-Ray Direc-

tional Dark-Field Imaging can be described by

$$D(x,y) = \exp\left[-\int \langle \boldsymbol{\epsilon}(x,y,z), \boldsymbol{t}\rangle^2 \,\mathrm{d}z\right]. \tag{4.1}$$

This is a relation similar to the Beer-Lambert law for the absorption of x-rays penetrating matter. Here x, y, and z are given relative to the laboratory coordinate system. D denotes the measured dark-field signal, and $\langle\cdot,\cdot\rangle$ the Euclidian scalar product, $\boldsymbol{\epsilon}(x,y,z) \in \mathbb{R}^3$ is the location-dependent scattering density introduced by the sample, and $\boldsymbol{t} \in \mathbb{R}^3$ the sensitivity vector of the grating interferometer. $\boldsymbol{t}$ describes the absolute sensitivity and its direction at the same time. It always points in a direction parallel to the grating surface but perpendicular to the grating lines. The magnitude of the sensitivity vector depends on the setup parameters of the interferometer, the sample location, and the x-ray photon energy. The scattering as well is energy-dependent and characterized by its direction and magnitude as represented by $\boldsymbol{\epsilon}$. In chapter 3, $\boldsymbol{t}$ and $\boldsymbol{\epsilon}$ were two-dimensional quantities, as the sample was rotated around the beam axis and the third dimension could safely be ignored. Now, because the sample will be oriented arbitrarily, both are given in three dimensions. For this work, we ignored all deviations that may have been caused by the polychromatic energy spectrum and reconstructed effective values.

X-Ray Directional Dark-Field Imaging is a two-dimensional technique, which works best for thin specimens that contain only few structure layers. Otherwise, it would be unfeasible to deduce the structure orientation from the scattering signal because of ambiguities [65, 66]. By contrast, computed tomography allows to reconstruct physical quantities in 3D with respect to the location, but requires an adaption of the line-integral for Directional Dark-Field Imaging. Therefore, we generalized the existing model for Directional Dark-Field Imaging by allowing a finite number $O \in \mathbb{N}$ of different scattering directions $\boldsymbol{\epsilon}_\alpha \in \mathbb{R}^3$ at every sample position. When performing tomography, the sample is rotated relative to the penetrating beam. As a consequence, the scattering in each voxel also depends on the direction of the incoming beam $\boldsymbol{s} \in \mathbb{R}^3$ relative to the sample coordinate system. These considerations lead to

$$D(x,y) = \exp\left[-\int \sum_{\alpha=1}^{O} \langle \boldsymbol{\epsilon}_\alpha(\boldsymbol{s},x,y,z), \boldsymbol{t}\rangle^2 \,\mathrm{d}z\right]. \tag{4.2}$$

This is the basis for calculating the x-ray scattering tensor at every sample location after reconstructing the discrete scattering contributions $\boldsymbol{\epsilon}_\alpha(\boldsymbol{s},x,y,z)$. We chose to fit an ellipsoid to the scattering data to calculate the tensor coefficients.

As already shown in section 3.3 and in [65, 66], it is impossible to distinguish between an isotropic scattering sample and two completely anisotropic layers put close to each other but with a relative orientation of 90°. Thus, we can ignore constant scattering contributions by absorbing them in at least two perpendicular anisotropic contributions. If we ensure that enough different scattering directions are available, even isotropic scattering contributions can be handled by this model. They will be distributed more or less equally over all scattering directions. This also avoids ambiguities with respect of the representation of isotropic scatterers.

To be able to perform a reconstruction, we still need to specify how $\boldsymbol{\epsilon}_\alpha(\boldsymbol{s}, x, y, z)$ changes when rotating the sample, which is equivalent to changing the direction of the incoming beam $\boldsymbol{s}$. Here, we assume that the scattering direction is always fixed with respect to the sample's coordinate system but the amount changes with the relative orientation of $\boldsymbol{\epsilon}_\alpha$ and $\boldsymbol{s}$ like

$$\boldsymbol{\epsilon}_\alpha(\boldsymbol{s}, x, y, z) = |\hat{\boldsymbol{s}} \times \hat{\boldsymbol{\epsilon}}_\alpha(x, y, z)|\, \boldsymbol{\epsilon}_\alpha(x, y, z). \tag{4.3}$$

Here, $\hat{\cdot}$ denotes the vector normalized to unit length, $\times$ the vector product, and $|\cdot|$ is the Euclidian vector norm. $\boldsymbol{\epsilon}_\alpha(x, y, z) \in \mathbb{R}^3$ now is a quantity independent of the illumination vector and represents the scattering in a fixed direction but with an arbitrary magnitude.

Using (4.3), we can substantiate (4.2):

$$D(x, y) = \exp\left[-\int \sum_{\alpha=1}^{O} \left(|\boldsymbol{\epsilon}_\alpha(x, y, z)|\, |\boldsymbol{t}|\right)^2 \left(|\hat{\boldsymbol{s}} \times \hat{\boldsymbol{\epsilon}}_\alpha|\, \langle \hat{\boldsymbol{\epsilon}}_\alpha, \hat{\boldsymbol{t}} \rangle\right)^2 \mathrm{d}z \right]. \tag{4.4}$$

All values of the weight factor

$$v_\alpha := \left(|\hat{\boldsymbol{s}} \times \hat{\boldsymbol{\epsilon}}_\alpha|\, \langle \hat{\boldsymbol{\epsilon}}_\alpha, \hat{\boldsymbol{t}} \rangle\right)^2 \tag{4.5}$$

can be precalculated from the corresponding sample orientation for a given recording scheme. For parallel geometry, they are constant for all rays contributing to a single projection image. The results presented below show the reconstruction of the product of the absolute values of $\boldsymbol{\epsilon}_\alpha(x, y, z)$ and $\boldsymbol{t}$,

$$\zeta_\alpha(x, y, z) = |\boldsymbol{\epsilon}_\alpha(x, y, z)|\, |\boldsymbol{t}|\,, \tag{4.6}$$

which we will call effective scattering strength. This is equivalent to the assumption that all sample voxels contain an identical distribution of scatterers

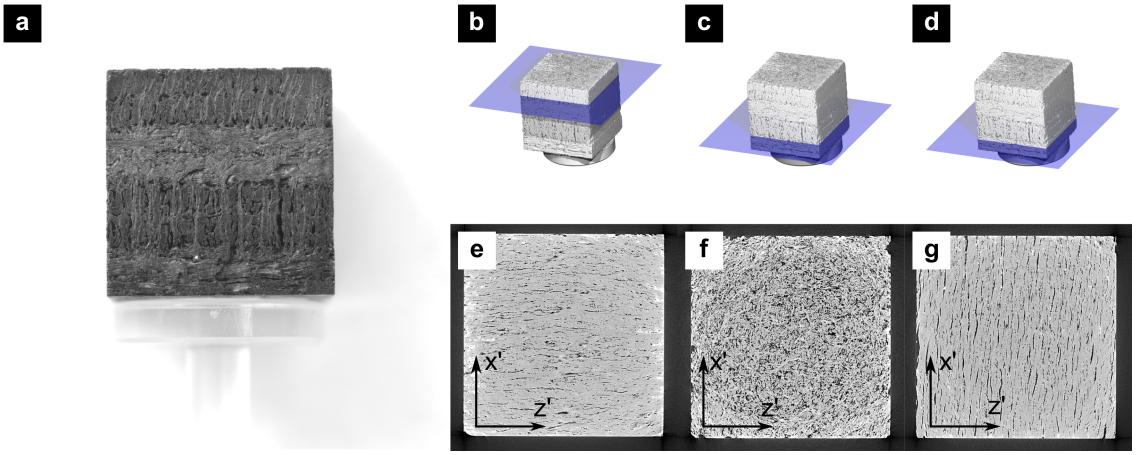

Fig. 4.2: The carbon cube sample. a) Photograph of the carbon cube specimen mounted on a PMMA disk. The change in fiber orientation between the layers can be observed directly. b)-d) Three-dimensional renderings of the specimen showing the position of the cross-sections depicted in e)-g). e)-g) Micro-tomographic slices from the planes that were marked in b)-d), respectively. They show the changes in orientation of the structures in the different sample layers. In e), most structures are aligned along the z' direction and consequently cause scattering along the x' axis. f) shows an intermediate felt layer, which is completely isotropic. In g), the structures are oriented along the x' axis and cause scattering in the z' direction.

with respect to their size and material. If one can furthermore assume that the sensitivity is more or less constant and known, this directly allows to reconstruct the scattering caused in each sample voxel. In general, this is not applicable, as the sensitivity strongly depends on the x-ray photon energy and structure dimensions. How to separate the two contributions from scattering and sensitivity and correctly model the energy dependence, will be part of future examinations.

4.2 The Investigated Sample

The specimen investigated in this study was a block of carbon fiber reinforced carbon (see fig. 4.2a)). The concept behind such compound materials in general is to combine beneficial features of two or more materials or material states, for instance low density at a high crack resistance, which gives these kinds of materials a broad field of application in engineering. The basic idea with this combination is to use the anisotropic properties of graphite to reinforce a carbon structure giving access to a light but strong material at a high thermal stability.

The sample was created from several layers of carbon fibers, which were then infiltrated with the carbon matrix by chemical vapor infiltration (CVI). This was done at the Institute for Chemical Technology and Polymer Chemistry at the Karlsruhe Institute of Technology (KIT). Blocks of $15 \times 50 \times 55\,\mathrm{mm}^3$ size were streamed under isothermal and isobaric conditions with methane. The specific correlations between infiltration parameters and resulting carbon-carbon structures can be found in [68]. The specimen researched in this work has been infiltrated at 1095 °C and 25 kPa for 90 h with a dwell time of 0.1 s. The carbon fiber laminate is commercially available ("Surface Transforms", Ellesmare Port, UK) and consists of HT-fibres (Panox®, SGL Carbon) with a Young's modulus of 190 GPa and a density of $1.72\,\mathrm{g/cm}^3$.

Due to the fabrication process, the carbon reinforced carbon (CFC) materials described in this chapter exhibit a certain porosity. In earlier studies, it has already been shown that pore networks in CFC materials based on a pure felt-like fiber structure are connecteded, whereas in specimens as in this investigations the pore networks between each layer are quite separated [69]. Furthermore, prolate shaped pores tend to appear parallel and oblate shaped ones perpendicular to the main fiber direction.

From one of the large carbon blocks, a cube of size $1.03\,\mathrm{cm} \times 1.03\,\mathrm{cm} \times 1.02\,\mathrm{cm}$ was cut, which served as specimen in our study. It contained eight layers of oriented fibers. The fibers in each layer mainly pointed in one direction. All layers were separated by thinner felt layers with an arbitrary fiber orientation resulting in a total of fifteen different layers. Groups of two equally oriented layers were oriented perpendicular towards each adjacent group and parallel to the upper/lower surface of the cube. All the layers were woven together by strings of fibers from the top to the bottom. 60 % of the fibers were oriented in each layer's main direction, 30 % connected the different layers in vertical direction, and the remaining 10 % were directed perpendicular to the other two orientations.

To get an insight into the inner structure, we recorded absorption-based microtomograms of the specimen at a very higher resolution (cf. fig. 4.2b)-g)). These micro-CT measurements were carried out at Technische Universität München at a v|tome|x s 240 by GE Sensing & Inspection Technologies GmbH (Germany). The scan parameters were 50 kV and 350 µA with an exposure time of 2000 ms averaging over 3 images and 1000 angular steps over 360°. The resulting voxel size was 17.896 µm. One can clearly distinguish oriented pore networks of alternating orientation (fig. 4.2e)+g)) and the intermediate felt layers (fig. 4.2f)). The felt layers are expected to produce a rather isotropic scattering signal, whereas the oriented layers should be clearly distinguishable by their anisotropic scatter-

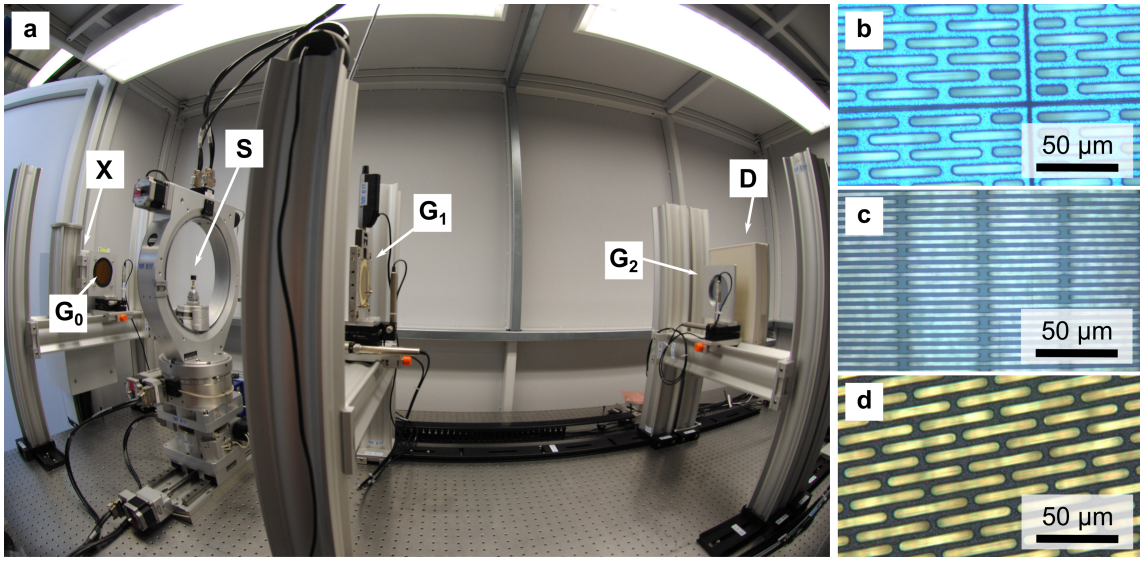

Fig. 4.3: The experimental realization of the X-Ray Tensor Tomography setup. a) As in fig. 4.1, the setup consisted of an x-ray tube (X), the grating interferometer (G_0, G_1, and G_2), the sample (S) and a detector (D). The sample was mounted on a three-circle Eulerian cradle allowing free rotations around any axis. b)-d) Visible light microscopy images showing the structures of the three gratings G_0, G_1, and G_2, respectively (see section 4.3 for grating parameters). For better stability of the grating structures their layout deviates from the ideal binary ruling by additional supporting bridges.

ing profile.

4.3 Experimental Setup and Scanning Parameters

We carried out the X-Ray Tensor Tomography experiments at a laboratory setup at the Technische Universität München (see fig. 4.3). A High Power X-Ray tube (MXR-160HP/11 by COMET AG, Switzerland) served as x-ray source and was accompanied by a Varian PaxScan 2520D with a CsI scintillator as detector with a pixel pitch of 127 µm and a scintillator thickness of 600 µm (Varian medical systems, USA). We chose an acceleration voltage of 90 kV and an anode current of 8 mA with an additional aluminum filter of 3.0 mm thickness. The interferometer consisted of two transmission gratings (G_0 and G_2) with a silicon substrate height of 500 µm and 150 µm and $160 - 170$ µm high gold lines and spaces filled with SU-8. Our phase-shifting grating (G_1) induced a phase shift of $\pi/2$ at the targeted design energy of 56.9 keV and was made of 10 µm nickel lines on a 200 µm thick silicon substrate. We used a symmetric setup with an inter-grating distance of $L = d = 1.15$ m. The period of the gratings was 10 µm for the ab-

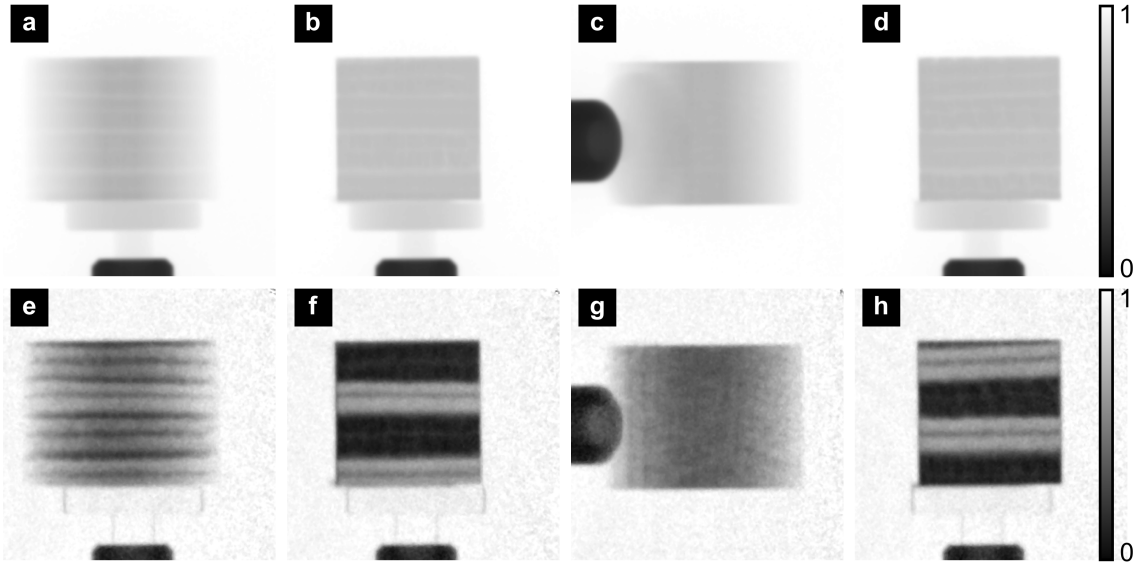

Fig. 4.4: Transmission and dark-field projections for four exemplary sample orientations. a)-d) Transmission radiographs for the following sample orientations (ϕ, θ, ψ): $(0°, 0°, -36°)$, $(0°, 0°, 0°)$, $(0°, 90°, -36°)$, $(90°, 0°, 0°)$. e)-h) Dark-field radiographs for the identical respective orientations. While the local transmission stays the same with respect to the orientation, the dark-field signal changes significantly. The dark-field contrast between the differently oriented sample layers even is inverted between f) and h). The grating lines were oriented vertically.

sorption gratings and 5 µm for the phase grating and all duty cycles were 0.5. A three-circle Eulerian cradle manufactured by Huber Diffraktionstechnik GmbH & Co. KG, Germany served as sample mounting system. It was placed such that the sample was located 89 cm from the source grating, which resulted in a magnification of 2.6. This allowed to assume parallel beam geometry for the computed tomography reconstruction problem later on.

As the contribution of each scattering component depends on the relative orientation with respect to the beam direction and the setup is sensitive only perpendicular to the grating lines, it was necessary to rotate the sample not only around a single rotation axis but freely around the center of rotation of the Eulerian cradle. Otherwise there would have been scattering coefficients ζ_α with a constant weight factor v_α equal to 0. The sample was rotated freely around the center of rotation of the Eulerian cradle covering the following Eulerian angle values:

$$\begin{aligned} \phi &\in \{0°, 45°, 90°, 135°\}, \\ \theta &\in \{0°, 45°, 90°, 135°\}, \\ \psi &\in \{-36.67°, -36.00°, -35.33°, -34.67°, \ldots, 36.67°\}. \end{aligned}$$

This resulted in a total number of 1776 projections. The sample and laboratory coordinate systems and the Eulerian angles were defined as described in section 1.4. During the experiment, ψ was used as fastest and ϕ as slowest axis. For each sample orientation the phase grating was scanned in 8 steps over one grating period (phase stepping, cf. section 1.2). Reference images were taken before and after scanning the fast axis completely. We calculated the three different contrast signals from the Fourier transform of the resulting intensity variation as described in section 1.3. Only transmission and dark-field contrast was used for this study. Figure 4.4 displays exemplary transmission projections and the corresponding dark-field images for four different sample orientations. The local transmission in the sample does not change with the rotation. By contrast, the dark-field signal strongly depends on the orientation of the sample.

4.4 The Reconstruction Algorithm

For the reconstruction, we discretized the sample volume with cubic volume elements (voxels) and used the Simultaneous Algebraic Reconstruction Technique (SART) [54]. Therefore, the SART algorithm presented in section 1.5 had to be adapted to the physical model of X-Ray Tensor Tomography given by eq. (4.4). The reconstructed quantity is the squared effective scattering strength $\zeta_\alpha^2(x,y,z) = |\epsilon_\alpha(x,y,z)|^2 |t|^2$, as $\zeta_\alpha(x,y,z)$ appears squared in eq. (4.4). Therefore, we introduce the auxiliary quantity

$$\eta_\alpha(x,y,z) = \zeta_\alpha^2(x,y,z), \tag{4.7}$$

which will be reconstructed by the algorithm. Afterwards, $\zeta_\alpha(x,y,z)$ is calculated from the reconstructed values by applying the square root. The discretized quantity corresponding to $\eta_\alpha(x,y,z)$ shall be denoted by $\eta_{\alpha j}$ with $1 \leq \alpha \leq O$. As before, α determines the scattering component and j specifies the voxel index. For SART, all rays arriving at the detector pixels i that form a single projection image $P_{(\phi,\theta,\psi)}$ are treated simultaneously. In introductory section 1.5, the projections were specified by a single angle only. As we need more rotational degrees of freedom for XTT, the exact projection now is specified by the triplet (ϕ,θ,ψ). The measurement values p_i for XTT are not the logarithmic relative intensities of conventional tomography but the measured logarithmic dark-field signals. As in section 1.5, i shall specify the detector pixel and the rotation step. For a single update step k to $k+1$, one distinct sample orientation and the corresponding projection image $P_{(\phi,\theta,\psi)_k}$ is required. The order, in which the projections are processed during a single iteration, is randomized. In general,

for an arbitrary setup geometry, the weight factors v_α depend on the location inside the volume and on the chosen ray i arriving at detector pixel p_i. For this reason, their discretized realizations are denoted by $v_{\alpha ij}$. With these prerequisites, the SART update equation for X-Ray Tensor Tomography can be written as

$$\eta_{\alpha j}^{(k+1)} = \eta_{\alpha j}^{(k)} + \frac{\sum\limits_{i \in P_{(\phi,\theta,\psi)_k}} \lambda_\mathrm{u} \frac{p_i - \sum\limits_{\beta=1}^{O} \sum\limits_{n=1}^{N} w_{in} v_{\beta in} \eta_{\beta n}^{(k)}}{\sum\limits_{\beta=1}^{O} \sum\limits_{n=1}^{N} w_{in} v_{\beta in}} w_{ij} v_{\alpha ij}}{\sum\limits_{\beta=1}^{O} \sum\limits_{i \in P_{(\phi,\theta,\psi)_k}} w_{ij} v_{\beta ij}}, \forall 1 \leq j \leq N. \tag{4.8}$$

As in section 1.5, the forward projection is marked in red and the backward projection in blue in eq. (4.8). In addition to the conventional weight factors of SART, the equation contains the new weights for each scattering component.

It has been mentioned above, that $v_{\alpha ij}$ is independent of the location in the reconstructed volume and constant for all rays of a certain projection if the illumination is with parallel rays. This constant value shall be denoted by $\tilde{v}_{\alpha k}$ and $\tilde{v}_{\alpha k} = v_{\alpha ij}$ for all j and all $i \in P_{(\phi,\theta,\psi)_k}$. Thus, for a single update step k to $k+1$, $v_{\alpha ij}$ varies only with the index α and eq. (4.8) can be simplified by substituting $v_{\alpha ij}$ with $\tilde{v}_{\alpha k}$ and factorizing the constant factors out:

$$\eta_{\alpha j}^{(k+1)} = \eta_{\alpha j}^{(k)} + \frac{\tilde{v}_{\alpha k}}{\left(\sum\limits_{\beta=1}^{O} \tilde{v}_{\beta k}\right)^2} \cdot \frac{\sum\limits_{i \in P_{(\phi,\theta,\psi)_k}} \lambda_\mathrm{u} \frac{p_i - \sum\limits_{\beta=1}^{O} \sum\limits_{n=1}^{N} w_{in} \tilde{v}_{\beta k} \eta_{\beta n}^{(k)}}{\sum\limits_{n=1}^{N} w_{in}} w_{ij}}{\sum\limits_{i \in P_{(\phi,\theta,\psi)_k}} w_{ij}}, \forall 1 \leq j \leq N. \tag{4.9}$$

From this equation, one can see that the conventional SART algorithm only has to be extended by a multiplication with an additional factor of $\tilde{v}_{\alpha k}(\sum_{\beta=1}^{O} \tilde{v}_{\beta k})^{-2}$ before performing the actual update and an additional weighted summation in the forward projection step. In the algorithm used for the results presented in this thesis, the backprojection step contained the multiplication with the conventional update weight λ_u and the additional XTT weights to improve its performance. The following listing shows the algorithm in python pseudocode:

Listing 4.1: The SART algorithm used for X-Ray Tensor Tomography (python pseudo code).

```
import numpy

# Initialize volume
volume = numpy.zeros(volume_size, dtype=numpy.double)

# Until convergence or - in this case - until a certain
# number of iterations is reached
for iteration in range(number_of_iterations):
    # Generate a random permutation of the set of
    # projection indices
    angle_indices = numpy.random.permutation(
                                        number_of_projections)

    # Iterate over all projections (in random order)
    for random_index in angle_indices:
        # Image projection: Compute line integrals through
        # all detector pixels of the currently selected
        # projection
        temp = project_and_weight(xtt_weights, volume,
                                        angles[random_index])

        # Correction image: For all detector pixels
        # calculate the correction images from the
        # difference to the measured projections
        difference = projection[random_index] - temp

        # Image backprojection: Distribute corrections
        # onto grid
        volume += backproject_and_weight(update_weight,
                                    xtt_weights, difference,
                                    angles[random_index])
```

Instead of reconstructing only a single volume, several volumes are reconstructed in parallel, one for each scattering component α. Therefore, the variable `volume` contains values for each volume element and scattering component. For forward and backward projection, we rotated the volume using trilinear interpolation and subsequently summed along the beam direction.

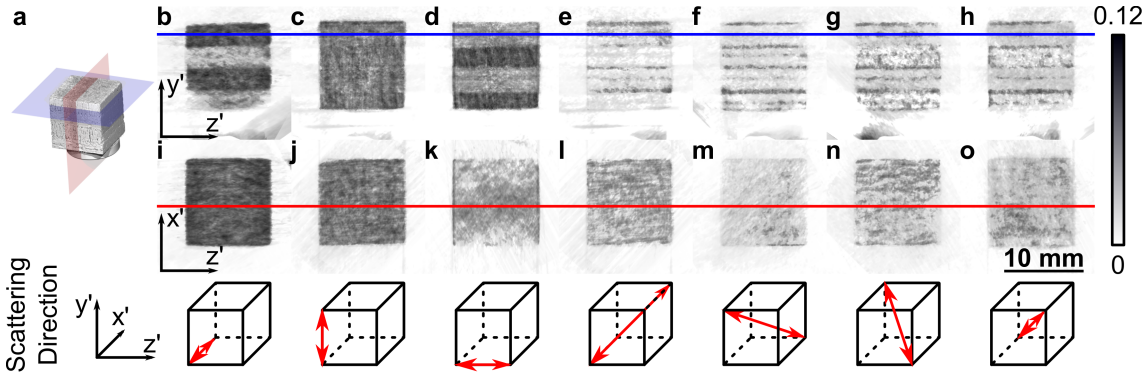

Fig. 4.5: Reconstructed slices by scattering component. a) A three-dimensional rendering of the specimen based on micro-CT. b)-h) show the effective scattering strength along the slice marked in red in a) with respect to the scattering direction. The corresponding directions are given in the bottom row. i)-o) show the same scattering components but now along the slice marked in blue. The broken lines mark the position of the slices with respect to each other. When moving along the sample's y' axis the strongest scattering direction inside the sample alternates between the x' direction and the z' direction. The scattering parallel to the y' axis is almost constant throughout the whole cubic specimen. At the locations of the intermediate felt layers, the fiber orientation is isotropic, which becomes visible in the equal distribution of the scattering power over all scattering components, even the diagonal ones.

4.5 Raw Reconstruction Results

The SART reconstructions for the carbon cube sample were done with a total of four iterations over all projection images. Afterwards, no significant changes in the reconstructed volume could be observed. Each voxel had an edge length of 49 µm such that the whole sample was approximately covered by 206^3 voxels. The projection images were cropped around the center of rotation to 358×358 pixels in size. The resulting volume of scattering coefficients was weighted with an exponential windowing function generated from the absorption data to suppress artifacts outside the specimen caused by the goniometer. Fig. 4.5 shows two representative slices of the raw results gained from reconstructing the effective scattering coefficients for seven different scattering orientations, along the three Cartesian coordinate axes and the four space diagonals. In the sample coordinate system these are

$$\hat{\boldsymbol{\epsilon}}_1 = \begin{pmatrix}1 & 0 & 0\end{pmatrix}^T,\ \hat{\boldsymbol{\epsilon}}_2 = \begin{pmatrix}0 & 1 & 0\end{pmatrix}^T,\ \hat{\boldsymbol{\epsilon}}_3 = \begin{pmatrix}0 & 0 & 1\end{pmatrix}^T,$$
$$\hat{\boldsymbol{\epsilon}}_4 = \frac{1}{\sqrt{3}}\begin{pmatrix}1 & 1 & 1\end{pmatrix}^T,\ \hat{\boldsymbol{\epsilon}}_5 = \frac{1}{\sqrt{3}}\begin{pmatrix}1 & -1 & 1\end{pmatrix}^T,$$
$$\hat{\boldsymbol{\epsilon}}_6 = \frac{1}{\sqrt{3}}\begin{pmatrix}1 & 1 & -1\end{pmatrix}^T,\ \hat{\boldsymbol{\epsilon}}_7 = \frac{1}{\sqrt{3}}\begin{pmatrix}1 & -1 & -1\end{pmatrix}^T.$$

We limited the number of scattering directions to 7 to save memory and computation time. In the figure it becomes evident that the scattering occurring inside the sample is mainly along the Cartesian coordinate axes and alternating between the x' and the z' direction when moving along the y' axis, while it is almost constant in the y' direction throughout the whole specimen. Mainly only at the locations of the intermediate felt layers, the diagonal scattering components show a significant contribution. For a fixed height y' inside the specimen, the scattering in all components is rather homogeneous.

In general, scattering only occurs perpendicular to the structures in the sample. This leads to a strong dark-field signal pointing in these directions. From the reconstructed scattering components, one can deduce that, because of the maximum scattering strength alternating between the x' and z' direction, the main orientation of the structures between the corresponding layers must be alternating as well. Strictly speaking, the scattering structures in the uppermost layer and the second lowest have to point in the z' direction and the features in the remaining two layers have to point in the x' direction. As all fiber layers are stacked on top of each other in y' direction, no change in the vertical scattering component can be observed.

However, the amount of scattering appears to be independent of the relative amount of fibers that point in the different directions. Otherwise, the main scattering direction would have to be along the y' axis. One possible explanation are the pores between the fibers stemming from the production process of the carbon cube material and the interferometric setup being most sensitive to structural changes at larger lengthscales than the fiber thickness, which is around 15 µm. Moreover, because of the infiltration of the carbon fibers with additional carbon, most of the material also could appear rather homogeneous and only the remaining pores could cause the scattering. To check these hypotheses, we can compare the XTT results to the microtomographic measurements (cf. fig. 4.2e)-g)). These measurements clearly show that the scattering corresponds to the orientation of the pores in between the fibers. In the sample's uppermost layer the pores are oriented along the z' axis and produce scattering mostly in the x' direction. In the intermediate felt layers, no oriented pores are found and the scattering is isotropic. The pores in the lowermost layer are oriented along the x' axis and produce scattering mostly in the z' direction.

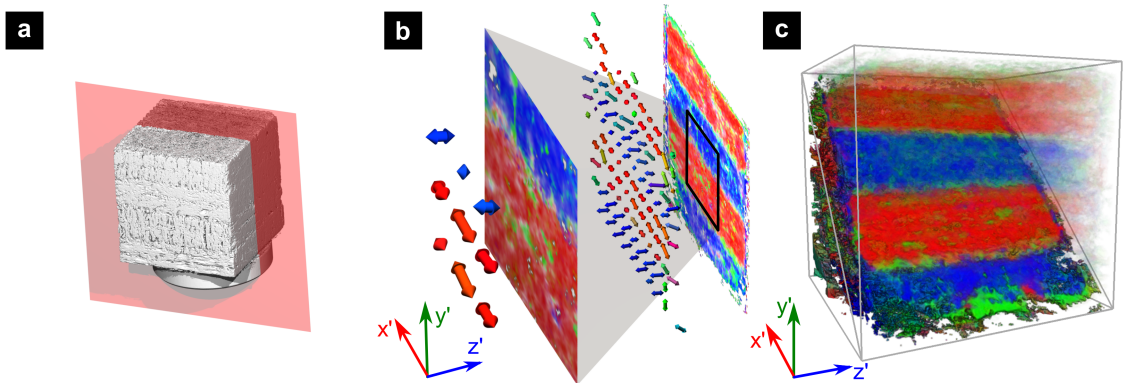

Fig. 4.6: Reconstructed local orientation and anisotropy. Based on the raw data shown in fig. 4.5, we derived the local orientation and anisotropy by fitting an ellipsoid to the scattering strength in every volume element. From the orientation and length of its major and minor axis, we computed the local scattering direction and anisotropy. a) A microCT rendering of the sample showing the location of the plane visualized in subfigure b). b) 3D rendering of the plane marked in a). Arrows show the local scattering direction and strength. A different way to visualize the local orientation and anisotropy is by color encoding. The three color channels (red/green/blue) correspond to the components of the scattering direction. The transparency channel is used to indicate the magnitude of the scattering strength. c) The whole volume rendered using the described color encoding. For better visibility of the inside, the upper right half of the cube is displayed with higher transparency. The reconstructions results gained with X-Ray Tensor Tomography qualitatively agree with the micro-tomography data (cf. fig. 4.2).

4.6 Extraction of Anisotropy and Main Scattering Direction via Ellipsoid Fitting

From the already quite large number of different scattering directions shown in fig. 4.5, it is hard to deduce the actual scattering amount and direction by eye. Therefore, we fitted an ellipsoid to the scattering data in every volume element. The fitting procedure was performed according to [70] by iterative least square ellipsoid-specific fitting. With this method, the result is guaranteed to be an ellipsoid and not only an arbitrary quadratic surface. Each ellipsoid represents a scattering tensor describing the amount of scattering with respect to the direction. Every ellipsoid's major axis then points in the direction of maximum scattering and the ratio between the length of the major and minor axis is a measure of the anisotropy at this location.

Fig. 4.6b) shows the reconstructed main scattering direction and anisotropy of a single plane through the sample as vector arrows and encoded in color. The

location of this cross-sectional plane is marked in subfigure a). In the color representation, the scattering direction is encoded in the red, green, and blue color channels with the absolute value of the vector component x' corresponding to red, y' to green, and z' to blue. The anisotropy is encoded in each voxel's transparency with transparent meaning isotropic and opaque corresponding to completely anisotropic. Fig. 4.6c) gives an impression of the scattering directions in the whole cube by applying the color encoding. For better visibility of the reconstructed data inside the object, the upper right half of the cube is rendered with higher transparency.

From the color encoding and the corresponding micro-tomography slices shown in fig. 4.2, one can see that the scattering orientation calculated with the new low-resolution dark-field tensor tomography agrees with the pore structures obtained from the high-resolution but absorption-based micro-tomography. The main orientation is quite homogeneous inside each of the oriented layers stacked on top of each other, while it appears inhomogeneous at the locations of the intermediate felt layers.

4.7 Conclusion

In summary, the results presented in this chapter show that the directional dark-field signal obtained with x-ray grating interferometry allows to tomographically reconstruct the local scattering properties of a specimen. By fitting an ellipsoid to the reconstructed scattering data, we calculated a symmetric scattering tensor describing the local direction-dependent scattering power. The scattering properties of the sample calculated with this X-Ray Tensor Tomography method agree with the orientation of the micro-structures forming the sample. The following chapter focuses on future applications, improvements, and extensions of the simulation framework, Directional Dark-Field Imaging, and – last but not least – X-Ray Tensor Tomography.

5 Outlook

We are at the very beginning of time for the human race. It is not unreasonable that we grapple with problems. But there are tens of thousands of years in the future. Our responsibility is to do what we can, learn what we can, improve the solutions, and pass them on.

Richard P. Feynman

Which future investigations could be performed on the basis of the results presented in this thesis? Concerning the dark-field simulations, the results should be extended for classes of samples with sample structure sizes below and above the lenghtscales adressed in chapter 2. An interesting question is, at which length scale and how the dark-field signal is transferred to phase contrast. Of course, the detector pixel size will play a role here, but the exact details have not been examined, yet. More realistic simulations could be performed if detector noise was included in the simulation process. Its influence on the different contrast modalities should as well be investigated. Until now, all simulations I performed were strictly monochromatic. The changes in the signal of (Directional) Dark-Field Imaging with respect to polychromatic illumination as in laboratory-based setups is another interesting topic. I already carried out simulations for a cone-beam setup geometry, but they are not part of this thesis. Please refer to [71] for further details. Finally, a more general theoretical description than the existing approximation for spherical objects has to be derived, that connects the sample properties and the dark-field signal.

With respect to Directional Dark-Field Imaging, the model developed in chapter 3 could for example be applied in materials science (e.g. compounds containing carbon fibers or meshes) and even have a large impact on medical diagnostics for example in the case of trabecular bone. For instance, diagnosis and treatment monitoring of osteoporosis, which is a major public health problem through its

association with fragility fractures, may be improved by taking interferometric projection images. Osteoporosis is characterized not only by loss of bone mineral density but also by decreasing bone quality including a deterioration of the trabecular microstructure [72]. Such changes of the trabecular bone structure due to osteoporosis or osteoporosis-related treatment may be detected a lot earlier and with higher sensitivity if compared to conventional x-ray techniques.

A large set of modifications could be realized to improve the X-Ray Tensor Tomography method presented in chapter 4. From the scattering tensor it is possible to derive the local sub-pixel structure orientation, but not the sizes of the contributing features. In the future, if energy-resolving pixelated detectors become available, it should also be possible to reconstruct the size distribution of these non-resolvable features, because then it is possible to take the energy-dependence of scattering and interferometer sensitivity into account. Nowadays, the energy dependence could already be studied at a synchrotron or a Compact Light Source. Even without high energy resolution, the sensitivity of the interferometer should be taken into account during reconstruction. Then not only effective scattering values like in chapter 4 but also the actual amount of scattering in the sample could be calculated.

X-Ray Tensor Tomography, in principle, could also have a large impact in the medical field, for example in the diagnosis of bone pathologies like osteoporosis. Up to now, only a qualitative comparison of the scattering directions and the sample morphology has been carried out. A quantitative comparison between the scattering tensor data and the actual structure orientation should be performed as well. This could be done based on the local orientation derived from high-resolution structural data, for example by computing the local Star Length Distribution (SLD) [73]. A major challenge will be the visualization of the tensor data, though. The raw data potentially will be constituted by a lot more different scattering directions, which cannot be viewed at the same time. Even the visualizations chosen in this thesis have their drawbacks. For a good overview, an arrow representation either requires a coarse grid, which neglects a lot of the data and might hide exactly the relevant features of interest. Without a three-dimensional viewing device, this visualization has ambiguities, too. Color encoding has been used in other techniques like Diffusion Tensor Imaging, which also need to display direction information. Here as well, the color encoding cannot be chosen such that there is a unique correspondence between color and direction [74]. The encoding presented in section 4.5 displays several diagonal directions in the same color. Another in-depth study should be performed with respect to time and dose reduction and influence of the number of angles on the accuracy of the reconstruction. Moreover, different experimental

techniques (e.g. Small-Angle X-Ray Scattering) might provide a physical model similar to the one derived here. Thus, the algorithm could easily be adapted to perform reconstructions in other areas.

A The Transmission of a Set of Randomly Distributed Spheres

In section 2.3.2, an analytic value for the transmission of a large number of randomly distributed spheres was used to compare it to the results from the simulations. Here, the expression given in equation (2.60) shall be derived.

For an arbitrary sample, the transmission $T(x,y)$ with respect to the position transverse to the x-ray beam is given by the Beer-Lambert law:

$$T(x,y) = \exp\left(-\int \mu(x,y,z)\,\mathrm{d}z\right). \tag{A.1}$$

$\mu(x,y,z)$ denotes the absorption coefficient of the sample. Only one material was used for the randomly distributed spheres in chapter 2. Therefore, $\mu(x,y,z)$ takes either a fixed value μ or 0, depending on whether we are inside or outside a sphere. Then, the Beer-Lambert law can be simplified to

$$T(x,y) = \exp\left(-\mu\,\Delta z(x,y)\right), \tag{A.2}$$

with $\Delta z(x,y)$ denoting the length of the path, which lies inside the spheres, for the ray arriving at (x,y). As long as the thickness of the sample does not vary too much over the area of a detector pixel, the transmission T measured in this pixel is given by

$$T \approx \exp\left(-\mu\,\langle\Delta z\rangle\right). \tag{A.3}$$

$\langle\Delta z\rangle$ is the mean path, which all rays arriving at the detector pixel travel through the sphere material.

Consequently, only an expression for $\langle\Delta z\rangle$ is required. Let N_S be the number of spheres in the whole sample volume and A_S be the total area transverse to the beam covered by the sample. Without loss of generality, as the mean thickness is assumed to be constant with respect to the position (x,y), we can assume that all spheres relevant for the calculation of the mean thickness are spread over the

circular area A centered at $x = y = 0$. Let $d(x,y)$ denote the thickness of one single sphere located at the coordinate center and d_S the sphere diameter. Then the mean thickness $\langle \Delta z \rangle$ can be calculated from

$$\langle \Delta z \rangle = \underbrace{\frac{N_S}{A_S} \iint_A 1 \, \mathrm{d}x\mathrm{d}y}_{(\star)} \underbrace{\frac{\iint_A d(x,y) \, \mathrm{d}x\mathrm{d}y}{\iint_A 1 \, \mathrm{d}x\mathrm{d}y}}_{(\star\star)}. \tag{A.4}$$

The terms denoted by $(\star)$ represent the number of spheres falling in the relevant area to contribute to the mean thickness. $(\star\star)$ is the mean thickness produced by one sphere. In the following, the integrals are calculated:

$$\begin{aligned}
\langle \Delta z \rangle &= \frac{N_S}{A_S} \frac{A}{A} \iint_A d(x,y) \, \mathrm{d}x\mathrm{d}y \\
&= \frac{N_S}{A_S} \int_{-d_S/2}^{d_S/2} \int_{-\sqrt{(d_S/2)^2 - y^2}}^{\sqrt{(d_S/2)^2 - y^2}} 2\sqrt{(d_S/2)^2 - x^2 - y^2} \, \mathrm{d}x\mathrm{d}y \\
&= \frac{2N_S}{A_S} \frac{d_S^3 \pi}{12}.
\end{aligned}$$

With this result, we arrive at

$$T \approx \exp\left(-\mu \langle \Delta z \rangle\right) = \exp\left(-\mu \frac{N_S \pi}{6 A_S} d_S^3\right) \tag{A.5}$$

as it was stated in eq. (2.60).

B Simulation Script for Directional Dark-Field Imaging

The following script was used to generate the simulation results presented in chapter 3:

Listing B.1: The python simulation script used to simulate directional dark-field imaging.

```
# -*- coding: utf-8 -*-
"""
superposition.py

Dark-field simulation script.

This script simulates two anisotropic layers to examine
the underlying superposition principle.

@author: Andreas Malecki

"""

import numpy as np
import time
from pyXSFW.material import Material
from pyXSFW.propagation import (AngularSpectrumPropagator,
                                DummyPropagator)
from pyXSFW.components import (PlanewaveSource,
                               RectangularGrating,
                               GratingStepper,
                               PilatusLikeDetector,
                               DetectorController,
                               FlatCylindersSample,
```

```
                                    GaussianSmoother)

start = time.time()

output_prefix = 'results/'
sample_prefix = 'samples/'

configurations = list()

Nangles = 16

# Do simulations for 10 different sets of randomly
# distributed positions
for statistical_run in np.arange(10):
    # Do simulations for 125 and 250 cylinders
    for number_of_cylinders in (125, 250):
        # Do simulations for sample 1 and different
        # orientations
        for i in range(Nangles):
          configurations.append({
          'output_path':
          '%d cylinders layer 1 angle %03d run %02d.h5' %
          (number_of_cylinders, i*360./Nangles,
          statistical_run),
          'sample': [{'filename':
          '%d random cylinders layer 1 run %02d.csv' %
          (number_of_cylinders, statistical_run),
          'angle': i*2.*np.pi/Nangles}]})

        # Do simulations for sample 2 and different
        # orientations
        for i in range(Nangles):
            configurations.append(
            {'output_path':
            '%d cylinders layer 2 angle %03d run %02d.h5'%
            (number_of_cylinders, i*360./Nangles,
            statistical_run),
            'sample': [{'filename':
            '%d random cylinders layer 2 run %02d.csv' %
            (number_of_cylinders, statistical_run),
            'angle': i*2.*np.pi/Nangles}]})

```

```
        # Do simulations for sample 1 and 2 and different
        # orientations
        for i in range(Nangles):
            # Only simulate relative angles of 0°, 45° and
            # 90° to save time
            for j in (i, (i+2)%Nangles, (i+4)%Nangles):
              configurations.append(
              {'output_path':
              ('%d cylinders layer 1 + 2 angle1 %03d '+
              'angle2 %03d run %02d.h5') %
              (number_of_cylinders, i*360./Nangles,
              j*360./Nangles, statistical_run),
              'sample': [{'filename':
              '%d random cylinders layer 1 run %02d.csv'%
              (number_of_cylinders, statistical_run),
              'angle': i*2.*np.pi/Nangles},
              {'filename':
              '%d random cylinders layer 2 run %02d.csv'%
              (number_of_cylinders, statistical_run),
              'angle': j*2.*np.pi/Nangles}]})

    # Do simulations for sample 1 (125 cylinders) and 2
    # (250 cylinders) and different orientations
    for i in range(Nangles):
        j = (i + 2) % Nangles
        configurations.append(
          {'output_path':
           ('%d cylinders layer 1 + %d cylinders layer 2'+
           ' angle1 %03d angle2 %03d run %02d.h5') %
           (125, 250, i*360./Nangles,
           j*360./Nangles, statistical_run),
           'sample': [{'filename':
           '%d random cylinders layer 1 run %02d.csv' %
           (125, statistical_run),
           'angle': i*2.*np.pi/Nangles},
           {'filename':
           '%d random cylinders layer 2 run %02d.csv' %
           (250, statistical_run),
           'angle': j*2.*np.pi/Nangles}]})

for configuration in configurations:
    source = PlanewaveSource(name='Source', index=0,
```

```
109                 position=(0, 0, -1.0), energy=45.7e3,
110                 N=(8192, 8192), delta=5e-6/40)
111
112     samples = list()
113     for entry in configuration['sample']:
114         samples.append(FlatCylindersSample(name='Sample',
115           index=0,
116           position=(0,0, -30e-3 + len(samples) * 10e-3),
117           filename=sample_prefix+entry['filename'],
118           scale=(500e-6, 500e-6),
119           rotate=entry['angle'],
120           height = 1000e-6, force_height=True,
121           diameter=50e-6, force_diameter=True,
122           material=Material('Ca', 1.55)))
123
124     G1 = RectangularGrating(name='G1', index=0,
125           position=(0, 0, 0), period=5e-6, dutycycle=0.5,
126           material_substrate=Material('Si', 2.336),
127           material_lines=Material('Ni', 8.908),
128           material_spaces=Material(),
129           height_substrate=500e-6, height_lines=8e-6,
130           height_spaces=0e-6)
131
132     smoother = GaussianSmoother(name='Smoother', index=0,
133                 position=(0., 0., 0.46075), sigma_x=1e-6,
134                 sigma_y=1e-6)
135
136     G2 = RectangularGrating(name='G2', index=0,
137           position=(2.5e-6, 0., 0.46075),
138           period=5e-6, dutycycle=0.5,
139           material_substrate=Material('Si', 2.336),
140           material_lines=Material('Au', 19.32),
141           material_spaces=Material(),
142           height_substrate=500e-6, height_lines=150e-6,
143           height_spaces=0e-6)
144
145     stepper = GratingStepper(name='Stepper', index=0,
146                 grating=G2, steps=8,
147                 distance=(G2.get_period(), 0))
148
149     detector = PilatusLikeDetector(name='Detector',
150                 index=0,
```

```
                    filename=output_prefix+
                             configuration['output_path'],
                    position=(0, 0, 0.46075),
                    pixelsize=(250e-6, 250e-6),
                    sensor_material=Material('Si', 2.336),
                    sensor_thickness=450e-6)

    detector_controller = DetectorController('Controller',
                                detector=detector)

    source.add_propagator(
      AngularSpectrumPropagator(to=samples[0]))
    for i in range(len(samples) - 1):
        samples[i].add_propagator(
          AngularSpectrumPropagator(to=samples[i+1]))
    samples[len(samples) - 1].add_propagator(
      AngularSpectrumPropagator(to=G1))
    G1.add_propagator(
      AngularSpectrumPropagator(to=smoother))
    smoother.add_propagator(DummyPropagator(to=stepper))
    stepper.add_propagator(
      DummyPropagator(to=detector_controller))

    source.calculate_results()

end = time.time()
print 'The complete simulation took %f s.' % (end-start)
```

Acknowledgments

If I have seen further it is by standing on ye sholders of Giants.

Isaac Newton

Just as Rome was not built in one day, it took a long time filled with experiments, discussions, hard and hardly thinking to finally arrive at the results I presented in this thesis. Consequently, there is a long list of people, who contributed to this outcome in many different ways.

Most importantly, before I could start my work, the idea that reconstructing the scattering including the direction could be possible, was put into a project by Prof. Franz Pfeiffer. He and Guillaume Potdevin provided a lot of support during the three years of my research on this topic. They also always provided an environment of creativity paired with a financial background that allowed to realize almost any idea that came to our mind.

I want to thank Prof. Nassir Navab, and especially Tobias Lasser from the Chair for Computer Aided Medical Procedures at the Technische Universität München for giving their advice on computed tomography with a computer science background.

All people who, during my time as PhD student, were at the Chair for Biomedical Physics at the Technische Universität München, also known as E17, certainly contributed to the success of my PhD project. I would like to set the following people apart: Klaus Achterhold, Martin Bech, Karin Burger, Michael Chabior, Martin Dierolf, Elena Eggl, Andreas Fehringer, Dieter Hahn, Hans Märcz, Friedrich Prade, Dieter Renker, Adrian Sarapata, Florian Schaff, Simone Schleede, Markus Schüttler, Arne Tapfer, Pierre Thibault, Astrid Velroyen, Konstantin Willer, Marian Willner, Johannes Wolf, and Andre Yaroshenko. Many of them also read through the manuscript of this thesis and helped finding

mistakes. I also want to thank my former colleague Thomas Biernath, who unfortunately passed away after a long time of severe illness. He built the experimental setup, which provided the data to most of the studies presented here.

I was part of very fruitful collaborations with the Institute for Radiology of the Klinikum rechts der Isar and the virtual institute "New X-ray analytic methods in materials science" of the Helmholtz association. Special thanks go to the medical doctors Thomas Baum and Jan S. Bauer for sharing their knowledge of bone pathologies and Peter B. Noël for his advice on topics in the field of computed tomography. Without the virtual institute I would not have received a perfect sample to demonstrate that X-Ray Tensor Tomography works. Here, my thanks go to Jens Maisenbacher, Jens Gibmeier, and Prof. Alexander Wanner.

There is quite a number of publications that arose throughout my thesis project. Thanks to everybody who served as co-author to the articles and conference abstracts and helped proofread all the manuscripts. A detailed publication list is located on page 107 onward.

The Technische Universität München Graduate School provided many essential soft-skill courses that improved my work significantly. I want to thank ALDI for the support of my studies by providing cheap food, POV-Ray for allowing me to create so many nice images, and the Flying Spaghetti Monster.

Most importantly, I want to acknowledge the support by my girlfriend and – in the meantime – wife, Christiane Malecki, who patiently endured my stays abroad for conferences and experiments. Without her driving force, this work would also not have been finished in such a short time.

Publications and Talks Resulting from this Work

Here, all written publications, conference talks, and poster presentations, which were a result of the work presented in this thesis, are listed in chronological order. They are separated into first-authored and co-authored articles as well as oral and poster presentations.

Articles

Andreas Malecki, Guillaume Potdevin, and Franz Pfeiffer. Quantitative wave-optical numerical analysis of the dark-field signal in grating-based X-ray interferometry. *Europhys. Lett.*, 99(4):48001, aug 2012. ISSN 0295-5075. doi: 10.1209/0295-5075/99/48001.

Andreas Malecki, Guillaume Potdevin, Thomas Biernath, Elena Eggl, Eduardo Grande Garcia, Thomas Baum, Peter B Noël, Jan S Bauer, and Franz Pfeiffer. Coherent Superposition in Grating-Based Directional Dark-Field Imaging. *PLoS ONE*, 8(4):e61268, 2013. doi: 10.1371/journal.pone.0061268.

Andreas Malecki, Guillaume Potdevin, Thomas Biernath, Elena Eggl, Eduardo Grande Garcia, Thomas Baum, Peter B. Noël, Jan S. Bauer, and Franz Pfeiffer. X-Ray Tensor Tomography. Submitted to Physical Review Letters.

Co-authored Articles

Guillaume Potdevin, Andreas Malecki, Thomas Biernath, Martin Bech, Torben Haugaard Jensen, Robert Feidenhans'l, Irene Zanette, Timm Weitkamp, Johannes Kenntner, Jürgen Mohr, Paul Roschger, Michael Kerschnitzki, Wolfgang Wagermaier, Klaus Klaushofer, Peter Fratzl, and Franz Pfeiffer. X-ray vector radiography for bone micro-architecture diagnostics. *Phys. Med. Biol.*, 57(11):3451–3461, jun 2012. ISSN 1361-6560. doi: 10.1088/0031-9155/57/11/3451.

Simone Schleede, Felix G Meinel, Martin Bech, Julia Herzen, Klaus Achterhold, Guillaume Potdevin, Andreas Malecki, Silvia Adam-Neumair, Sven F Thieme, Fabian Bamberg, Konstantin Nikolaou, Alexander Bohla, Ali Ö Yildirim, Roderick Loewen, Martin Gifford, Ronald Ruth, Oliver Eickelberg, Maximilian Reiser, and Franz Pfeiffer. Emphysema diagnosis using X-ray dark-field imaging at a laser-driven compact synchrotron light source. *Proceedings of the National Academy of Sciences of the United States of America*, 109(44):17880–5, October 2012. ISSN 1091-6490. doi: 10.1073/pnas.1206684109.

Astrid Velroyen, Martin Bech, Andreas Malecki, Arne Tapfer, Andre Yaroshenko, Michael Ingrisch, C C Cyran, S D Auweter, K Nikolau, M Reiser, and Franz Pfeiffer. Microbubbles as a scattering contrast agent for grating-based x-ray dark-field imaging. *Physics in Medicine and Biology*, 58(7):N37–N46, 2013. doi: 10.1088/0031-9155/58/4/N37.

Oral Presentations

Andreas Malecki, Thomas Biernath, Martin Bech, Tobias Lasser, Guillaume Potdevin, and Franz Pfeiffer. Towards the Reconstruction of 3D Orientation Information from Direction-Sensitive X-Ray Projections. In *The 11th International Meeting on Fully Three-Dimensional Image Reconstruction in Radiology and Nuclear Medicine and the 3rd Workshop on High Performance Image Reconstruction*, pages 391–394, Potsdam, Germany, July 2011.

Andreas Malecki, Guillaume Potdevin, Thomas Biernath, Martin Bech, and Franz Pfeiffer. X-ray vector radiography for bone micro-architecture diagnostics. Frühjahrstagung der Deutschen Physikalischen Gesellschaft, Berlin, Germany, March 2012.

Andreas Malecki, Thomas Biernath, Guillaume Potdevin, Martin Bech, and Franz Pfeiffer. Advances in x-ray dark field imaging and tomography. SPIE Optics + Photonics, San Diego, CA, USA, August 2012.

Poster Presentations

Andreas Malecki, Thomas Biernath, Martin Bech, Tobias Lasser, Guillaume Potdevin, and Franz Pfeiffer. Directional X-Ray Scattering Tomography. In *The 12th International Meeting on Fully Three-Dimensional Image Reconstruction in Radiology and Nuclear Medicine*, Lake Tahoe, CA, USA, June 2013.

Bibliography

[1] Frits Zernike. How I discovered phase contrast - Nobel Lecture, December 11, 1953. In *Nobel Lectures, Physics 1942-1962*, pages 239–246. Elsevier Publishing Company, Amsterdam, 1964.

[2] Frits Zernike. Das Phasenkontrastverfahren bei der mikroskopischen Beobachtung. *Zeitschrift für technische Physik*, 16:454–457, 1935.

[3] Frits Zernike. Phase Contrast, a New Method for the Microscopic Observation of Transparent Objects. *Physica*, 9(10):974–986, 1942.

[4] Richard Wheeler. Micrograph of whatman lens tissue paper. bright field illumination. 10x magnification, 1.559 µm/px. http://en.wikipedia.org/wiki/File:Paper_Micrograph_Bright.png, June 2010. Accessed 25 March 2013.

[5] Richard Wheeler. Micrograph of whatman lens tissue paper. phase contrast illumination. 10x magnification, 1.559 µm/px. http://en.wikipedia.org/wiki/File:Paper_Micrograph_Phase.png, June 2010. Accessed 25 March 2013.

[6] Richard Wheeler. Micrograph of whatman lens tissue paper. dark field illumination. 10x magnification, 1.559 µm/px. http://en.wikipedia.org/wiki/File:Paper_Micrograph_Dark.png, June 2010. Accessed 25 March 2013.

[7] Arthur Stanton. Wilhelm Conrad Röntgen - On a New Kind of Rays - Translation from the Sitzungsberichte der Würzburger Physik-medic. Gesellschaft, 1895. *Nature*, 53(1369):274–276, January 1896. ISSN 0028-0836. doi: 10.1038/053274b0.

[8] C. T. Odhner. Nobel Prize in Physics 1901 - Presentation Speech. In *Nobel*

Lectures, Physics 1901-1921. Elsevier Publishing Company, Amsterdam, 1967.

[9] U. Bonse and M. Hart. An X-Ray Interferometer. *Applied Physics Letters*, 6 (8):155, 1965. ISSN 00036951. doi: 10.1063/1.1754212.

[10] Günter Schmahl, Dietbert Rudolph, Peter Guttmann, Gerd Schneider, Jürgen Thieme, and Bastian Niemann. Phase contrast studies of biological specimens with the x-ray microscope at BESSY (invited). *Review of Scientific Instruments*, 66(2):1282, 1995. ISSN 00346748. doi: 10.1063/1.1145955.

[11] Y. Kagoshima, Y. Yokoyama, T. Niimi, T. Koyama, Y. Tsusaka, J. Matsui, and K. Takai. Hard X-ray phase-contrast microscope for observing transparent specimens. *Journal de Physique IV (Proceedings)*, 104:49–52, March 2003. ISSN 1155-4339. doi: 10.1051/jp4:200300027.

[12] Michael Chabior. *Contributions to the characterization of grating-based x-ray phase-contrast imaging*. Phd thesis, Technischen Universität Dresden, 2011.

[13] A. Snigirev, I. Snigireva, V. Kohn, S. Kuznetsov, and I. Schelokov. On the possibilities of x-ray phase contrast microimaging by coherent high-energy synchrotron radiation. *Review of Scientific Instruments*, 66(12):5486, 1995. ISSN 00346748. doi: 10.1063/1.1146073.

[14] C. Raven, A. Snigirev, I. Snigireva, P. Spanne, A. Souvorov, and V. Kohn. Phase-contrast microtomography with coherent high-energy synchrotron x rays. *Applied Physics Letters*, 69(13):1826–1828, 1996.

[15] Atsushi Momose. Phase-contrast radiographs of nonstained rat cerebellar specimen. *Medical Physics*, 22(4):375, 1995. ISSN 00942405. doi: 10.1118/1.597472.

[16] E. Förster, K. Goetz, and P. Zaumseil. Double Crystal Diffractometry for the Characterization of Targets for Laser Fusion Experiments. *Kristall und Technik*, 15(8):937–945, 1980. ISSN 00234753. doi: 10.1002/crat.19800150812.

[17] V N Ingal and E A Beliaevskaya. X-ray plane-wave topography observation of the phase contrast from a non-crystalline object. *Journal of Physics D: Applied Physics*, 28(11):2314–2317, November 1995. ISSN 0022-3727. doi: 10.1088/0022-3727/28/11/012.

[18] T. J. Davis, D. Gao, T. E. Gureyev, A. W. Stevenson, and S. W. Wilkins.

Phase-contrast imaging of weakly absorbing materials using hard X-rays. *Nature*, 373(6515):595–598, February 1995. ISSN 0028-0836. doi: 10.1038/373595a0.

[19] Franz Pfeiffer, Timm Weitkamp, Oliver Bunk, and Christian David. Phase retrieval and differential phase-contrast imaging with low-brilliance X-ray sources. *Nature Physics*, 2(4):258–261, 2006. doi: 10.1038/nphys265.

[20] Timm Weitkamp, Christian David, Christian Kottler, Oliver Bunk, and Franz Pfeiffer. Tomography with grating interferometers at low-brilliance sources. In *Proceedings of SPIE*, volume 6318, page 63180S, 2006. doi: 10.1117/12.683851.

[21] Franz Pfeiffer, Martin Bech, Oliver Bunk, P. Kraft, E. F. Eikenberry, C. Brönnimann, C. Grünzweig, and Christian David. Hard-X-ray dark-field imaging using a grating interferometer. *Nature Materials*, 7(2): 134–137, 2008. doi: 10.1038/nmat2096.

[22] J. F. Clauser and M. W. Reinsch. New Theoretical and Experimental Results in Fresnel Optics with Applications to Matter-Wave and X-Ray Interferometry. *Applied Physics B*, 54(5):380–395, May 1992. ISSN 0721-7269. doi: 10.1007/BF00325384.

[23] Christian David, B. Nöhammer, H. H. Solak, and E. Ziegler. Differential x-ray phase contrast imaging using a shearing interferometer. *Applied Physics Letters*, 81(17):3287, 2002. ISSN 00036951. doi: 10.1063/1.1516611.

[24] Atsushi Momose, Shinya Kawamoto, Ichiro Koyama, Yoshitaka Hamaishi, Kengo Takai, and Yoshio Suzuki. Demonstration of X-Ray Talbot Interferometry. *Japanese Journal of Applied Physics*, 42(Part 2, No. 7B): L866–L868, July 2003. ISSN 0021-4922. doi: 10.1143/JJAP.42.L866.

[25] Timm Weitkamp, Ana Diaz, Christian David, Franz Pfeiffer, Marco Stampanoni, Peter Cloetens, and Eric Ziegler. X-ray phase imaging with a grating interferometer. *Optics Express*, 13(16):6296, 2005.

[26] Han Wen, Eric E. Bennett, Monica M. Hegedus, and Stanislas Rapacchi. Fourier X-ray Scattering Radiography Yields Bone Structural Information. *Radiology*, 251(3):910–918, June 2009. ISSN 1527-1315. doi: 10.1148/radiol.2521081903.

[27] Wataru Yashiro, Y. Terui, K. Kawabata, and Atsushi Momose. On the

origin of visibility contrast in x-ray Talbot interferometry. *Optics Express*, 18(16):16890–16901, 2010. doi: 10.1364/OE.18.016890.

[28] Guillaume Potdevin, Andreas Malecki, Thomas Biernath, Martin Bech, Torben Haugaard Jensen, Robert Feidenhans'l, Irene Zanette, Timm Weitkamp, Johannes Kenntner, Jürgen Mohr, Paul Roschger, Michael Kerschnitzki, Wolfgang Wagermaier, Klaus Klaushofer, Peter Fratzl, and Franz Pfeiffer. X-ray vector radiography for bone micro-architecture diagnostics. *Phys. Med. Biol.*, 57(11):3451–3461, jun 2012. ISSN 1361-6560. doi: 10.1088/0031-9155/57/11/3451.

[29] Martin Bech, O Bunk, Tilman Donath, R Feidenhans'l, C David, and Franz Pfeiffer. Quantitative x-ray dark-field computed tomography. *Physics in Medicine and Biology*, 55(18):5529–5539, September 2010. ISSN 1361-6560. doi: 10.1088/0031-9155/55/18/017.

[30] Guang-Hong Chen, Nicholas Bevins, Joseph Zambelli, and Zhihua Qi. Small-angle scattering computed tomography (SAS-CT) using a Talbot-Lau interferometerand a rotating anode x-ray tube: theory and experiments. *Optics Express*, 18(12):12960–12970, June 2010. ISSN 1094-4087.

[31] Wataru Yashiro, Sébastien Harasse, Katsuyuki Kawabata, Hiroaki Kuwabara, Takashi Yamazaki, and Atsushi Momose. Distribution of unresolvable anisotropic microstructures revealed in visibility-contrast images using x-ray Talbot interferometry. *Physical Review B*, 84(9):094106, September 2011. ISSN 1098-0121. doi: 10.1103/PhysRevB.84.094106.

[32] Susanna K. Lynch, Vinay Pai, Julie Auxier, Ashley F. Stein, Eric E. Bennett, Camille K. Kemble, Xianghui Xiao, Wah-Keat Lee, Nicole Y. Morgan, and Han Harold Wen. Interpretation of dark-field contrast and particle-size selectivity in grating interferometers. *Applied Optics*, 50(22):4310–4319, July 2011. ISSN 0003-6935. doi: 10.1364/AO.50.004310.

[33] P. Modregger, F. Scattarella, B. Pinzer, C. David, R. Bellotti, and M. Stampanoni. Imaging the Ultrasmall-Angle X-Ray Scattering Distribution with Grating Interferometry. *Physical Review Letters*, 108(4): 048101, January 2012. ISSN 0031-9007. doi: 10.1103/PhysRevLett.108.048101.

[34] Andreas Malecki, Guillaume Potdevin, and Franz Pfeiffer. Quantitative wave-optical numerical analysis of the dark-field signal in grating-based

X-ray interferometry. *Europhys. Lett.*, 99(4):48001, aug 2012. ISSN 0295-5075. doi: 10.1209/0295-5075/99/48001.

[35] Joseph John Thomson. *Conduction of electricity through gases*. Cambridge University Press, Cambridge, 2 edition, 1906.

[36] Charles G. Barkla. Polarisation in Röntgen Rays. *Nature*, 69(1794):463, March 1904. ISSN 0028-0836. doi: 10.1038/069463a0.

[37] Charles G. Barkla. Polarised Röntgen Radiation. *Philosophical Transactions of the Royal Society A*, 204:467–479, January 1905. ISSN 1364-503X. doi: 10.1098/rsta.1905.0013.

[38] Michael Eckert. Disputed discovery: The beginnings of X-ray diffraction in crystals in 1912 and its repercussions. *Zeitschrift für Kristallographie*, 227(1): 27–35, January 2012. ISSN 0044-2968. doi: 10.1524/zkri.2012.1445.

[39] Steven Weinberg. *The Quantum Theory of Fields, Volume I: Foundations*. Cambridge University Press, Cambridge, 1995. ISBN 0521670535.

[40] Jens Als-Nielsen and Des McMorrow. *Elements of Modern X-ray Physics*. John Wiley & Sons, Chichester, 2 edition, 2011. ISBN 9780470973950.

[41] B. E. Warren. *X-Ray Diffraction*. Dover Publications, New York, 1991. ISBN 0486663175.

[42] William Henry Fox Talbot. Facts relating to Optical Science, No. IV. *The London and Edinbourgh Philosophical Magazine and Journal of Science*, 9(56): 401–407, 1836.

[43] Thomas J. Suleski. Generation of Lohmann images from binary-phase Talbot array illuminators. *Applied Optics*, 36(20):4686–4691, July 1997. ISSN 0003-6935. doi: 10.1364/AO.36.004686.

[44] Martin Bech. *X-ray imaging with a grating interferometer*. PhD thesis, University of Copenhagen, 2009.

[45] Andreas Eder and Martin Jordan. The Schlieren Technique. In Franz Mayinger and Oliver Feldmann, editors, *Optical Measurements*, Heat and Mass Transfer, pages 5–16. Springer Berlin Heidelberg, 2001. ISBN 978-3-642-63079-8. doi: 10.1007/978-3-642-56443-7_2.

[46] Allan M. Cormack. Representation of a Function by Its Line Integrals, with Some Radiological Applications. *Journal of Applied Physics*, 34(9):2722, 1963. ISSN 00218979. doi: 10.1063/1.1729798.

[47] Allan M. Cormack. Representation of a Function by Its Line Integrals, with Some Radiological Applications. II. *Journal of Applied Physics*, 35(10):2908, 1964. ISSN 00218979. doi: 10.1063/1.1713127.

[48] Godfrey N. Hounsfield. Computerized transverse axial scanning (tomography): Part 1. Description of system. *British Journal of Radiology*, 46 (552):1016–1022, December 1973. ISSN 0007-1285. doi: 10.1259/0007-1285-46-552-1016.

[49] Godfrey N. Hounsfield. Computed medical imaging - Nobel Lecture, 8 December, 1979. In Jan Lindsten, editor, *Nobel Lectures, Physiology or Medicine 1971-1980*, pages 568–586. World Scientific Publishing Co., Singapore, 1992.

[50] Thorsten M Buzug. *Computed Tomography - From Photon Statistics to Modern Cone-Beam CT*. Springer Berlin Heidelberg, Berlin, Heidelberg, 1 edition, 2008. ISBN 978-3-540-39407-5. doi: 10.1007/978-3-540-39408-2.

[51] Avinash C. Kak and Malcolm Slaney. *Principles of Computerized Tomographic Imaging*. siam, Philadelphia, 2001. ISBN 978-0-898714-94-4.

[52] Klaus Müller. *Fast and Accurate Three-Dimensional Reconstruction from Cone-Beam Projection Data Using Algebraic Methods*. PhD thesis, Ohio State University, 1998.

[53] Matteo Frigo and Steven G. Johnson. The Design and Implementation of FFTW3. *Proceedings or the IEEE*, 93(2):216–231, 2005.

[54] A. H. Andersen and A. C. Kak. Simultaneous Algebraic Reconstruction Technique (SART): A Superior Implementation of the ART Algorithm. *Ultrasonic Imaging*, 6(1):81–94, 1984.

[55] Charles Byrne. Iterative oblique projection onto convex sets and the split feasibility problem. *Inverse Problems*, 18(2):441–453, April 2002. ISSN 0266-5611. doi: 10.1088/0266-5611/18/2/310.

[56] Torben Haugaard Jensen, Martin Bech, Oliver Bunk, Tilman Donath, Christian David, Robert Feidenhans'l, and Franz Pfeiffer. Directional x-ray

dark-field imaging. *Physics in Medicine and Biology*, 55(12):3317–3323, May 2010. ISSN 1361-6560. doi: 10.1088/0031-9155/55/12/004.

[57] Torben Haugaard Jensen, Martin Bech, Irene Zanette, Timm Weitkamp, Christian David, Hans Deyhle, Simon Rutishauser, Elena Reznikova, Jürgen Mohr, Robert Feidenhans'l, and Franz Pfeiffer. Directional x-ray dark-field imaging of strongly ordered systems. *Physical Review B*, 82(21): 214103, December 2010. ISSN 1098-0121. doi: 10.1103/PhysRevB.82.214103.

[58] Michael Chabior, Tilman Donath, Christian David, Manfred Schuster, Christian Schroer, and Franz Pfeiffer. Signal-to-noise ratio in x ray dark-field imaging using a grating interferometer. *Journal of Applied Physics*, 110(5):053105, 2011. ISSN 00218979. doi: 10.1063/1.3630051.

[59] Jason D. Schmidt. *Numerical Simulation of Optical Wave Propagation With Examples in MATLAB*. SPIE Press, Bellingham, Washington USA, 1 edition, 2010. ISBN 0819483265.

[60] Joseph W. Goodman. *Introduction to Fourier Optics*. Roberts & Company Publishers, Englewood, Colorado USA, 3 edition, 2004. ISBN 0974707724.

[61] The HDF Group. Hierarchical data format version 5. http://www.hdfgroup.org/HDF5, 2000-2010.

[62] J. H. Siewerdsen, A. M. Waese, D. J. Moseley, S. Richard, and D. A. Jaffray. Spektr: A computational tool for x-ray spectral analysis and imaging system optimization. *Medical Physics*, 31(11):3057–3067, 2004. ISSN 00942405. doi: 10.1118/1.1758350.

[63] P. Bandyopadhyay and C.U. Segre. Mucal 1.3. http://www.csrri.iit.edu/mucal.html, April 2009.

[64] Torben Haugaard Jensen. *Refraction and scattering based x-ray imaging*. PhD thesis, University of Copenhagen, 2010.

[65] V. Revol, C. Kottler, R. Kaufmann, A. Neels, and A. Dommann. Orientation-selective x-ray dark field imaging of ordered systems. *J. Appl. Phys.*, 112(11):114903, 2012. ISSN 00218979. doi: 10.1063/1.4768525.

[66] Andreas Malecki, Guillaume Potdevin, Thomas Biernath, Elena Eggl, Eduardo Grande Garcia, Thomas Baum, Peter B Noël, Jan S Bauer, and

Franz Pfeiffer. Coherent Superposition in Grating-Based Directional Dark-Field Imaging. *PLoS ONE*, 8(4):e61268, 2013. doi: 10.1371/journal.pone.0061268.

[67] Andreas Malecki, Guillaume Potdevin, Thomas Biernath, Elena Eggl, Eduardo Grande Garcia, Thomas Baum, Peter B. Noël, Jan S. Bauer, and Franz Pfeiffer. X-Ray Tensor Tomography. Submitted to Physical Review Letters.

[68] W. G. Zhang, Z. J. Hu, and K. J. Hüttinger. Chemical vapor infiltration of carbon fiber felt: optimization of densification and carbon microstructure. *Carbon*, 40:2529–2545, 2002.

[69] Jörg-Martin Gebert. *Intrinsische Risse und Poren in Kohlenstoff Verbundwerkstoffen*. PhD thesis, Karlsruher Institut für Technologie (KIT), 2010.

[70] Li Qingde and John G. Griffiths. Least Squares Ellipsoid Specific Fitting. In *Proceedings of the Geometric Modeling and Processing 2004*, volume 2004, pages 335–340. IEEE, 2004. ISBN 0-7695-2078-2. doi: 10.1109/GMAP.2004.1290055.

[71] Astrid Velroyen, Martin Bech, Andreas Malecki, Arne Tapfer, Andre Yaroshenko, Michael Ingrisch, C C Cyran, S D Auweter, K Nikolau, M Reiser, and Franz Pfeiffer. Microbubbles as a scattering contrast agent for grating-based x-ray dark-field imaging. *Physics in Medicine and Biology*, 58(7):N37–N46, 2013. doi: 10.1088/0031-9155/58/4/N37.

[72] NIH Consensus Development Panel on Osteoporosis Prevention, Diagnosis, and Therapy. Osteoporosis prevention, diagnosis, and therapy. *JAMA*, 285(6):785–795, 2001. doi: 10.1001/jama.285.6.785.

[73] Anders Odgaard, Jesper Kabel, Bert van Rietbergen, Michel Dalstra, and Rik Huiskes. Fabric and Elastic Principal Directions of Cancellous Bone Are Closely Related. *Journal of Biomechanics*, 30(5):487–495, 1997.

[74] Sinisa Pajevic and Carlo Pierpaoli. Color schemes to represent the orientation of anisotropic tissues from diffusion tensor data: application to white matter fiber tract mapping in the human brain. *Magnetic resonance in medicine : official journal of the Society of Magnetic Resonance in Medicine / Society of Magnetic Resonance in Medicine*, 43(6):921, June 2000. ISSN 1522-2594.

[75] Simone Schleede, Felix G Meinel, Martin Bech, Julia Herzen, Klaus Achterhold, Guillaume Potdevin, Andreas Malecki, Silvia Adam-Neumair, Sven F Thieme, Fabian Bamberg, Konstantin Nikolaou, Alexander Bohla, Ali Ö Yildirim, Roderick Loewen, Martin Gifford, Ronald Ruth, Oliver Eickelberg, Maximilian Reiser, and Franz Pfeiffer. Emphysema diagnosis using X-ray dark-field imaging at a laser-driven compact synchrotron light source. *Proceedings of the National Academy of Sciences of the United States of America*, 109(44):17880–5, October 2012. ISSN 1091-6490. doi: 10.1073/pnas.1206684109.

[76] Andreas Malecki, Thomas Biernath, Martin Bech, Tobias Lasser, Guillaume Potdevin, and Franz Pfeiffer. Towards the Reconstruction of 3D Orientation Information from Direction-Sensitive X-Ray Projections. In *The 11th International Meeting on Fully Three-Dimensional Image Reconstruction in Radiology and Nuclear Medicine and the 3rd Workshop on High Performance Image Reconstruction*, pages 391–394, Potsdam, Germany, July 2011.

[77] Andreas Malecki, Guillaume Potdevin, Thomas Biernath, Martin Bech, and Franz Pfeiffer. X-ray vector radiography for bone micro-architecture diagnostics. Frühjahrstagung der Deutschen Physikalischen Gesellschaft, Berlin, Germany, March 2012.

[78] Andreas Malecki, Thomas Biernath, Guillaume Potdevin, Martin Bech, and Franz Pfeiffer. Advances in x-ray dark field imaging and tomography. SPIE Optics + Photonics, San Diego, CA, USA, August 2012.

[79] Andreas Malecki, Thomas Biernath, Martin Bech, Tobias Lasser, Guillaume Potdevin, and Franz Pfeiffer. Directional X-Ray Scattering Tomography. In *The 12th International Meeting on Fully Three-Dimensional Image Reconstruction in Radiology and Nuclear Medicine*, Lake Tahoe, CA, USA, June 2013.

List of Figures

List of Listings

Index